

LUDWIG-MAXIMILIANS-UNIVERSITÄT MÜNCHEN

---

# Multipartite entanglement detection and efficiency of state characterisation

---

MASTER THESIS

Nico Klein

*A thesis submitted in fulfillment of the requirements  
for the Master of Science*

Working Group of Prof. Dr. Weinfurter  
Chair Prof. Dr. Hänsch  
April 2015



LUDWIG-MAXIMILIANS-UNIVERSITÄT MÜNCHEN

---

# Detektion von Mehrteilchen-Verschränkung und Effizienz der Zustandscharakterisierung

---

MASTER THESIS

Nico Klein

*A thesis submitted in fulfillment of the requirements  
for the Master of Science*

Working Group of Prof. Dr. Weinfurter  
Chair Prof. Dr. Hänsch  
April 2015



# Declaration of Authorship

Hiermit erkläre ich, Nico Klein, diese Arbeit selbstständig und nur unter Verwendung der angegebenen Quellen und Hilfsmittel angefertigt zu haben.

I, Nico Klein, hereby declare that this thesis is my own work, and that I have not used any sources and aids other than those stated in the thesis.

Munich,

---

Signature

---



LUDWIG-MAXIMILIANS-UNIVERSITÄT MÜNCHEN

# Abstract

Faculty of physics  
Working group of Prof. Dr. Weinfurter

Master of Science

**Multipartite entanglement detection and efficiency of state characterisation**  
by Nico Klein

Certifying entanglement in a multi-qubit state can be a very demanding task. Up to now, all methods either required a lot of experimental and computational effort or were suitable only for a few specific types of states and could not be constructed for other states. In this thesis, a novel, constructive method to design non-linear genuine multipartite entanglement witnesses is introduced. The witnesses can be tailored to detect entanglement in a certain kind of states and it is often sufficient to use data obtained in only two measurement settings. The applicability of this method is proven by the experimental verification of genuine fourpartite entanglement of GHZ and cluster states, superpositions of those, and for the four-qubit Dicke and singlet state. Furthermore, this thesis illuminates the topic of quantum state tomography. Monte-Carlo simulations are used to numerically investigate the scaling of reconstruction fidelity with respect to the number of measurements. A postselection method based on the linear estimate is introduced and used to develop an intuitive understanding of the processes, effects and outcomes of popular methods to reconstruct a quantum state.

## *Acknowledgements*

First of all, I would like to express my gratitude towards Prof. Dr. Harald Weinfurter for the kind acceptance to the group, inspiring discussions throughout the year and especially for the supporting supervision of my thesis. My deepest thanks go to Lukas Knips and Christian Schwemmer for the welcoming working atmosphere and all the help. It was a pleasure to work with you! Furthermore, I would like to thank the whole XQP group and all the people in Garching, who turned every workday into a pleasant and rewarding experience. Last but not least, I am grateful for the continued support and sympathy of my parents, my dear Vanessa, and my friends, which amounted to a lot.

# Contents

<b>Declaration of Authorship</b>	<b>i</b>
<b>Abstract</b>	<b>iii</b>
<b>Acknowledgments</b>	<b>iv</b>
<b>List of Figures</b>	<b>vii</b>
<b>List of Tables</b>	<b>ix</b>
<b>1. Introduction</b>	<b>1</b>
<b>2. Fundamentals</b>	<b>3</b>
2.1. Qubits . . . . .	3
2.2. Mixed states . . . . .	5
2.2.1. Purity . . . . .	5
2.3. Multiple qubits . . . . .	6
2.4. Entanglement . . . . .	6
2.4.1. Types of entanglement . . . . .	7
2.4.2. Entanglement measures . . . . .	8
2.4.3. Entanglement witnesses . . . . .	9
2.5. Relevant states and their properties . . . . .	10
2.5.1. Bell states . . . . .	10
2.5.2. Greenberger-Horne-Zeilinger states . . . . .	11
2.5.3. Graph states . . . . .	11
2.5.4. Cluster states . . . . .	11
2.5.5. Dicke states . . . . .	12
2.6. Photon processing . . . . .	12
2.6.1. Spontaneous parametric down conversion . . . . .	12
2.6.2. Yttrium-Vanadate crystals . . . . .	14
2.6.3. Waveplates . . . . .	14
2.6.4. Beam splitters . . . . .	15
2.7. Tomographic state reconstruction . . . . .	15
2.7.1. Measurements . . . . .	15
2.7.2. Linear inversion . . . . .	17
2.7.3. Maximum likelihood estimation . . . . .	18
2.7.4. Distances and metrics on Hilbert spaces . . . . .	18
<b>3. Multipartite entanglement detection with minimal effort</b>	<b>21</b>
3.1. Theoretical background . . . . .	21
3.1.1. Correlation complementarity . . . . .	21
3.1.2. Cut-anticommutativity . . . . .	22

3.1.3.	Fourpartite non-linear entanglement witnesses for the GHZ state . . .	23
3.1.4.	Constructing a single witness for all bipartitions . . . . .	25
3.1.5.	Witnesses for other prominent states . . . . .	26
3.1.6.	Extension to more qubits . . . . .	30
3.2.	Experimental implementation . . . . .	30
3.2.1.	State preparation . . . . .	31
3.2.2.	State analysis . . . . .	32
3.2.3.	Experimental results . . . . .	35
3.3.	Conclusion . . . . .	39
<b>4.</b>	<b>Numerical investigation of Heisenberg scaling in quantum state tomography</b>	<b>41</b>
4.1.	Simulation algorithm . . . . .	41
4.1.1.	Target states . . . . .	41
4.1.2.	Simulated tomography . . . . .	43
4.2.	Results for one qubit . . . . .	43
4.2.1.	Diverging distributions and a postselection criterion . . . . .	44
4.2.2.	Pure states . . . . .	47
4.2.3.	Mixed states . . . . .	50
4.3.	Extension to more qubits . . . . .	53
4.3.1.	Product states . . . . .	53
4.3.2.	Maximally entangled states . . . . .	57
4.4.	Conclusion . . . . .	61
<b>5.</b>	<b>Conclusion</b>	<b>63</b>
<b>A.</b>	<b>Interferometer setup</b>	<b>65</b>
A.1.	Compensation of phases . . . . .	66
A.2.	Efficiencies . . . . .	67

# List of Figures

2.1. Illustration of the Bloch sphere . . . . .	4
2.2. Types of entanglement in pure states . . . . .	8
2.3. Schematic of an entanglement witness . . . . .	10
2.4. Different graph states . . . . .	12
2.5. SPDC Type I . . . . .	13
2.6. Schematic of a beam splitter . . . . .	15
2.7. Setup of polarisation analysis (PA) . . . . .	16
3.1. (Cut-)Anticommutativity graph for the GHZ witness . . . . .	25
3.2. Flowchart for witness construction . . . . .	27
3.3. Illustration of optimisation of weights . . . . .	28
3.4. Optical setup for state preparation . . . . .	31
3.5. One of the interferometers . . . . .	33
3.6. Complete experimental setup . . . . .	34
3.7. Experimental density matrices . . . . .	36
3.8. Performance of combined entanglement witnesses . . . . .	39
4.1. Target states on a projection of the Bloch sphere . . . . .	42
4.2. Scaling behaviour of infidelity . . . . .	44
4.3. Histogram of infidelities . . . . .	45
4.4. Section of the Bloch sphere with reconstructed states . . . . .	46
4.5. Scaling of infidelity with postselection . . . . .	46
4.6. Slightly rotated target state . . . . .	47
4.7. Possible outcomes for state tomography with 10 counts per basis . . . . .	48
4.8. Bloch representation of reconstructed states with slightly rotated target state . . . . .	48
4.9. Position of bend in scaling of initially physical states . . . . .	49
4.10. Flattening of scaling of initially unphysical states . . . . .	50
4.11. Scaling for mixed states with MLE . . . . .	51
4.12. Scaling for mixed states with LIN . . . . .	52
4.13. Illustration of Uhlmann infidelity . . . . .	52
4.14. Histogram of infidelities for a two-qubit product state . . . . .	54
4.15. Scaling for pure product states with MLE . . . . .	54
4.16. Discreteness in product states . . . . .	55
4.17. Mixed product states reconstructed using MLE . . . . .	56
4.18. Mixed product states reconstructed using LIN . . . . .	57
4.19. Histogram of infidelities for a two-qubit maximally entangled state . . . . .	58
4.20. Scaling for pure maximally entangled states with MLE . . . . .	58
4.21. Discreteness in maximally entangled states . . . . .	59
4.22. Additional effect in entangled states . . . . .	60
4.23. Mixed entangled states, reconstructed using MLE . . . . .	60
4.24. Mixed entangled states, reconstructed using LIN . . . . .	61

A.1. Sagnac interferometer setup . . . . .	65
A.2. Details on the interferometer setup process . . . . .	66
A.3. Measurement of zero position of glass plate . . . . .	67

# List of Tables

2.1. Settings of the wave plates for polarisation analysis . . . . .	16
3.1. All non-vanishing correlations of the four qubit GHZ state . . . . .	23
3.2. The non-vanishing correlations of the cluster state . . . . .	28
3.3. Angle settings for different bases . . . . .	36
3.4. Characterisation of 13 members states of the family . . . . .	38
4.1. Overview of all observed scaling effects . . . . .	62
A.1. How to identify the zero position of the glass plate . . . . .	68



# 1. Introduction

Since its birth with Planck’s derivation of the radiation law in the early 20<sup>th</sup> century [1], quantum mechanics has fascinated scientists all over the world. Counter intuitive phenomena observed in quantum mechanical systems stand in stark contrast with our everyday experience. Especially the *uncertainty principle* [2], which states that some properties of a quantum system are complementary such that exactly measuring one of them “destroys” the information about the other, and *entanglement* [3], where actions on one part of an entangled quantum system seem to influence the other, even though they are far apart (a phenomenon described by Einstein as “spooky action at a distance” [4]), triggered and still trigger animated discussions.

These inherently quantum mechanical features have since been used to overcome classical barriers. Quantum cryptography [5–7], quantum teleportation [8], quantum metrology [9], and quantum computation and simulation [10–12] are all examples where certain tasks cannot be performed by classical counterparts, or not with as high efficiencies. Most of these advances rely on two-level systems, also called *qubits* in correspondence to the classical *bit*, and entanglement between multiple qubits. As system sizes increase, the classification and detection of multipartite entanglement becomes harder. Even with entanglement between all parties, there are still different classes of entanglement, e.g. the GHZ and W-types [13] for tripartite entanglement.

Various physical systems, such as photons, atoms, ions or defects in solid state systems have been used to implement qubits, all with different advantages and restrictions. The experimentally realised number of coupled qubits increases rapidly, but completely analysing these systems via quantum state tomography requires an exponentially large number of measurements on a whole ensemble of the same state. It is therefore crucial to develop and understand efficient schemes to extract information about the system, e.g. whether and how much entanglement is present in it.

This thesis focuses, after introducing fundamental concepts and methods of quantum mechanics (Chapter 2), on a new method to efficiently detect genuine multipartite entanglement (Chapter 3). In Chapter 4, an intuitive understanding of current methods in quantum state tomography will be developed.

In the next chapter, “Fundamentals”, important concepts and notations concerning qubits and entanglement are introduced. Different established entanglement measures will be presented. Furthermore, some prominent quantum states used later on are introduced. After that, the basics of photon processing like the generation of polarisation entangled photons and important optical components will be described, as well as methods to analyse these photons for state tomography.

Equipped with the necessary tools, Chapter 3, “Multipartite entanglement detection with minimal effort”, derives a constructive method to design non-linear entanglement witnesses.

Based on *correlation complementarity*, our criteria allow to detect genuine multipartite entanglement in arbitrarily large systems with data of measurements in only two settings for prominent quantum states. To test the method experimentally, four-qubit GHZ and cluster states are prepared and analysed in an optical setup. Data of Dicke and singlet states obtained in previous experiments also emphasise the usability of the derived criteria.

The topic of full quantum state tomography is discussed in Chapter 4 “Numerical investigation of Heisenberg scaling in quantum state tomography”. Tomographies on simulated data are used to analyse the results for a single qubit. *Postselection criteria* which are based on properties of the linearly estimated quantum state, are used to investigate different effects (that can lead to Heisenberg scaling) of pure and mixed states, which had not been examined so far. Moreover, the developed tools are extended to two qubit product and entangled states.

## 2. Fundamentals

In this chapter, some fundamental notions and properties of quantum mechanical systems are being defined and illustrated. Amongst others, the terms *qubit*, *mixed state* and *entanglement* are introduced and shortly depicted. The basics of state reconstruction as well as often used optical components are also described. For varied formulations from a slightly different point of view, see Ref. [14–16].

### 2.1. Qubits

Analogously to a classical bit, which can have values 0 or 1, the *quantum bit* [17], in short *qubit*, can be in the states  $|0\rangle$  or  $|1\rangle$ . These states can for example be the ground state and an excited state of an atom, the spin-orientation of an electron or the polarisation of a photon. Unlike the classical bit, a qubit can also be in a superposition of  $|0\rangle$  and  $|1\rangle$ ,

$$|\psi\rangle = \alpha |0\rangle + \beta |1\rangle \quad (2.1)$$

where  $\alpha$  and  $\beta$  are complex numbers.

Since quantum states have to be normalised ( $\alpha^2 + \beta^2 = 1$ ) and a global phase cannot be observed, a pure qubit can be expressed as

$$|\psi\rangle = \cos \frac{\theta}{2} |0\rangle + e^{i\varphi} \sin \frac{\theta}{2} |1\rangle \quad (2.2)$$

so that  $|\psi\rangle$  only depends on the real variables  $\theta \in [0, \pi]$  and  $\varphi \in [0, 2\pi]$ . These variables can be interpreted as angles such that they describe a point on the surface of a three-dimensional sphere, the so called *Bloch sphere* (Figure 2.1). Every physically different two-dimensional quantum state is uniquely related to a point on the Bloch sphere. This point is described by the *Bloch vector*

$$\mathbf{r} = r \begin{pmatrix} \sin \theta \cos \varphi \\ \sin \theta \sin \varphi \\ \cos \theta \end{pmatrix}. \quad (2.3)$$

All of these states are elements of the *Hilbert space*  $\mathcal{H}$ , with the basis  $\{|0\rangle, |1\rangle\}$  often used as the *computational basis*. Of course, all sets of two orthonormal states can be used as a basis, whereas the three most important ones are given by the eigenvectors of the three *Pauli matrices*

$$\sigma_x = \begin{pmatrix} 0 & 1 \\ 1 & 0 \end{pmatrix}, \quad \sigma_y = \begin{pmatrix} 0 & -i \\ i & 0 \end{pmatrix} \quad \text{and} \quad \sigma_z = \begin{pmatrix} 1 & 0 \\ 0 & -1 \end{pmatrix}. \quad (2.4)$$

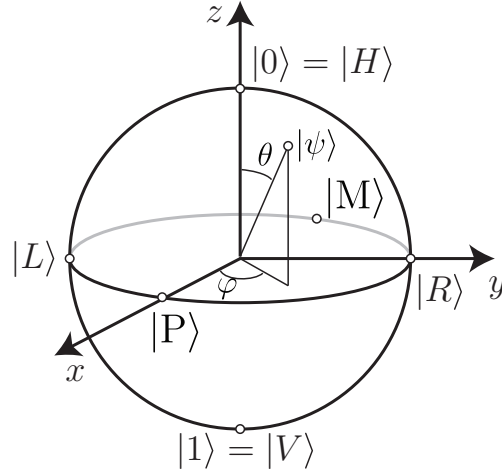


**Figure 2.1.: Illustration of the Bloch sphere.** Each point on the surface corresponds to a pure one qubit state  $|\psi\rangle$ , according to Eq. (2.2). Conventionally, the states  $|0\rangle$  and  $|1\rangle$  are arranged at  $z = 1$  and  $z = -1$  respectively. Analogously, one finds the states  $|P\rangle$  and  $|M\rangle$  at  $x = 1$  and  $x = -1$ . The points within the sphere correspond to physical states, too. These states are called *mixed states*.

The states  $|0\rangle$  and  $|1\rangle$  are then the eigenvectors of  $\sigma_z$ ,

$$\sigma_z |0\rangle = \begin{pmatrix} 1 & 0 \\ 0 & -1 \end{pmatrix} \begin{pmatrix} 1 \\ 0 \end{pmatrix} = \begin{pmatrix} 1 \\ 0 \end{pmatrix} = +|0\rangle \quad (2.5)$$

$$\sigma_z |1\rangle = \begin{pmatrix} 1 & 0 \\ 0 & -1 \end{pmatrix} \begin{pmatrix} 0 \\ 1 \end{pmatrix} = -\begin{pmatrix} 0 \\ 1 \end{pmatrix} = -|1\rangle . \quad (2.6)$$

The eigenvectors

$$|P\rangle = \frac{1}{\sqrt{2}} (|0\rangle + |1\rangle) \quad (2.7)$$

$$|M\rangle = \frac{1}{\sqrt{2}} (|0\rangle - |1\rangle) \quad (2.8)$$

of  $\sigma_x$  and

$$|R\rangle = \frac{1}{\sqrt{2}} (|0\rangle + i|1\rangle) \quad (2.9)$$

$$|L\rangle = \frac{1}{\sqrt{2}} (|0\rangle - i|1\rangle) \quad (2.10)$$

of  $\sigma_y$  ensue accordingly.

When the polarisation of a photon is described with this formalism, it is consensus to use  $|0\rangle = |H\rangle$  and  $|1\rangle = |V\rangle$  for the horizontal and vertical polarisation.  $|P\rangle$  and  $|M\rangle$  then refer to a linear diagonal polarisation and  $|R\rangle$ ,  $|L\rangle$  to right and left circular polarisation, respectively. Since the focus of this thesis lies predominantly on photons, this nomenclature will be used throughout.

## 2.2. Mixed states

The states  $|\psi\rangle$  considered up to now are called *pure states*, because it describes the behaviour of, e.g., a particle exactly (within quantum mechanical probabilities). In an actual experiment, there will be an ensemble of particles all prepared the same way, but, due to imperfections of the source, they are not necessarily all in the same pure state. In that case, a *mixed state* is needed to describe an arbitrary single particle out of the ensemble. If it could be in different pure states  $|\psi_\nu\rangle$  with some classical probabilities  $p_\nu$ , it is described by the so called *density matrix*

$$\rho = \sum_{\nu} p_{\nu} |\psi_{\nu}\rangle \langle \psi_{\nu}| \quad (2.11)$$

which has to fulfill

$$\text{Tr}(\rho) = 1 \quad (\text{normalisation}) \quad (2.12)$$

$$\langle \psi | \rho | \psi \rangle \geq 0 \quad \forall |\psi\rangle \in \mathcal{H} \quad (\text{positivity}) \quad (2.13)$$

to represent a physically meaningful state. From the above conditions, it follows that  $\rho$  must be Hermitian

$$\rho = \rho^\dagger. \quad (2.14)$$

The density matrix of a  $d$ -dimensional Hilbert space can be expressed as a  $d \times d$  matrix in a basis of the Hilbert space. For qubits, and because of the Hermiticity of the density matrix, it can be expressed by the Pauli matrices

$$\rho = \frac{1}{2} (\mathbb{1}_2 + T_x \sigma_x + T_y \sigma_y + T_z \sigma_z) = \frac{1}{2} \sum_{s=0}^3 T_s \sigma_s \quad (2.15)$$

where the coefficients  $T_s$  denote the respective expectation values  $T_s = \langle \sigma_s \rangle$ ,  $\sigma_0$  denotes the identity  $\mathbb{1}^{(2)}$ , and  $\{1, 2, 3\}$  and  $\{x, y, z\}$  are used synonymously. In this expansion, the positivity condition Eq. (2.13) imposes a bound

$$T_x^2 + T_y^2 + T_z^2 \leq 1 \quad (2.16)$$

on the squared expectation values of the Pauli matrices. Note that  $T_x, T_y, T_z$  correspond to the 3 elements of the Bloch vector Eq. (2.3), with its absolute value  $|\mathbf{r}|$  equal to 1 for pure states and smaller than 1 for mixed states. Therefore, in the Bloch picture, mixed states lie within the Bloch sphere.

### 2.2.1. Purity

When dealing with mixed states, the *purity*  $P$  is a measure for the mixedness of a state. Defined as

$$P(\rho) = \text{Tr}(\rho^2) = \sum_{\nu} p_{\nu}^2, \quad (2.17)$$

the purity can have values between 1 (for pure states) and  $1/d$  (for the  $d$ -dimensional maximally mixed state  $\rho = \mathbb{1}^{(d)}/d$ ).

### 2.3. Multiple qubits

If we now consider a system with more than a single qubit, the state of this system has to be described in a higher dimensional Hilbert space. Assuming that the qubits are distinguishable in some degree of freedom (e.g. spatial), the Hilbert space  $\mathcal{H}_{\text{comp}}$  of the composite system is described by

$$\mathcal{H}_{\text{comp}} = \mathcal{H}_1 \otimes \mathcal{H}_2 \otimes \cdots \otimes \mathcal{H}_n , \quad (2.18)$$

the tensor product between  $n$  single qubit systems. A basis for  $\mathcal{H}_{\text{comp}}$  can then be obtained the same way:

$$\begin{aligned} |HH \dots HH\rangle &= |H\rangle_1 \otimes |H\rangle_2 \otimes \cdots \otimes |H\rangle_{n-1} \otimes |H\rangle_n \\ |HH \dots HV\rangle &= |H\rangle_1 \otimes |H\rangle_2 \otimes \cdots \otimes |H\rangle_{n-1} \otimes |V\rangle_n \\ &\vdots \\ |VV \dots VV\rangle &= |V\rangle_1 \otimes |V\rangle_2 \otimes \cdots \otimes |V\rangle_{n-1} \otimes |V\rangle_n . \end{aligned} \quad (2.19)$$

If a pure state can be expressed as the tensor product of single qubit states

$$|\psi\rangle_{\text{comp}} = |\phi\rangle_1 \otimes \cdots \otimes |\phi\rangle_n = \bigotimes_{j=1}^n |\phi\rangle_j , \quad (2.20)$$

it is called *fully separable* or *product state*. If such a decomposition is not possible for a certain state it is called *non-separable* or *entangled*.

In order to also describe mixed multi-qubit states, the density matrix formalism is generalised. Just like Eq. (2.15) in the single qubit case, one can express the density matrix of a multi-qubit state as a linear combination of tensor products of Pauli matrices,

$$\rho = \frac{1}{2^n} \sum_{s_1, \dots, s_n=0}^3 T_{s_1 \dots s_n} \bigotimes_{j=1}^n \sigma_{s_j} \quad (2.21)$$

with weights  $T$  again the expectation values

$$T_{\mathbf{s}} = T_{s_1 \dots s_n} = \text{Tr} \left( \rho \bigotimes_{j=1}^n \sigma_{s_j} \right) \quad (2.22)$$

and the indices  $s_j \in \{0, 1, 2, 3\}$  for all  $j = 1, \dots, n$ .  $T$  is often called *correlation tensor*, while its single elements  $T_{\mathbf{s}}$  are named *correlations*.

### 2.4. Entanglement

Entanglement is a strictly quantum feature that can emerge in multi-qubit systems, when it is not possible to assign a separate wave function to each single qubit, as described above. This leads to some very interesting properties not present in classical physics, which are best described with an example. Let us take the state

$$|\phi_+\rangle = \frac{1}{\sqrt{2}} (|H\rangle_A \otimes |H\rangle_B + |V\rangle_A \otimes |V\rangle_B) \equiv \frac{1}{\sqrt{2}} (|HH\rangle + |VV\rangle) , \quad (2.23)$$

which is one of the Bell states (for details see Section 2.5.1).

First, if we perform a measurement on only one of the two qubits, we get random results for every basis. This is best seen by using the density matrix formalism and partially tracing out one system to obtain the state of the other,

$$\mathrm{Tr}_A (|\phi_+\rangle\langle\phi_+|) = \sum_{i=\{H,V\}} \langle i|_A |\phi_+\rangle\langle\phi_+| |i\rangle_A = \frac{1}{2} (|H\rangle_B\langle H|_B + |V\rangle_B\langle V|_B) = \frac{1}{2} \mathbf{1}_B^{(2)}, \quad (2.24)$$

the maximally mixed state.

Second, the state exhibits correlations between the two quantum particles in more than one basis. One can see straight away the correlations in the computational basis: If we measure the first qubit to be in state  $|H\rangle_A$  ( $|V\rangle_A$ ), we will automatically measure the second qubit in the same state. But this is also true for other bases,

$$\frac{1}{\sqrt{2}} (|HH\rangle + |VV\rangle) = \frac{1}{\sqrt{2}} (|PP\rangle + |MM\rangle) = \frac{1}{\sqrt{2}} (|RL\rangle + |LR\rangle), \quad (2.25)$$

as can easily be calculated by means of Eq. (2.7)-Eq. (2.10).

These correlations occur at arbitrarily large distances with a speed at least a few orders of magnitude above the speed of light [18] and cannot be explained classically. They led to interesting discussions about the foundations of quantum mechanics, most notably the EPR-Paradox [4], followed by the derivation of the Bell inequalities [19, 20] and the experimental verification of these [21, 22].

### 2.4.1. Types of entanglement

Different classes of entanglement occur when considering more than two qubits. In case of three qubits,  $A$ ,  $B$  and  $C$ , there is not only the option that a pure state is fully separable, namely  $|\psi\rangle = |\psi_A\rangle \otimes |\psi_B\rangle \otimes |\psi_C\rangle$  (often also written as  $A|B|C$ ) or entangled ( $ABC$ ), but it is also possible that the state is *biseparable* (e.g.  $|\psi\rangle = |\psi_A\rangle \otimes |\psi_{BC}\rangle$  for  $A|BC$ ) and there are in fact two different kinds of *tripartite* entanglement, the GHZ-type and the W-type [13]. All these possibilities are depicted in Figure 2.2. This classification, as well as generalisations to more qubits, is based on equivalence under *stochastic local operations and classical communication* (SLOCC). Further information on the subject can be found in Ref. [16, 23].

#### Genuine multipartite entanglement

*Genuine multipartite entanglement* (or *true multipartite entanglement*) is a special form of entanglement with entanglement between all parties. Additionally, a decomposition into states that are separable with respect to some partitions must not be possible. For example, a state

$$\rho = \alpha\rho_A \otimes \rho_{BC} + \beta\rho_{AB} \otimes \rho_C \quad (2.26)$$

would not be genuinely multipartite entangled. Please note that some entanglement witnesses (see Section 2.4.3) or the negativity (see Section 2.4.2) could still certify entanglement (if  $\rho_{BC}$  and  $\rho_{AB}$  are both entangled).

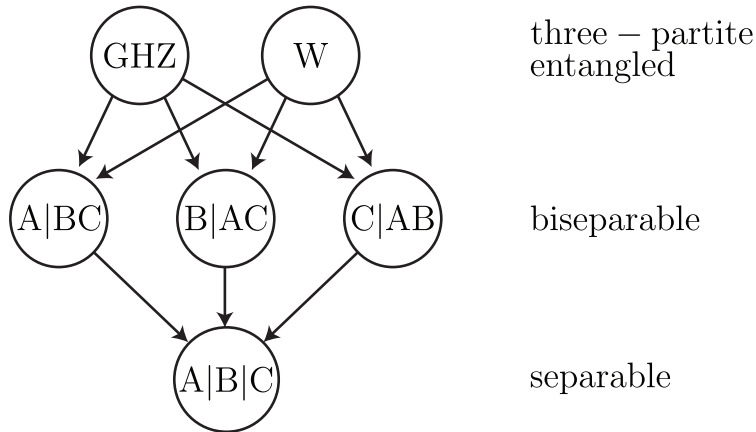


**Figure 2.2.: Types of entanglement in pure states.** In the three qubit case, there are different classes of entanglement – tripartite entangled states, subdivided into GHZ-type and W-type entanglement, biseparable states with entanglement between only two parties, and fully separable states.

### 2.4.2. Entanglement measures

Even though the definition of separability Eq. (2.20) is straightforward, it is experimentally and computationally very difficult to confirm entanglement for arbitrary quantum states. But for experimentalists, it is of course vital to confirm that the prepared state is indeed entangled and, if possible, to quantify the present entanglement. There are three broadly accepted conditions an entanglement measure should fulfil:

- $E(\rho_{\text{sep}}) = 0$  (vanishes for separable states)
- $E(\Lambda_{\text{LOCC}}\rho\Lambda_{\text{LOCC}}) \leq E(\rho)$  (does not increase using LOCC)
- $E(\lambda\rho_1 + (1 - \lambda)\rho_2) \leq \lambda E(\rho_1) + (1 - \lambda)E(\rho_2)$  (is convex)

Here, just a short overview over different entanglement measures is given; for a more detailed description see Ref. [3, 16, 24].

### Entropy and entanglement of formation

As seen before, one part of a Bell state appears as white noise if observed individually, while tracing out one qubit of a pure separable state results in a pure residual state. This property can be quantified for an entanglement measure called *entropy*,

$$E_S(\rho_{AB}) = S(\text{Tr}_A(\rho_{AB})) = S(\text{Tr}_B(\rho_{AB})) \tag{2.27}$$

with the von Neumann entropy  $S(\rho) = -\text{Tr}(\rho \log_2(\rho))$ . The biggest problem with this approach is that it works only for pure states (the mixedness in the residual state can result from entanglement but also from mixedness of the whole state). A generalisation to mixed states can be done and is called *entanglement of formation*  $E_F$ . It is calculated by minimising over all possible decompositions of the mixed state

$$E_F(\rho) = \text{Inf}_{\rho = \sum_i p_i |\psi_i\rangle\langle\psi_i|} \sum_i p_i E_S(|\psi_i\rangle) , \tag{2.28}$$

but this minimisation is quite arduous. Fortunately, an explicit form

$$E_F(\rho) = h\left(\frac{1 + \sqrt{1 - C^2(\rho)}}{2}\right), \quad (2.29)$$

can be found [25] with the *concurrence*  $C = \max(0, \sqrt{\lambda_1} - \sqrt{\lambda_2} - \sqrt{\lambda_3} - \sqrt{\lambda_4})$ , defined by the eigenvalues  $\lambda_i$  of the state  $\rho$ , and the binary entropy function  $h(x) = -x \log_2 x - (1 - x) \log_2(1 - x)$ .

### Negativity

The *negativity* is an entanglement measure originating in the Peres-Horodecki criterion [26]. It uses a positive map, e.g. transposition of the density matrix. If a positive map is acting on a part of a separable state, the resulting state will be physical, but if it is acting on a part of an entangled state, this is not necessarily so. Therefore, two states are entangled if the partially transposed density matrix has a negative eigenvalue. This is a necessary criterion for all states, but sufficient only for qubit-qubit and qubit-qutrit systems. The negativity as a measure can then be defined as

$$E_N = \frac{1}{2} \sum_i \left( |\lambda_i^T| - \lambda_i^T \right), \quad (2.30)$$

where  $\lambda_i^T$  are the eigenvalues of the partially transposed density matrix.

One problem with this entanglement measure is that it does not reliably detect entanglement in any dimension, as well as that the entanglement ordering is somewhat different to the entanglement of formation measure. Also, both measures introduced until now use the complete density matrix, whose determination requires an exponentially increasing (with the system size) measurement effort.

### 2.4.3. Entanglement witnesses

Another method to certify entanglement are linear *entanglement witnesses*. Such a witness is described by an operator  $\mathcal{W}$  such that

$$\text{Tr}(\mathcal{W}\rho) = 0 \quad (2.31)$$

defines a hyperplane in the convex space of mixed states, see Figure 2.3. One now has to choose  $\mathcal{W}$  in a way that  $\text{Tr}(\mathcal{W}\rho_{\text{sep}}) \geq 0$  for all separable states. Therefore, from

$$\text{Tr}(\mathcal{W}\rho) < 0 \quad (2.32)$$

it follows that  $\rho$  is an entangled state. This uses only the expectation value of  $\mathcal{W}$ , which is experimentally easier to determine than the complete density matrix.

There are always entangled states that are not detected by a witness, but it is normally not a problem to tailor a witness to detect entanglement around a certain target state. A big advantage of witnesses is that one does not have to perform a complete tomography as for the previous methods – the experimental and computational effort can be reduced tremendously.

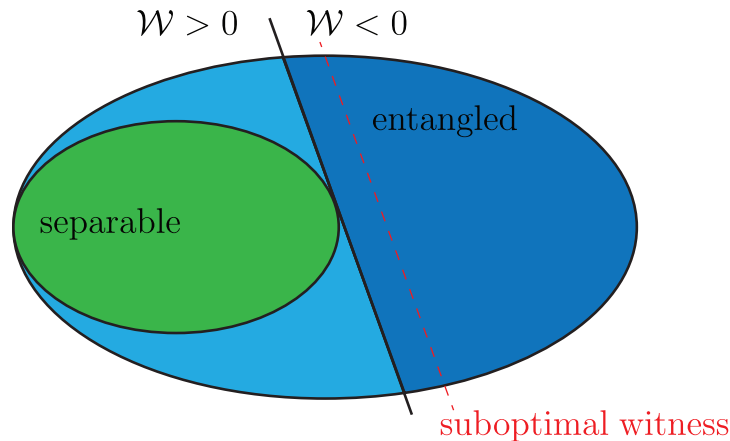


**Figure 2.3.: Schematic of an entanglement witness.** The hyperplane defined by the witness (black line) separates the state space into two parts. One of these parts (where  $\text{Tr}(\mathcal{W}\rho) > 0$ ) contains all separable states (green), such that entanglement is proven for  $\text{Tr}(\mathcal{W}\rho) < 0$ . Entangled states lying in the light blue region are not detected by the witness. The red dashed line shows another, suboptimal witness verifying entanglement for less states.

There is a generic way to define a *fidelity based* witness  $\mathcal{W}_\psi$  to detect entanglement in the vicinity of a pure state  $|\psi\rangle$ :

$$\mathcal{W}_\psi = \alpha \mathbb{1} - |\psi\rangle\langle\psi|, \quad (2.33)$$

with  $\alpha = \sup_{\phi_{\text{sep}}} |\langle\phi_{\text{sep}}|\psi\rangle|$  for the optimal witness [16]. There is also a connection between the value of a witness and the strength of entanglement, as seen in [27, 28].

## 2.5. Relevant states and their properties

Apart from the important one-qubit eigenstates of the Pauli matrices defined in Section 2.1, there are a number of important multi-qubit states. This section concentrates on some prominent states appearing in this thesis and examines their properties.

### 2.5.1. Bell states

Named after J.S.Bell because of their relation to the Bell inequalities [19], *Bell states* are maximally entangled 2-qubit states. The four Bell states

$$\begin{aligned} |\phi_+\rangle &= \frac{1}{\sqrt{2}} (|HH\rangle + |VV\rangle), \\ |\phi_-\rangle &= \frac{1}{\sqrt{2}} (|HH\rangle - |VV\rangle), \\ |\psi_+\rangle &= \frac{1}{\sqrt{2}} (|HV\rangle + |VH\rangle) \text{ and} \\ |\psi_-\rangle &= \frac{1}{\sqrt{2}} (|HV\rangle - |VH\rangle) \end{aligned} \quad (2.34)$$

make up a basis of the 2-qubit state space (like the computational basis Eq. (2.19)). The Bell states are transformed into each other by unitary transformations on only one qubit,

$$|\phi_+\rangle = (\mathbb{1} \otimes \sigma_z) |\phi_-\rangle = (\mathbb{1} \otimes \sigma_x) |\psi_+\rangle = i(\mathbb{1} \otimes \sigma_z) |\psi_-\rangle , \quad (2.35)$$

meaning that such a local transformation has an effect on the whole bipartite state. This indicates entanglement, as well as the behaviour when tracing out one of the qubits and correlations in multiple bases (already seen in Section 2.4).

### 2.5.2. Greenberger-Horne-Zeilinger states

A generalisation of the  $|\phi_+\rangle$ -Bell state for three and more qubits is the *Greenberger-Horne-Zeilinger* (GHZ) state [29]

$$|\text{GHZ}\rangle = \frac{1}{\sqrt{2}} (|HH \cdots H\rangle + |VV \cdots V\rangle) . \quad (2.36)$$

Like the Bell states, the GHZ state loses its entanglement when partially tracing out one of the qubits,

$$\begin{aligned} \text{Tr}_A |\text{GHZ}_n\rangle &= \text{Tr}_A \left( \frac{1}{2} (|HH \cdots H\rangle + |VV \cdots V\rangle) (|HH \cdots H\rangle + |VV \cdots V\rangle) \right) \\ &= \frac{1}{2} (|H \cdots H\rangle \langle H \cdots H| + |V \cdots V\rangle \langle V \cdots V|) , \end{aligned} \quad (2.37)$$

resulting in a mixed state of reduced dimension.

Because of their correspondence to the Bell states and Bell inequalities [30], GHZ states are often referred to as maximally entangled. However, this classification depends strongly on the used measure. E.g., using the negativity (see Section 2.4.2) results in a value of only 0.5 for the 4-qubit GHZ state but reaches over 0.8 for a Dicke state.

### 2.5.3. Graph states

*Graph states* are multipartite entangled states that can be represented by a mathematical graph. In this context, qubits are depicted as vertices of the graph while its edges correspond to interactions between qubits, see Figure 2.4. For example, the already introduced GHZ state is a star-like graph state. Another important class of graph states are the *cluster states*.

### 2.5.4. Cluster states

Special cases of graph states where the vertices are connected in linear fashion are called *cluster states* [31]. This is for example the case for  $n$  one-dimensionally arranged qubits, each having only next-neighbour interactions. The 4-qubit Cluster state

$$|\mathcal{C}_4\rangle = \frac{1}{2} (|HHHH\rangle + |HHVV\rangle + |VVHH\rangle - |VVVV\rangle) \quad (2.38)$$

is depicted in Figure 2.4. Cluster states are useful for one-way quantum computing [32], and show high *entanglement persistency*, meaning that one can measure (in the 4-qubit cluster state) up to two qubits without losing the entanglement [33].

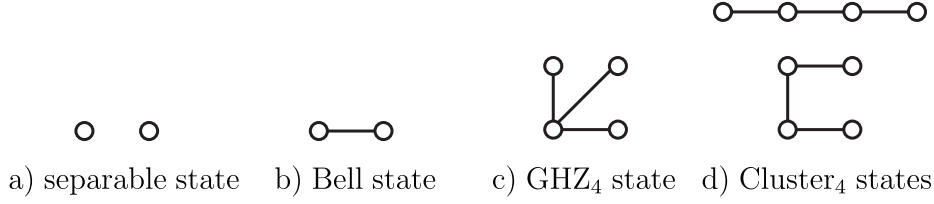


**Figure 2.4.: Different graph states.** Qubits are represented as vertices of a graph while interactions between them are depicted as the edges of the graph. Separable states (a), Bell states (b) and GHZ states (c) were already introduced and can be represented by graphs. (d) shows representations of the cluster state.

### 2.5.5. Dicke states

*Dicke states* [34] are permutationally invariant, i.e. they are fully symmetric under exchange of any qubits. The Dicke state  $|D_N^{(e)}\rangle$  is the  $N$ -qubit symmetric state with  $e$  excitations, such that  $e$  qubits are in an excited state and  $N - e$  in the respective ground state. For example, the four-qubit Dicke state with two excitations

$$|D_4^{(2)}\rangle \propto |HHVV\rangle + |HVHV\rangle + |HVVH\rangle + |VHHV\rangle + |VHVH\rangle + |VVHH\rangle \quad (2.39)$$

is a superposition of all permutations of  $|HHVV\rangle$ . As the cluster states, Dicke states show a relatively high entanglement persistency [35].

## 2.6. Photon processing

To experimentally prepare, manipulate and observe entanglement in photonic quantum states, one needs to employ several different optical components. First of all, a source of entangled photons is introduced in this section, followed by polarisation controlling devices, beam splitters and photo detectors.

### 2.6.1. Spontaneous parametric down conversion

The process of *spontaneous parametric down conversion* (SPDC) is based on nonlinear optics. An electromagnetic field  $\mathbf{E}$  induces a polarisation

$$\mathbf{P} = \epsilon_0 \left( \sum_{j=1}^3 \chi_{ij}^{(1)} E_j + \sum_{j=1}^3 \sum_{k=1}^3 \chi_{ijk}^{(2)} E_j E_k + \sum_{j=1}^3 \sum_{k=1}^3 \sum_{l=1}^3 \chi_{ijkl}^{(3)} E_j E_k E_l + \dots \right) \quad (2.40)$$

in a dielectric crystal (e.g. made of beta barium borate or BBO in short), where  $\epsilon_0$  is the permittivity for vacuum and  $\chi^{(\cdot)}$  are the susceptibilities. Since higher orders of  $\chi$  are very small, one needs high pump powers and therefore strong fields to notice their effects. SPDC uses a second order effect called *three-wave mixing*, where a single pump photon  $\hbar\omega_p$  can decay into two photons called *signal*  $\hbar\omega_s$  and *idler*  $\hbar\omega_i$ , respectively. Obviously, in the particle picture conservation of momentum

$$\hbar\mathbf{k}_p = \hbar\mathbf{k}_s + \hbar\mathbf{k}_i \quad (2.41)$$

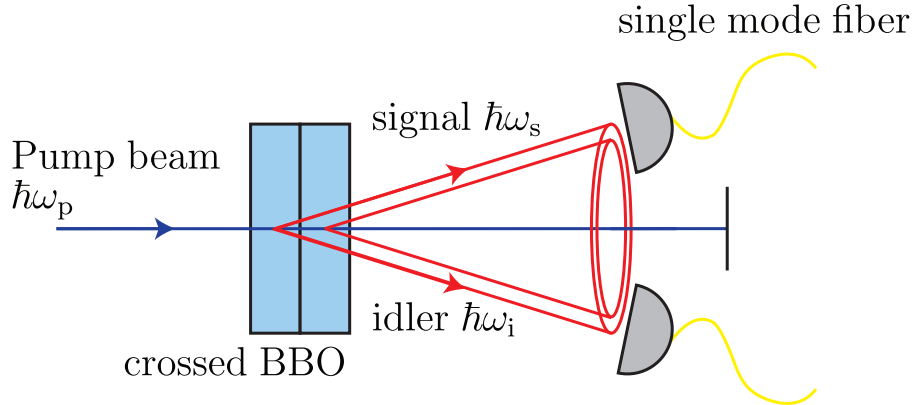


**Figure 2.5.: SPDC Type I.** Pumping the two crossed BBO crystals results in two emission cones. Entangled photon pairs have to be gathered at diametrically opposed sides of the cones, and such that they could have come from either crystal. That way, a created photon pair is in a superposition of originating from the first crystal and the second crystal, resulting in the superposition of  $|HH\rangle$  and  $|VV\rangle$ . Coupling into a single mode fiber can be used for spatial mode filtering.

and energy

$$\hbar\omega_p = \hbar\omega_s + \hbar\omega_i \quad (2.42)$$

have to apply. In the wave picture, these relations are called *phase-matching* and *frequency-matching* condition, respectively. Since the photons should be distinguished only spatially and by their polarisation, they have to be indistinguishable otherwise. To achieve this, we collect only photons with about half the frequency of the pump beam. Momentum conservation then ensures that the two photons are emitted symmetrically around the pump beam. It is commonly differentiated between *Type I* and *Type II* SPDC, where the created photons are parallelly and orthogonally polarised to each other, respectively. In both cases, the polarisation of the incoming pump photon is aligned to the optical axis of the nonlinear crystal, but the crystals have to be cut differently [16, 36]. Type II SPDC is not explained further since only Type I SPDC is used in this thesis.

**Type I SPDC** In Type I SPDC, signal and idler photons are both ordinarily polarised, i.e. orthogonal to the optical axis of the crystal and to the pump beam. Depending on the orientation, only the product states  $|HH\rangle$  or  $|VV\rangle$  are produced and emitted into a cone. To create polarisation entanglement, two crossed crystals with overlapping emission cones are needed, see Figure 2.5. It is important that the photons cannot be distinguished spatially, therefore the two individual crystals have to be very thin [37]. Pumping with photons in a state  $\frac{1}{\sqrt{2}}(|H\rangle + e^{i\varphi}|V\rangle)$  (e.g.  $|+\rangle$  with  $\varphi = 0$ ), the entangled state

$$|\psi_{SPDC1}\rangle = \frac{1}{\sqrt{2}}(|VV\rangle + e^{i\varphi}|HH\rangle) \quad (2.43)$$

(e.g.  $|\phi_+\rangle$  with  $\varphi = 0$ ) is created. More theory and a detailed description of the crystals and their orientation can be found in Ref. [36].

### 2.6.2. Yttrium-Vanadate crystals

*Yttrium Vanadate crystals* ( $\text{YVO}_4$ ) are used to control the phase between horizontal and vertical polarisation. These birefringent crystals are rotatable around their optical axis, applying the transformation

$$\begin{aligned} U_{\text{YVO}_4}(\varphi) &= \begin{pmatrix} i \cos\left(\frac{\varphi}{2}\right) + \sin\left(\frac{\varphi}{2}\right) & 0 \\ 0 & i \cos\left(\frac{\varphi}{2}\right) - \sin\left(\frac{\varphi}{2}\right) \end{pmatrix} \\ &= i \cos\left(\frac{\varphi}{2}\right) \sigma_0 + \sin\left(\frac{\varphi}{2}\right) \sigma_z. \end{aligned} \quad (2.44)$$

Since  $\cos(\theta/2) + i \sin(\varphi/2) = \exp(i\varphi/2)$ , the transformation

$$U_{\text{YVO}_4}(\varphi) = -e^{-i\varphi/2} \begin{pmatrix} 1 & 0 \\ 0 & e^{i\varphi} \end{pmatrix} \quad (2.45)$$

corresponds to a relative phase shift of  $\varphi$ .

### 2.6.3. Waveplates

*Waveplates* are also birefringent and therefore have different refraction indices for the ordinary (polarised perpendicular to the optical axis) and the extraordinary (polarised parallel to the optical axis) beam, resulting in a differing retardation and therefore leading to a phase difference between these modes. If this phase difference corresponds to  $\Delta\varphi = \pi$ , one speaks of a *half-wave plate* (HWP), in case of  $\Delta\varphi = \pi/2$  of a *quarter-wave plate* (QWP). With the rotation angle of the waveplate  $\theta$ , the transformation matrices are given by

$$\begin{aligned} U_{\text{HWP}}(\theta) &= \begin{pmatrix} \cos(2\theta) & \sin(2\theta) \\ \sin(2\theta) & -\cos(2\theta) \end{pmatrix} \\ &= \sin(2\theta) \sigma_x + \cos(2\theta) \sigma_z \end{aligned} \quad (2.46)$$

for the half-wave plate and by

$$\begin{aligned} U_{\text{QWP}}(\theta) &= \begin{pmatrix} \cos^2(\theta) - i \sin^2(\theta) & (1+i) \sin(\theta) \cos(\theta) \\ (1+i) \sin(\theta) \cos(\theta) & -i \cos^2(\theta) + \sin^2(\theta) \end{pmatrix} \\ &= \frac{1}{2} ((1-i)\sigma_0 + 2(1+i) \sin(\theta) \cos(\theta) \sigma_x + (1+i) \cos(2\theta) \sigma_z) \end{aligned} \quad (2.47)$$

for the quarter-wave plate. For example, the state  $|H\rangle$  can be transformed

$$U_{\text{HWP}}(\pi/8) |H\rangle = |P\rangle \quad (2.48)$$

$$U_{\text{QWP}}(\pi/4) |H\rangle = e^{-i\pi/4} |R\rangle \quad (2.49)$$

to the orthogonal states  $|P\rangle$  or  $|R\rangle$ .

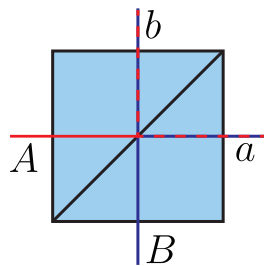


**Figure 2.6.: Schematic of a beam splitter.** A beam splitter with its two input modes  $A$  and  $B$  and its two output modes  $a$  and  $b$ .

### 2.6.4. Beam splitters

Another very important optical component is the *beam splitter*, used to couple two input modes,  $A$  and  $B$ , with two output modes  $a$  and  $b$ . Most often, this is employed to split a single beam into two or to overlap two incoming beams, see Figure 2.6. Whether light incoming at  $A$  is transmitted to  $a$  or reflected to  $b$  generally depends on the polarisation.

The transmittivities  $T_H$  and  $T_V$  and reflectivities  $R_H$  and  $R_V$  characterise the beam splitter. Important special cases are the 50 : 50 beam splitter, where  $T_H^2 = T_V^2 = R_H^2 = R_V^2 = 0.5$  (the probability to transmit (to reflect) a photon is exactly one half, independent of polarisation), and the polarising beam splitter, where  $T_H = R_V = 1$  and  $T_V = R_H = 0$  (horizontally polarised photons are always transmitted and vertically polarised photons are always reflected).

## 2.7. Tomographic state reconstruction

To determine the full density matrix of an experimentally prepared state, it is necessary to perform measurements in different bases and combine the results accordingly. Commonly, a procedure like that is referred to as *quantum state tomography* (QST). This section focuses first on a *linear inversion* scheme, then explains the nonlinear method of *maximum likelihood estimation*.

### 2.7.1. Measurements

Measurements of the polarisation of photons are performed by a *polarisation analysis* (PA) setup as shown in Figure 2.7. A polarising beam splitter spatially separates different polarisations and leads them to single photon detectors (e.g. avalanche photo diodes, short APDs) to be detected. The basis can be changed by rotating the half- and quarter-wave plates in front of the beam splitter – rotating the polarisation of the photon is equivalent to actually rotating the measurement basis. With this approach, two measurements are performed simultaneously, e.g. horizontally and vertically polarised photons can be detected with the same angles of the wave plates. For the measurement of diagonally polarised photons, a half-wave plate at  $22.5^\circ$  rotates the polarisation by  $45^\circ$

$$U_{\text{QWP}}(0)U_{\text{HWP}}\left(\frac{\pi}{8}\right)|P\rangle = |H\rangle \quad (2.50)$$

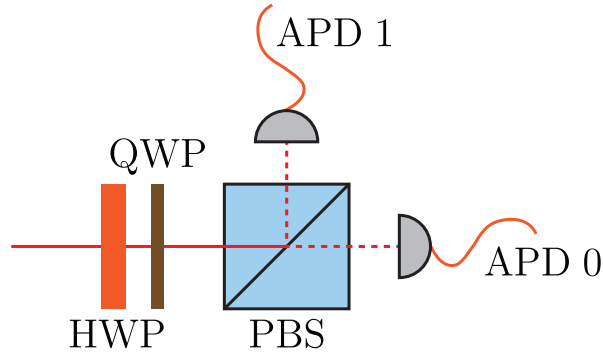


**Figure 2.7.: Setup of polarisation analysis (PA).** Incoming photons are first directed through a pair of half- and quarter-wave plates to change the measurement basis. A polarising beam splitter spatially separates the photons into two output modes, where they are collected into multi mode fibers guiding them to single photon detectors.

such that a click in APD 0 corresponds to a projection onto  $|P\rangle$  and a click in APD 1 corresponds to a projection onto  $|M\rangle$ . All angle settings for measuring the important single qubit states Eq. (2.5)-Eq. (2.10) are listed in Table 2.1. In a typical experiment, the source produces a stream of identically prepared photons, so that one can count the detection events  $c_i^s$  in the APD  $i$  occurring during a given time for every setting  $s \in \{1, 2, 3\} \equiv \{x, y, z\}$ .

**Table 2.1.: Settings of the wave plates for polarisation analysis.** A click in a given APD while having the wave plates set at certain angles corresponds to a projection onto a specific state. For every setting, the experiment runs for a fixed time and the number of counts in each APD can be measured. From a single setting, multiple count rates can be measured leading to the expectation value of one of the Pauli matrices.

Projection onto	Angle of HWP	Angle of QWP	Click in	Measured quantity
$ H\rangle$	$0^\circ$	$0^\circ$	APD 0	$c_0^z$ } $T_3 \equiv T_z = \langle \sigma_z \rangle$
$ V\rangle$	$0^\circ$	$0^\circ$	APD 1	
$ P\rangle$	$22.5^\circ$	$0^\circ$	APD 0	$c_0^x$ } $T_1 \equiv T_x = \langle \sigma_x \rangle$
$ M\rangle$	$22.5^\circ$	$0^\circ$	APD 1	
$ R\rangle$	$0^\circ$	$45^\circ$	APD 0	$c_0^y$ } $T_2 \equiv T_y = \langle \sigma_y \rangle$
$ L\rangle$	$0^\circ$	$45^\circ$	APD 1	

Performing all of these 6 measurements corresponds to an *overcomplete tomography* since it is sufficient to determine 3 parameters to fully describe a single qubit state. A tomography scheme with only 4 (the fourth measurement is needed to exclude the influence of the total photon flux) projection measurements (projection onto  $|H\rangle$ ,  $|V\rangle$ ,  $|P\rangle$  and  $|R\rangle$ ) is presented in [38]. Nevertheless, since the setup described above can detect orthogonally polarised photons simultaneously, it is more convenient (and usually leads to better results [39]) to perform such an overcomplete tomography scheme.

This scheme can be generalised to  $n$  spatially separated qubits encoded on the polarisational degree of freedom straightforwardly. One polarisation analysis setup is needed for every photon, and the 3 settings given in Table 2.1 have to be combined in every possible way,

resulting in  $3^n$  measurement settings. Instead of only single counts  $c_i^s$ ,  $n$ -fold coincidences  $c_{i_1 \dots i_n}^{s_1 \dots s_n}$  are recorded, making it possible to perform  $2^n$  measurements simultaneously.

Using the count rates, the respective frequencies

$$f_{i_1 \dots i_n}^{s_1 \dots s_n} = \frac{c_{i_1 \dots i_n}^{s_1 \dots s_n}}{N_{s_1 \dots s_n}} \quad (2.51)$$

can be determined with total counts  $N_{s_1 \dots s_n} = \sum_{i_1, \dots, i_n} c_{i_1 \dots i_n}^{s_1 \dots s_n}$  of setting  $\mathbf{s} = (s_1, \dots, s_n)$ .

### 2.7.2. Linear inversion

For state reconstruction by *linear inversion* (LIN), the expression Eq. (2.21) for the density matrix

$$\rho = \frac{1}{2^n} \sum_{s_1, \dots, s_n=0}^3 T_{s_1 \dots s_n} \bigotimes_{j=1}^n \sigma_{s_j} \quad (2.52)$$

is used with the correlation tensor  $T$ . Full correlations can be calculated directly

$$T_{s_1 \dots s_n} = \sum_{i_1, \dots, i_n=0}^1 g(i_1, \dots, i_n) f_{i_1 \dots i_n}^{s_1 \dots s_n} \quad (2.53)$$

from the observed frequencies, where  $g = (-1)^{\sum_j i_j}$  is a parity function determining the sign of the contributions. Non-full correlations can be determined from multiple settings, e.g.  $T_{0z}$  could be calculated by using results from measuring either in the setting  $xz$ ,  $yz$  or  $zz$ , because the measurement result on the first qubit just has to be neglected. Consequently,  $T_{0s_2 \dots s_n}$  can be calculated using e.g. the setting  $S = xs_2 \dots s_n$ ,

$$T_{0s_2 \dots s_n} = \sum_{i_1, \dots, i_n=0}^1 g'(x, \dots, s_n, i_1, \dots, i_n) f_{i_1 \dots i_n}^{xs_2 \dots s_n}, \quad (2.54)$$

with a different parity function  $g' = (-1)^k$ , where

$$k = \sum_{j=1}^n (\delta_{s_j, x} + \delta_{s_j, y} + \delta_{s_j, z}) i_j \quad (2.55)$$

counts only relevant results of nonzero settings  $s_j$ . To reduce the variance of these non-full correlations, one takes the mean over all possible ways to compute it. Using this and substituting the correlation tensor in Eq. (2.52), a general expression for the density matrix

$$\rho = \frac{1}{2^n} \sum_{s_1, \dots, s_n=1}^3 \sum_{i_1, \dots, i_n=0}^1 f_{i_1 \dots i_n}^{s_1 \dots s_n} \bigotimes_{j=1}^n \left( \frac{1}{3} \sigma_0 + (-1)^{i_j} \sigma_{s_j} \right) \quad (2.56)$$

is obtained. For a more detailed derivation, refer to [16].

In the special case of a single qubit, the density matrix is obtained by means of Eq. (2.15)

$$\rho = \frac{1}{2} (\mathbb{1}_2 + T_x \sigma_x + T_y \sigma_y + T_z \sigma_z) = \frac{1}{2} \sum_{s=0}^3 T_s \sigma_s \quad (2.57)$$

with

$$T_0 = 1; \quad T_x = \frac{c_0^x - c_1^x}{c_0^x + c_1^x}; \quad T_y = \frac{c_0^y - c_1^y}{c_0^y + c_1^y}; \quad T_z = \frac{c_0^z - c_1^z}{c_0^z + c_1^z} \quad (2.58)$$

for the correlation tensor elements.

### 2.7.3. Maximum likelihood estimation

Since the measured quantities and frequencies are inherently subject to statistical fluctuations, the density matrix obtained by linear inversion is not necessarily physical, i.e. it can show negative eigenvalues. In the single qubit case, theoretically reachable, linearly reconstructed states lie in a cube containing the Bloch sphere of physical states. To restrict the results to these physical states, a fit algorithm is needed. A widely used method is the *maximum likelihood estimation* (MLE), calculating the physical state *most likely* to produce the measurement results. To quantify the likelihood, one first considers the probability

$$p_\rho(\mathbf{i}|\mathbf{s}) = \text{Tr}(\rho \mathcal{P}_i^{\mathbf{s}}) \quad (2.59)$$

for a single measurement result  $\mathbf{i} \equiv (i_1, \dots, i_n)$  (on all qubits  $1, \dots, n$ ) in a setting  $\mathbf{s}$ , given a certain state  $\rho$ .  $\mathcal{P}_i^{\mathbf{s}}$  denotes the projection operator corresponding to the measurement result, e.g.  $\mathcal{P}_{10}^{zz} = |VH\rangle\langle VH|$ . The likelihood function for all measurement results

$$\mathcal{L}(\rho) = \prod_{j=1}^N p_\rho(\mathbf{i}_j|\mathbf{s}_j) \quad (2.60)$$

is then just the product of all probabilities for the single events. Of course, one can group equal terms,

$$\mathcal{L}(\rho) = \prod_{\mathbf{i}, \mathbf{s}} p_\rho(\mathbf{i}|\mathbf{s})^{c_i^{\mathbf{s}}}, \quad (2.61)$$

where the product now runs over all results in all settings. To obtain the state  $\rho$ , this likelihood function needs to be maximised

$$\rho = \arg \max_{\rho \geq 0} \mathcal{L}(\rho) \quad (2.62)$$

where  $\rho \geq 0$  ensures physicality. Since it is computationally easier, provides better scaling and is possible because of the monotony of the logarithm, the *log-likelihood*

$$\mathcal{L}_l(\rho) = \log \mathcal{L}(\rho) = \sum_{\mathbf{i}, \mathbf{s}} c_i^{\mathbf{s}} \log p_\rho(\mathbf{i}|\mathbf{s}) \quad (2.63)$$

is often minimised instead of maximising Eq. (2.61).

### 2.7.4. Distances and metrics on Hilbert spaces

After the quantum mechanical state has been reconstructed, it is often important for an experimentalist to know how close the prepared state is to a given target state. Therefore, metrics and distances on the Hilbert space have to be defined. A metric  $D$  has to fulfil:

- $D(\rho_1, \rho_2) \geq 0$  (non-negativity)
- $D(\rho_1, \rho_2) = 0 \iff \rho_1 = \rho_2$  (Leibniz' Law)
- $D(\rho_1, \rho_2) = D(\rho_2, \rho_1)$  (symmetric in arguments)
- $D(\rho_1, \rho_2) \leq D(\rho_1, \rho_3) + D(\rho_3, \rho_2)$  (triangle inequality)

## Fidelity

Most experimentalists use the *fidelity*  $\mathcal{F}$  as a measure for state preparation and reconstruction quality. For pure states, it is defined as the overlap

$$\mathcal{F}(|\psi_1\rangle, |\psi_2\rangle) = |\langle\psi_1|\psi_2\rangle|^2 \quad (2.64)$$

between two states  $|\psi_1\rangle$  and  $|\psi_2\rangle$ . Also based on the transition probability between two states, the *Uhlmann-Fidelity* [40, 41]

$$\mathcal{F}(\rho_1, \rho_2) = \left( \text{Tr} \sqrt{\sqrt{\rho_1} \rho_2 \sqrt{\rho_1}} \right)^2 \quad (2.65)$$

can be defined for mixed states. The fidelity is not a metric (does not fulfill triangle inequality and Leibniz' Law), but the *Bures metric*

$$D_B(\rho_1, \rho_2) = \sqrt{2 - 2\sqrt{\mathcal{F}(\rho_1, \rho_2)}} \quad (2.66)$$

uses the fidelity as a parameter.

## Hilbert-Schmidt distance

The *Hilbert-Schmidt distance* is also one of the more prominent measures for closeness of states. Calculated by

$$D_{HS}(\rho_1, \rho_2) = \sqrt{\text{Tr}(\rho_1 - \rho_2)^2}, \quad (2.67)$$

it already fulfills the requirements of a metric.



## 3. Multipartite entanglement detection with minimal effort

As one has already seen in Section 2.4, detecting entanglement can be a very demanding task especially for systems with a high number of qubits. Usually, it is even more difficult to certify *genuine multipartite entanglement* (see Section 2.4.1). Full quantum state tomography (QST) is of course possible, but, for an  $n$ -qubit state, requires determining  $4^n - 1$  parameters, i.e. the experimental effort scales exponentially with  $n$ . Procedures for QST needing less effort have been developed [42, 43], but one has to assume certain features of the underlying state, such as permutational invariance [44–46]. Other strategies to certify genuine multipartite entanglement focus on features like the ability to violate a Bell inequality more strongly [47], a sufficiently large component of a correlation tensor [48], or use a multipartite entanglement witness [49, 50]. But, up to now, all methods are either suitable for only a few specific states and can not be constructed for other states, or they still require a lot of experimental and computational effort.

In this chapter, a systematic method to construct non-linear multipartite entanglement witnesses (tailored to certain states) will be introduced. It is often sufficient to use data obtainable in only two measurement settings, corresponding to minimal experimental effort. These witnesses are then used to experimentally certify genuine fourpartite entanglement of the GHZ and cluster type, superpositions of those, and for the four-qubit Dicke and singlet state.

### 3.1. Theoretical background

This section will highlight the fundamental theory underlying the generation of entanglement witnesses for many qubits. The concepts of *correlation complementarity* and *cut-anticommutativity* will be introduced and used on the considered states. Parts of the theory are also presented in [51, 52].

#### 3.1.1. Correlation complementarity

The idea to construct nonlinear entanglement witnesses is based on the complementarity of expectation values of anticommuting operators. For simplicity, correlations  $T_{\mathbf{s}} = T_{s_1 \dots s_n}$  are used, as they correspond to the expectation values of tensor products of Pauli matrices  $\sigma_{\mathbf{s}} = \bigotimes_{j=1}^n \sigma_{s_j}$  (with the shorthand notation  $\mathbf{s} \equiv (s_1 \dots s_n)$ , where  $\mathbf{s}$  is an element of  $\mathcal{I} = \{0 \dots 00, 0 \dots 01, \dots, 3 \dots 33\}$ ), see Eq. (2.22).

The eigenvalues of these tensor products  $\sigma_s$  are  $\pm 1$  and therefore their expectation values are constrained to the interval  $[-1, 1]$ . Consequently, the correlations have to fulfill

$$T_s^2 \leq 1. \quad (3.1)$$

Together with the physicality condition on a density matrix  $\rho$ , various bounds for the summed squares of correlations can be deduced. For example, with a set of  $j$  pairwise commuting operators  $\{\sigma_s : s \in \mathcal{C} \subset \mathcal{I}\}$  defined by the set of indices  $\mathcal{C}$  one can find a common eigenstate and thus the bound

$$\sum_{s \in \mathcal{C}} T_s^2 \leq j \quad (3.2)$$

holds for all states. For a set of pairwise anticommuting operators  $\{\sigma_s : s \in \mathcal{A} \subset \mathcal{I}\}$  defined by  $\mathcal{A}$  one can find an eigenstate to only one operator of the set at a time, and the bound decreases to

$$\sum_{s \in \mathcal{A}} T_s^2 \leq 1. \quad (3.3)$$

Exemplarily, consider the single qubit Pauli operators  $\sigma_x$ ,  $\sigma_y$  and  $\sigma_z$ . As they are anticommuting, the bound

$$T_x^2 + T_y^2 + T_z^2 \leq 1 \quad (3.4)$$

is imposed on their expectation values  $T_x, T_y$  and  $T_z$ , corresponding to the condition of physicality Eq. (2.16).

### 3.1.2. Cut-anticommutativity

The concept of complementarity valid for the expectation values of anticommuting operators can be employed to detect genuine multipartite entanglement if it is generalised to *cut-anticommutativity*. Two operators  $A_1 \otimes B_1$  and  $A_2 \otimes B_2$  are called *cut-anticommuting* for the given bipartition  $A|B$  (speak: *A-cut-B*), in short  $A|B$ -anticommuting, if they locally anticommute on part  $A$  or on part  $B$ :

$$\{A_1 \otimes B_1, A_2 \otimes B_2\}_{A|B} = 0 \iff \{A_1, A_2\} = 0 \vee \{B_1, B_2\} = 0 \quad (3.5)$$

with  $\{A_1, A_2\} = A_1 A_2 + A_2 A_1$  denoting the anticommutator.

Then, using a set  $\mathcal{A}_{A|B}$  defining only operators that mutually commute, but  $A|B$ -anticommute, namely operators fulfilling

$$\{\sigma_{s_1}, \sigma_{s_2}\}_{A|B} = 0 \wedge [\sigma_{s_1}, \sigma_{s_2}] = 0, \quad (3.6)$$

Eq. (3.2) is valid for a general (entangled) state while a state separable with respect to the bipartition  $A|B$  has to fulfil an inequality like Eq. (3.3):

$$T_{s_1}^2 + T_{s_2}^2 \leq_{A|B}^{\text{SEP}} 1, \quad (3.7)$$

where  $\leq_{A|B}^{\text{SEP}}$  denotes that the inequality is valid for states separable to the bipartition  $A|B$ .

This means that the sum of squared expectation values  $T_s^2$  of operators that pairwise commute, but cut-anticommute for a given bipartition  $A|B$  can be used as a witness to rule out separability along that cut. If that is done for every cut, all possible biseparations can be disproven, consequentially proving genuine multipartite entanglement. It is often possible to

use the same two correlation measurements for all possible bipartitions, keeping experimental effort at a minimum. Keep in mind that non-full correlations, i.e. correlations with indices equal to 0, can be obtained from the measurement of a possible respective full correlation (with each 0 replaced by either 1, 2 or 3), see Eq. (2.54). In some cases, one can even create a single combined criterion capable of disproving separability along all cuts at once.

### Commutativity of tensor products of Pauli matrices

Since we are using tensor products of Pauli matrices  $\sigma_s = \bigotimes_{j=1}^n \sigma_{s_j}$ , please note that two such operators commute when they differ at even number of positions, excluding pairs involving the unit operator  $\sigma_0$ , and anticommute otherwise [52]. For example, the operators  $\sigma_{3333}$  and  $\sigma_{1111}$  commute, but  $A|BCD$ -anticommute.

### 3.1.3. Fourpartite non-linear entanglement witnesses for the GHZ state

The process of designing witnesses will now be explained and illustrated with an example. This section will first concentrate on the derivation of multiple witnesses for the fourpartite GHZ state and then explain the differences for a single criterion.

The fourpartite GHZ state features 15 non-trivial correlations, all equal to  $\pm 1$ , making it an ideal example to show the application of our entanglement criteria. All non-zero correlations are depicted in Table 3.1.

First, two correlation measurements  $\sigma_{\mathbf{k}^{(1)}}$  and  $\sigma_{\mathbf{k}^{(2)}}$  with  $\mathbf{k}^{(i)} = (k_1 k_2 k_3 k_4)$ ,  $k_l \in \{1, 2, 3\}$  have to be selected while keeping in mind that these measurements not only determine the value of the full correlations  $T_{\mathbf{k}^{(1)}}$  and  $T_{\mathbf{k}^{(2)}}$ , but can also be used to calculate some non-full correlations.  $\sigma_{\mathbf{k}^{(1)}}$  and  $\sigma_{\mathbf{k}^{(2)}}$  have to be chosen such that the emerging set of accessible correlations  $\{\sigma_s : \mathbf{s} \in \mathcal{S} \subset \mathcal{I}\}$

- contains, for each bipartition, at least two operators that commute but cut-anticommute for the respective cut
- has corresponding squared correlation tensor elements  $T_s^2$  as large as possible.

In case of the GHZ-state, one measurement is set apart from the others: By measuring in the  $zzzz$ -basis, i.e. the operator  $\sigma_{3333}$ , 7 non-zero elements of the correlation tensor can be inferred. These 7 correlations are highlighted in blue in Table 3.1. The second correlation measurement can be picked at random out of the remaining 8 correlations because

**Table 3.1.: All non-vanishing correlations of the four qubit GHZ state.** The correlations coloured in blue can be inferred from the setting  $\sigma_{3333}$  and those coloured in red can be deduced from  $\sigma_{1221}$ . Taken from [51].

$T_{0000}$	1	$T_{0033}$	1	$T_{0303}$	1	$T_{0330}$	1
$T_{3003}$	1	$T_{3030}$	1	$T_{3300}$	1	$T_{3333}$	1
$T_{2112}$	-1	$T_{2121}$	-1	$T_{2211}$	-1	$T_{2222}$	1
$T_{1111}$	1	$T_{1122}$	-1	$T_{1212}$	-1	$T_{1221}$	-1

the corresponding operators are equivalent for our purposes. Here,  $\sigma_{1221}$  (measuring in the basis  $xyyx$ ) was chosen, leading to the correlation  $T_{1221}$  printed in red. With these two measurements, we now have access to the set

$$\{\sigma_s : s \in \mathcal{S} \subset \mathcal{I}\} = \{\sigma_{0033}, \sigma_{0303}, \sigma_{0330}, \sigma_{3003}, \sigma_{3030}, \sigma_{3300}, \sigma_{3333}, \sigma_{1221}\}, \quad (3.8)$$

of 8 pairwise commuting operators while, for every cut, there are some that cut-anticommute.

For every possible cut, we only use the operators from the set that cut-anticommute for the given cut. For example, the operators  $\sigma_{0303}$ ,  $\sigma_{0330}$ ,  $\sigma_{3003}$  and  $\sigma_{3030}$   $AB|CD$ -anticommute with  $\sigma_{1221}$ . Any one of the first operators together with the last one can be used to make up a witness like

$$\mathcal{W}_{AB|CD}^{\text{GHZ}} = \frac{1}{2} \left( T_{3030}^2 + T_{1221}^2 \right) \leq_{\text{SEP}_{AB|CD}} \frac{1}{2}, \quad (3.9)$$

with the normalisation factor of  $1/2$ . An entangled state (like the GHZ state) can then achieve a maximal value of 1, while a state separable to the cut  $AB|CD$  is restricted to  $1/2$ . However, depending on the actual experiment and statistical noise, some correlations will be larger than others. Because four operators are  $AB|CD$ -anticommuting with  $\sigma_{1221}$ , we use their averaged squared expectation values and thus obtain the normalised witness

$$\mathcal{W}_{AB|CD}^{\text{GHZ}} = \frac{1}{2} \left( \frac{1}{4} \left( T_{0303}^2 + T_{0330}^2 + T_{3003}^2 + T_{3030}^2 \right) + T_{1221}^2 \right) \leq_{\text{SEP}_{AB|CD}} \frac{1}{2}. \quad (3.10)$$

As those four operators mutually  $AB|CD$ -commute, their contribution has lower weight in the optimal witness, as a state separable to the cut  $AB|CD$  can achieve high absolute values either for  $T_{0303}$ ,  $T_{0330}$ ,  $T_{3003}$ , and  $T_{3030}$  or for  $T_{1221}$ .

An interesting quantity for the comparison of entanglement witnesses is the *noise robustness*  $\mathcal{R}$ , i.e. the maximal amount of white noise that can be admixed to a pure entangled state, while the witness still detects the state to be entangled. In the case when used correlations are equal  $\pm 1$ , the noise robustness is directly related to the threshold  $\mathcal{T} = 1/2$ ,

$$\mathcal{R} = 1 - \sqrt{\mathcal{T}} = 1 - \frac{1}{\sqrt{2}} \quad (3.11)$$

since the white noise directly decreases the squared correlations.

The witnesses for the 6 remaining cuts

$$\mathcal{W}_{A|BCD}^{\text{GHZ}} = \frac{1}{2} \left( \frac{1}{4} \left( T_{3003}^2 + T_{3030}^2 + T_{3300}^2 + T_{3333}^2 \right) + T_{1221}^2 \right) \leq_{\text{SEP}_{A|BCD}} \frac{1}{2}, \quad (3.12)$$

$$\mathcal{W}_{B|ACD}^{\text{GHZ}} = \frac{1}{2} \left( \frac{1}{4} \left( T_{0303}^2 + T_{0330}^2 + T_{3300}^2 + T_{3333}^2 \right) + T_{1221}^2 \right) \leq_{\text{SEP}_{B|ACD}} \frac{1}{2}, \quad (3.13)$$

$$\mathcal{W}_{C|ABD}^{\text{GHZ}} = \frac{1}{2} \left( \frac{1}{4} \left( T_{0033}^2 + T_{0330}^2 + T_{3030}^2 + T_{3333}^2 \right) + T_{1221}^2 \right) \leq_{\text{SEP}_{C|ABD}} \frac{1}{2}, \quad (3.14)$$

$$\mathcal{W}_{D|ABC}^{\text{GHZ}} = \frac{1}{2} \left( \frac{1}{4} \left( T_{0033}^2 + T_{0303}^2 + T_{3003}^2 + T_{3333}^2 \right) + T_{1221}^2 \right) \leq_{\text{SEP}_{D|ABC}} \frac{1}{2}, \quad (3.15)$$

$$\mathcal{W}_{AC|BD}^{\text{GHZ}} = \frac{1}{2} \left( \frac{1}{4} \left( T_{0033}^2 + T_{0330}^2 + T_{3003}^2 + T_{3300}^2 \right) + T_{1221}^2 \right) \leq_{\text{SEP}_{AC|BD}} \frac{1}{2} \text{ and} \quad (3.16)$$

$$\mathcal{W}_{AD|BC}^{\text{GHZ}} = \frac{1}{2} \left( \frac{1}{4} \left( T_{0033}^2 + T_{0303}^2 + T_{3030}^2 + T_{3300}^2 \right) + T_{1221}^2 \right) \leq_{\text{SEP}_{AD|BC}} \frac{1}{2} \quad (3.17)$$

can be derived analogously and look very similar. Please note that all 7 criteria are based on the same data obtainable in only two measurement settings.

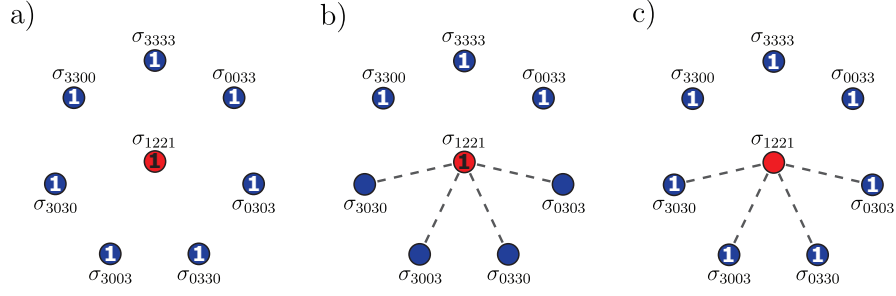


**Figure 3.1.: (Cut-)Anticommutativity graph for the GHZ witness.** All blue vertices are weighted with  $\alpha$  since they originate from the same measurement basis and behave similarly for the different cuts. The red vertex has weight  $\beta$ . There are no edges in the anticommutativity graph a), as all operators in the set  $\{\sigma_s : s \in \mathcal{S} \subset \mathcal{I}\}$  mutually commute. Thus, the value  $c = 1$  can be assigned to all vertices, resulting in a graph score  $G = 7\alpha + \beta$ . In case of  $AB|CD$ -anticommutativity, there are two possibilities, b) and c), as  $\sigma_{1221}$   $AB|CD$ -anticommutes with four other operators (dashed lines). These lead to the graph scores  $G_{AB|CD}^{(1)} = 3\alpha + \beta$  and  $G_{AB|CD}^{(2)} = 7\alpha$ , indicating the optimal weights  $4\alpha = \beta$ .

### 3.1.4. Constructing a single witness for all bipartitions

The increased computational effort needed to evaluate different witnesses for all possible bipartitions can be reduced by combining all criteria into a single witness. While this combined criterion is slightly less sensitive, it is very easy to apply, since the violation of a single threshold is enough to prove genuine multipartite entanglement. In order to determine the optimal single criterion, so-called *anti-commutativity graphs* are used. Such a graph is drawn for standard anticommutativity as well as for every cut-anticommutativity relation, see Figure 3.1.

First, all of the operators determined in the previous section  $\{\sigma_s : s \in \mathcal{S} \subset \mathcal{I}\}$  are represented by vertices of the graph. Weights  $v_i$  are assigned to each vertex (labeled by  $i$ ), initially free parameters that will later be used to optimize the witness. Then, connect vertices of (cut-)anticommuting operators, these are the edges of the graph. Now, values  $c_i^{(d)} \in \{0, 1\}$  can be assigned to the vertices, but two 1's cannot be connected directly by a line. There is more than one possible way to do this, so the different distributions are labeled by  $d$ . We calculate a maximal *graph score*

$$G_{(\text{cut})} = \max_d \sum_i c_i^{(d)} v_i, \quad (3.18)$$

still depending on the weights  $v_i$ . After the graph scores for the anticommutativity graph  $G$  and all cut-anticommutativity graphs  $\tilde{G}_j^{(d)}$  (label the different cuts with  $j$ ) are known, the optimal weights

$$\{v_i\} = \arg \min_{\{v_i\}} \max_{j,d} \frac{\tilde{G}_j^{(d)}}{G} \quad (3.19)$$

can be determined by minimising the maximal ratio  $\tilde{G}_j^{(d)}/G$ .

Then, the general normalised optimal witness

$$\mathcal{W} = \frac{1}{G} \sum_{s \in \mathcal{S}} T_s^2 \leq_{\text{BISEP}} \frac{\tilde{G}}{G} \quad (3.20)$$

is obtained. Please refer to Figure 3.2 for a flowchart as an overview of the procedure.

In case of the GHZ state, it is possible to assign equal weights  $\alpha$  to the 7 vertices representing operators derived from  $\sigma_{3333}$  because they behave symmetrically for the different cuts ( $\sigma_{1221}$  cut-anticommutes for 4 different biseparations and commutes for the remaining 3 with each of them). The vertex representing  $\sigma_{1221}$  is weighted with  $\beta$ . In the anticommutativity graph (Figure 3.1 a)), there are no edges and we can assign  $c = 1$  to all vertices, resulting in a graph score

$$G = 7\alpha + \beta . \quad (3.21)$$

For the cut-anticommutativity graphs, there are always some unconnected vertices that can have  $c = 1$ . Additionally, one can either assign a “1” to  $\sigma_{1221}$  or to the other remaining operators (Figure 3.1 b) and c)). The different cut-anticommutativity graph scores are then

$$\begin{aligned} G_j^{(1)} &= 3\alpha + \beta \\ G_j^{(2)} &= 7\alpha \end{aligned} \quad (3.22)$$

for all seven cuts  $j$ . The best noise robustness

$$\min_{\{v_i\}} \max_{j,d} \frac{G_j^{(d)}}{G} \quad (3.23)$$

is achieved when these two values are equal,  $3\alpha + \beta = 7\alpha$ , so  $\beta = 4\alpha$  is the best choice (see Figure 3.3 for illustration). With that, the optimal single witness for the GHZ state

$$\mathcal{W}^{\text{GHZ}} = \frac{1}{11} \left( T_{0033}^2 + T_{0303}^2 + T_{0330}^2 + T_{3003}^2 + T_{3030}^2 + T_{3300}^2 + T_{3333}^2 + 4T_{1221}^2 \right) \leq_{\text{SEP}} \frac{7}{11} \quad (3.24)$$

is established.

### 3.1.5. Witnesses for other prominent states

The scheme introduced above can be used to derive witnesses for other prominent quantum states, including the cluster, Dicke, singlet and W state.

**Cluster state** Table 3.2 shows the list of all non-trivial correlations for the cluster state

$$|\mathcal{C}_4\rangle \propto (|HHHH\rangle + |HHVV\rangle - |VVHH\rangle + |VVVV\rangle) . \quad (3.25)$$

Thereof, the bases  $zzxx$  and  $xxzz$  were chosen for measurements. 6 non-zero correlations can be deduced from them, and there are corresponding cut-anticommuting operators for every cut, so this choice is viable for the construction of non-linear witnesses. Let us again take a look at cut  $AB|CD$  as an example. For this cut,  $\sigma_{0311}$  and  $\sigma_{3011}$  cut-anticommute with  $\sigma_{1130}$  and  $\sigma_{1103}$ , so, for a separable state, only the first *or* the last two operators can be large. This results in the normalised criterion

$$\mathcal{W}_{AB|CD}^{\mathcal{C}_4} = \frac{1}{2} \left( \frac{1}{2} \left( T_{0311}^2 + T_{3011}^2 \right) + \frac{1}{2} \left( T_{1130}^2 + T_{1103}^2 \right) \right) \leq_{\text{SEP}_{AB|CD}} \frac{1}{2} \quad (3.26)$$

with  $\mathcal{W}_{AB|CD}^{\mathcal{C}_4} = 1$  for the ideal cluster state. Criteria for 1-vs-3 separability look very similar, but for the bipartitions  $\mathcal{B} = \{AC|BD, AD|BC\}$ , there is a difference. In these cases,

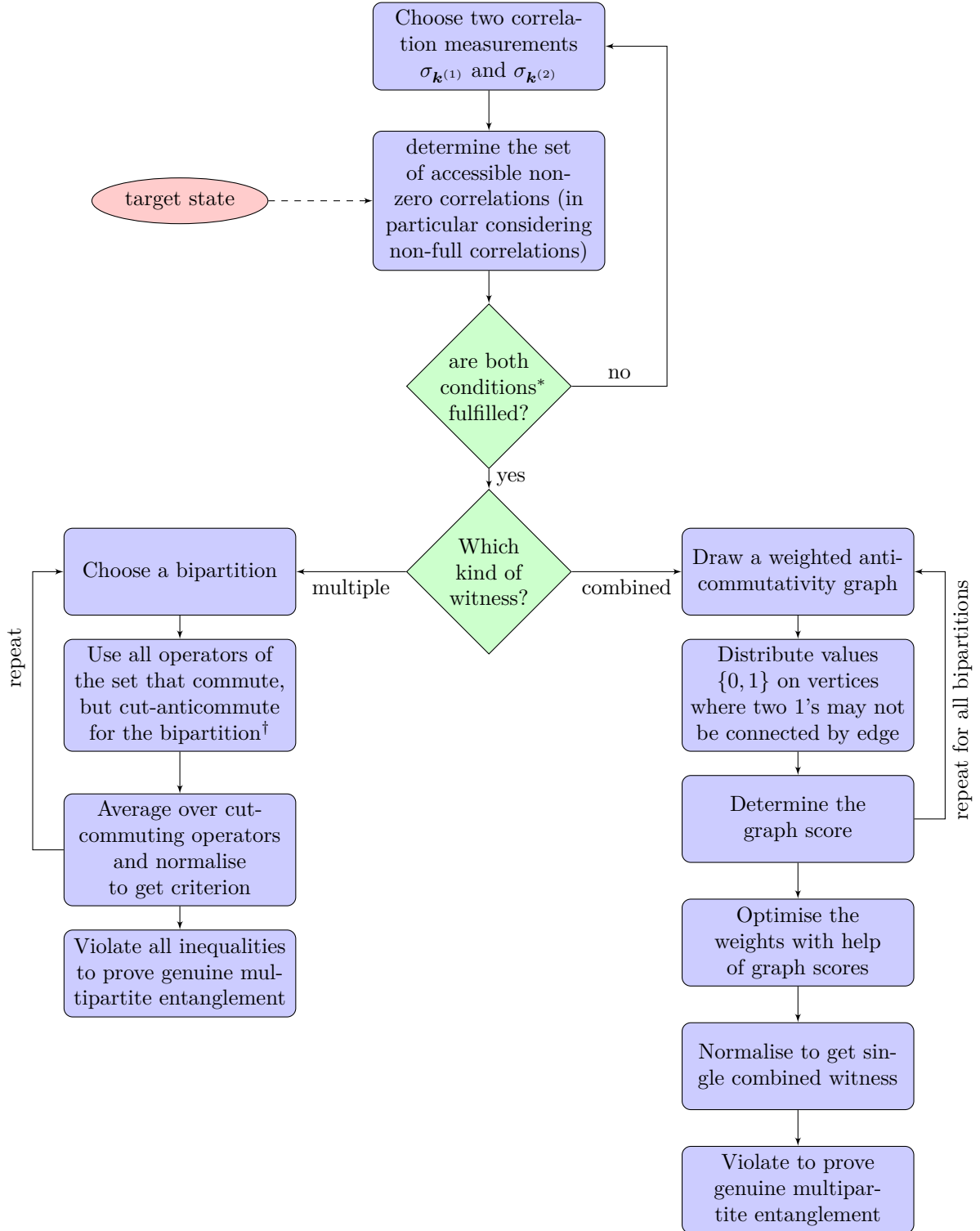


**Figure 3.2.: Flowchart for witness construction.** This scheme gives an overview of the process to construct either separate criteria for every bipartition or the combined witness to prove genuine multipartite entanglement. For details, please refer to the text. (\*) the conditions mentioned here are (1) the set has to contain, for every bipartition, operators that commute, but cut-anticommute and (2) the respective squared correlations have to be large. (†) when there are operators with different squared expectation values, choose those with the largest for best noise robustness.

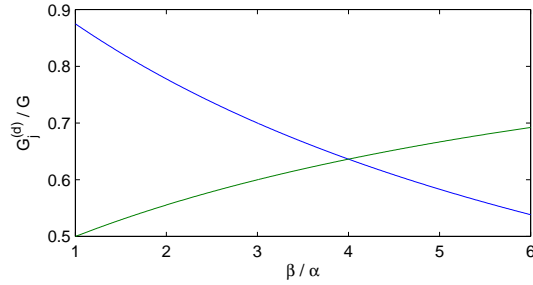


**Figure 3.3.: Illustration of optimisation of weights.** The best noise robustness is achieved when the maximal graph score achievable by separable states (from the cut-anticommutativity graphs) is small in comparison to the score obtainable by an entangled state (from the anticommutativity graph). Here, the two possibilities to obtain high scores with separable states are shown. The **blue line** shows the ratio  $(3\alpha + \beta)/(7\alpha + \beta)$ , the **green line** shows  $7\alpha/(7\alpha + \beta)$ . For each line, there is at least one separable state achieving that value. We are therefore looking for the minimum of the highest line, which is obtained at the intersection.

all operators cut-anticommute with two other operators, making up a closed circle. Thus, only 3 out of 6 correlations can be large for a state separable to these partitions, leading to

$$\mathcal{W}_{\mathcal{B}}^{\mathcal{C}_4} = \frac{1}{6} \left( T_{0033}^2 + T_{0311}^2 + T_{3011}^2 + T_{1103}^2 + T_{1130}^2 + T_{3300}^2 \right) \leq_{\text{SEP}} \frac{1}{2} \quad (3.27)$$

For the cluster state, a single witness

$$\mathcal{W}^{\mathcal{C}_4} = \frac{1}{6} \left( T_{0033}^2 + T_{0311}^2 + T_{3011}^2 + T_{1103}^2 + T_{1130}^2 + T_{3300}^2 \right) \leq_{\text{BISEP}} \frac{2}{3} \quad (3.28)$$

can also be derived by combining the criteria for all possible cuts, in the same way as for the GHZ-witness. The weights of all correlations are equal because the corresponding operators behave symmetrically for the different cuts. Note that the combined criterion looks just like the one for  $AC|BD$  and  $AD|BC$ , but has a higher threshold.

**Dicke state** The four-qubit Dicke state with two excitations,

$$\left| D_4^{(2)} \right\rangle \propto |HHVV\rangle + |HVHV\rangle + |HVVH\rangle + |VHHV\rangle + |VHVH\rangle + |VVHH\rangle, \quad (3.29)$$

has only three correlations equal to  $\pm 1$ , namely  $T_{1111}$ ,  $T_{2222}$  and  $T_{3333}$ . Fortunately,  $\sigma_{1111}$  allows to deduce also non-full correlations ( $T_{0011}$  and permutations) with values  $\pm 2/3$ , such

**Table 3.2.: The non-vanishing correlations of the cluster state.** The correlations in **blue** can be inferred from the expectation values of  $\sigma_{1133}$ , those in **red** from  $\sigma_{3311}$  [51].

$T_{0000}$	1	$T_{0033}$	1	$T_{0311}$	1	$T_{0322}$	-1
$T_{1103}$	-1	$T_{1130}$	-1	$T_{1212}$	-1	$T_{1221}$	-1
$T_{2112}$	-1	$T_{2121}$	-1	$T_{2203}$	1	$T_{2230}$	1
$T_{3011}$	1	$T_{3022}$	-1	$T_{3300}$	1	$T_{3333}$	1

that entanglement witnesses using measurements in the bases  $xxxx$  and  $yyyy$  are possible. 1-vs-3 separability  $\{1 : 3\}$  (e.g.  $A|BCD$ ) can be ruled out by violation of

$$\mathcal{W}_{\{1:3\}}^D = \frac{1}{2} \left( T_{1111}^2 + T_{2222}^2 \right) \leq_{\text{SEP}_{\{1:3\}}} \frac{1}{2} \quad (3.30)$$

with  $\mathcal{W}_{\{1:3\}}^D = 1$  for the Dicke state. Please note that averaging over additional correlations as done for the GHZ and cluster state would lead to a weaker criterion, since these additional correlations are smaller ( $\pm 2/3$ ) here. 2-vs-2 separability is checked by

$$\mathcal{W}_{AB|CD}^D = \frac{1}{2} \left( \frac{1}{4} \left( T_{1010}^2 + T_{1001}^2 + T_{0110}^2 + T_{0101}^2 \right) + T_{2222}^2 \right) \leq_{\text{SEP}_{AB|CD}} \frac{1}{2} \quad (3.31)$$

for the cut  $AB|CD$ . Note that even the ideal Dicke state obtains only  $\mathcal{W}_{AB|CD}^D = 1/8(4 \cdot 4/9 + 4) = 13/18 \approx 0.72$  in this case! Separability along the two remaining cuts can be ruled out by permuting the indices in the above equation. Although a combined criterion would be theoretically possible for the Dicke state,

$$\mathcal{W}^D = \frac{1}{11} \left( T_{1111}^2 + T_{0011}^2 + T_{0101}^2 + T_{0110}^2 + T_{1010}^2 + T_{1001}^2 + T_{1100}^2 + 4T_{2222}^2 \right) \leq_{\text{BISEP}} \frac{7}{11}, \quad (3.32)$$

its noise robustness is quite low because of the low absolute values of the correlations (the ideal Dicke state only obtains  $\mathcal{W}^D = 23/33 \approx 0.697$ , slightly more than the required  $7/11 \approx 0.636$ ). It would therefore be very difficult to experimentally violate the inequality.

**Singlet state** The set of correlations determinable by measuring in the  $xxxx$  and  $yyyy$  basis for the Dicke state are similar for the four qubit singlet state

$$|\Psi_4\rangle \propto |HHVV\rangle + |VVHH\rangle - \frac{1}{2} (|HVHV\rangle + |HVVH\rangle + |VHHV\rangle + |VHVV\rangle). \quad (3.33)$$

Therefore, the criteria  $\mathcal{W}_{\{1:3\}}^\Psi = \mathcal{W}_{\{1:3\}}^D$  and  $\mathcal{W}_{AB|CD}^\Psi = \mathcal{W}_{AB|CD}^D$  can still be used, while the remaining two

$$\mathcal{W}_{AC|BD}^\Psi = \frac{1}{2} \left( \frac{1}{2} \left( T_{1001}^2 + T_{0110}^2 \right) + T_{2222}^2 \right) \leq_{\text{SEP}_{AC|BD}} \frac{1}{2} \quad (3.34)$$

$$\mathcal{W}_{AD|BC}^\Psi = \frac{1}{2} \left( \frac{1}{2} \left( T_{1010}^2 + T_{0101}^2 \right) + T_{2222}^2 \right) \leq_{\text{SEP}_{AD|BC}} \frac{1}{2} \quad (3.35)$$

have to be slightly modified (correlations  $T_{0011}$  and  $T_{1100}$  are left out because they only reach a value of  $1/3$  for the singlet state). Also because of these low absolute values for the correlations, it is not possible to design a single witness for all cuts still detecting the singlet state. With the method introduced above, the witness

$$\mathcal{W}_1^\Psi = \frac{1}{11} \left( T_{1111}^2 + T_{0011}^2 + T_{0101}^2 + T_{0110}^2 + T_{1010}^2 + T_{1001}^2 + T_{1100}^2 + 4T_{2222}^2 \right) \leq_{\text{BISEP}} \frac{7}{11} \quad (3.36)$$

would be obtained (if we take the low correlations into account again), but its value for the singlet state is exactly  $7/11$ , making the inequality impossible to violate with the ideal singlet state. Leaving out the two low correlations makes matters worse, as

$$\mathcal{W}_2^\Psi = \frac{1}{7} \left( T_{1111}^2 + T_{0101}^2 + T_{0110}^2 + T_{1010}^2 + T_{1001}^2 + 2T_{2222}^2 \right) \leq_{\text{BISEP}} \frac{5}{7} \quad (3.37)$$

obtains only  $43/63$  for the singlet state, falling short by  $2/63$ .

**W state** For the fourpartite W state,

$$|W_4\rangle \propto |HHHV\rangle + |HHVH\rangle + |HVHH\rangle + |VHHH\rangle, \quad (3.38)$$

the witnesses have even lower noise robustness, but still, it is possible to design them using only two measurement settings. Except for  $T_{3333} = -1$ , correlations are at most  $\pm 1/2$ . Using the bases  $xxxx$  and  $zzzz$ , the criteria

$$\mathcal{W}_{A|BCD}^W = \frac{1}{2} \left( \frac{1}{3} \left( T_{1001}^2 + T_{1010}^2 + T_{1100}^2 \right) + T_{3333}^2 \right) \leq_{\text{SEP}_{A|BCD}} \frac{1}{2} \quad (3.39)$$

and

$$\mathcal{W}_{AB|CD}^W = \frac{1}{2} \left( \frac{1}{4} \left( T_{0101}^2 + T_{0110}^2 + T_{1001}^2 + T_{1010}^2 \right) + T_{3333}^2 \right) \leq_{\text{SEP}_{AB|CD}} \frac{1}{2} \quad (3.40)$$

follow, while the other criteria for 1-vs-3 separations can be obtained by permuting indices in Eq. (3.39) and separability along  $AC|BD$  and  $AD|BC$  can be ruled out with permutations of Eq. (3.40). Again, because of the low correlation values, it is not possible to design a combined witness that can prove multipartite entanglement for the W state.

### 3.1.6. Extension to more qubits

The combined two-measurement witnesses for GHZ and cluster state can also be formulated for the general case of  $N$  qubits. For the GHZ state, it is based on the correlations  $T_{3333\dots 3}$ ,  $T_{0033\dots 3}$ ,  $T_{0303\dots 3}$ ,  $\dots$ ,  $T_{33\dots 300}$ , and, e.g.,  $T_{2211\dots 1}$  and is optimal when  $T_{2211\dots 1}$  has  $2^{N-2}$  times the weight of the other correlations. Genuine multipartite entanglement can be detected by violating

$$\mathcal{W}^{\text{GHZ}_N} \leq_{\text{BISEP}} \frac{2^{N-1} - 1}{2^{N-1} + 2^{N-2} - 1} \xrightarrow{N \rightarrow \infty} \frac{2}{3}, \quad (3.41)$$

with the limiting threshold of  $2/3$  for large systems.

For the  $N$ -qubit cluster state, measurements of  $\sigma_{1313\dots 13}$  and  $\sigma_{3131\dots 31}$  are sufficient. As in the four-qubit case, weights are equal for optimal noise robustness, genuine multipartite entanglement can be identified by violation of

$$\mathcal{W}^{\text{C}_N} \leq_{\text{BISEP}} \frac{2^{N/2-1} + 2^{N/2} - 2}{2(2^{N/2} - 1)} \xrightarrow{N \rightarrow \infty} \frac{3}{4}, \quad (3.42)$$

with the threshold converging to  $3/4$ . For details, refer to Ref. [51].

## 3.2. Experimental implementation

In this section, the focus lies on the experimental demonstration of the usability of the derived entanglement witnesses for a family of superpositions between four qubit GHZ and cluster states. First, the target states are prepared, then, to prove full experimental control, complete state tomographies of the states are performed. These also include the measurements necessary to infer the values of the nonlinear entanglement witnesses.

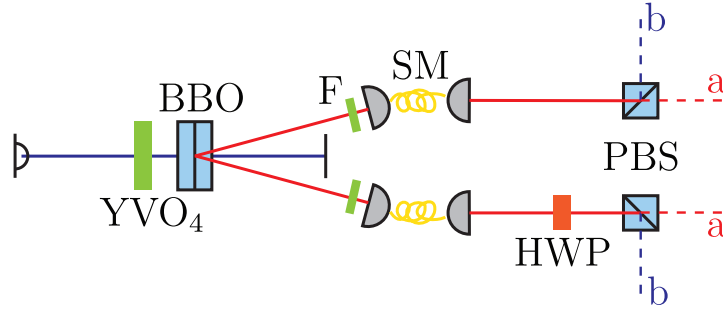


**Figure 3.4.: Optical setup for state preparation.** Pumped by a continuous wave laser diode, two crossed type I cut BBO crystals create entangled photon pairs by spontaneous parametric down conversion. The emitted pairs are spectrally filtered by interference filters (F) and coupled into single mode fibers (SM) for spatial filtering. A half-wave plate (HWP) in one output mode allows to rotate the prepared states before the Hilbert space is enlarged by coupling to a spatial degree of freedom with polarising beam splitters (PBS).

### 3.2.1. State preparation

For a high state fidelity, high count rate, and the ability to superpose GHZ and cluster states, two qubits are encoded on the polarisation degree of freedom and the other two on the path degree of freedom. This is achieved by using polarising beam splitters to couple the spatial degree of freedom of both photons to their polarisations.

#### The photon source

The two polarisation entangled photons are obtained from a spontaneous parametric down conversion (SPDC) source, as explained in Section 2.6.1. In our case, we use a pair of crossed type I cut  $\beta$ -Barium-Borate (BBO) crystals. The crystals are pumped at a central wavelength of 402 nm with approximately 60 mW power and  $45^\circ$  linearly polarised light created by a continuous wave laser diode. An additional YVO<sub>4</sub> in front of the BBOs enables to set a phase  $\varphi$ , resulting in the state

$$|\psi_{\text{SPDC}}(\varphi)\rangle = \frac{1}{\sqrt{2}} \left( |HH\rangle + e^{i\varphi} |VV\rangle \right). \quad (3.43)$$

The emitted photons are spectrally filtered by interference filters with a bandwidth of 5 nm, while spatial filtering is achieved by coupling them into single mode fibers. As seen in Figure 3.4, an HWP at angle  $\theta$ , put in one of the output modes, rotates the polarisation of one of the photons to any linear polarisation. Hence, states of the form

$$\begin{aligned} |\psi_{\text{source}}(\varphi, \theta)\rangle = & \frac{1}{\sqrt{2}} \left( |H\rangle (\cos(2\theta) |H\rangle + \sin(2\theta) |V\rangle) \right. \\ & \left. + e^{i\varphi} |V\rangle (\sin(2\theta) |H\rangle - \cos(2\theta) |V\rangle) \right) \end{aligned} \quad (3.44)$$

can be prepared.

### Enlarging the Hilbert space

Polarising beam splitters allow to couple to the path degree of freedom. Consequently, the Hilbert space is enlarged to contain the intended four qubit states. More precisely, photons in the incoming mode  $A$  (see Figure 2.6) are transformed as

$$|H\rangle \rightarrow |Ha\rangle \quad (3.45)$$

$$|V\rangle \rightarrow |Vb\rangle \quad (3.46)$$

such that the family

$$\begin{aligned} |\psi_{\text{family}}(\varphi, \theta)\rangle = & \frac{1}{\sqrt{2}} \left( \cos(2\theta) |HaHa\rangle + \sin(2\theta) |HaVb\rangle \right. \\ & \left. + e^{i\varphi} \sin(2\theta) |VbHa\rangle - e^{i\varphi} \cos(2\theta) |VbVb\rangle \right) \end{aligned} \quad (3.47)$$

is obtained.

By setting the YVO<sub>4</sub> crystal in the source according to  $\varphi = \pi$ , the GHZ states

$$|\psi_{\text{family}}(\pi, 0)\rangle = |\psi_{\text{GHZ}}\rangle = \frac{1}{\sqrt{2}} (|HaHa\rangle + |VbVb\rangle) \quad (3.48)$$

$$\left| \psi_{\text{family}} \left( \pi, \frac{\pi}{4} \right) \right\rangle = |\psi_{\text{GHZ}'}\rangle = \frac{1}{\sqrt{2}} (|HaVb\rangle + |VbHa\rangle) \quad (3.49)$$

and the cluster state

$$\left| \psi_{\text{family}} \left( \pi, \frac{\pi}{8} \right) \right\rangle = |\psi_{\text{C}}\rangle = \frac{1}{2} (|HaHa\rangle + |HaVb\rangle - |VbHa\rangle + |VbVb\rangle) \quad (3.50)$$

can be prepared just by rotating the HWP to  $\theta = 0, \pi/4$  and  $\pi/8$ , respectively. Obviously, superpositions of GHZ and cluster states can be prepared by intermediate values of  $\theta$ .

### 3.2.2. State analysis

In order to characterise the prepared states, QST is performed, proving full control of the experimental apparatus. Therefore, the different spatial modes have to be overlapped again such that their phase difference can be determined – an interferometric setup is needed, which is followed by polarisation analyses and coincidence detection.

#### Interferometers

It is crucial to keep the interferometers stable during the experiment. A Sagnac configuration as shown in Figure 3.5 allows for high phase stability without the need for active stabilisation schemes.

The wave plates in the interferometer are necessary for state tomography and, counter-intuitively, measure the polarisation degree of freedom of the photons. The required angle settings will be discussed later in Section 3.2.2. The two YVO<sub>4</sub> crystals with their optical axes crossed are used to compensate any unwanted polarisation dependent phase shift. Although all optical components were mounted carefully to avoid birefringence due to mechanical stress,

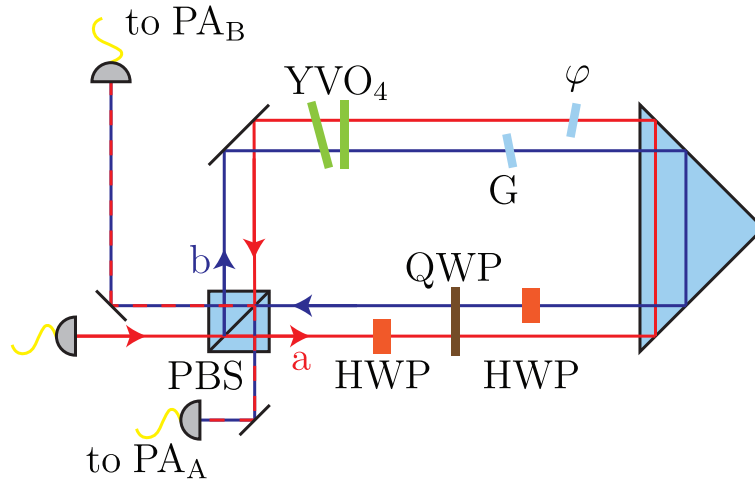


**Figure 3.5.: One of the interferometers.** To determine the phase between the two spatial modes, an interferometric setup is needed. To avoid active stabilisation schemes, a self stabilising Sagnac loop is used. Please note that the polarising beam splitter (PBS) is first used to enlarge the Hilbert space and then again to overlap the modes; it is part of the state preparation as well as the state analysis.  $\text{YVO}_4$  crystals are used to compensate polarisation dependent phase shifts (e.g. Goos-Hänchen effect), and glass plates  $G$  and  $\varphi$  shift the phases between the two interferometer modes  $a$  and  $b$ . A combination of half- (HWP) and quarter-wave plates (QWP) sets the measurement basis for the polarisation degree of freedom. After the modes are overlapped again, they are coupled into single mode fibers leading to polarisation analysis setups PA (see Figure 2.7)

the internal reflection at the prism still evokes such a phase shift (Goos-Hänchen effect). Finally, the phase between the two interferometer modes can be set by the glass plates. One of them is motorized, enabling easy correction of thermal length fluctuations and varying wave-plate thicknesses. The other glass plate of the same thickness balances the interferometer. Together, they have to be aligned such that relative phases (arising e.g. from reflections, imperfections of the mirrors and wave plates) between the modes of the interferometer are compensated. Details on how to set up the interferometer and how to determine the angle for the glass plate can be found in Appendix A.

### Polarisation analysis and detection

After overlapping the interferometer modes again at the polarising beam splitter, the polarisation of each output photon has to be analysed. This can be done by a setup as explained in Section 2.7.1. The main advantage of using a polarising beam splitter instead of a polariser is that both outputs can be detected simultaneously with two different detectors, which leads to higher count rates. In our experiment, we use fiber coupled single photon counters from Perkin Elmer (SPCM), connected to a coincidence logic with a window of 10 ns. Since the detectors are not perfect, they show different detection efficiencies. This effect can be compensated by measuring and calculating efficiencies, which are then used to correct later measurement results accordingly. In our case, we also account for different coupling efficiencies for each angle setting of the components in the interferometers, resulting in 12 efficiencies

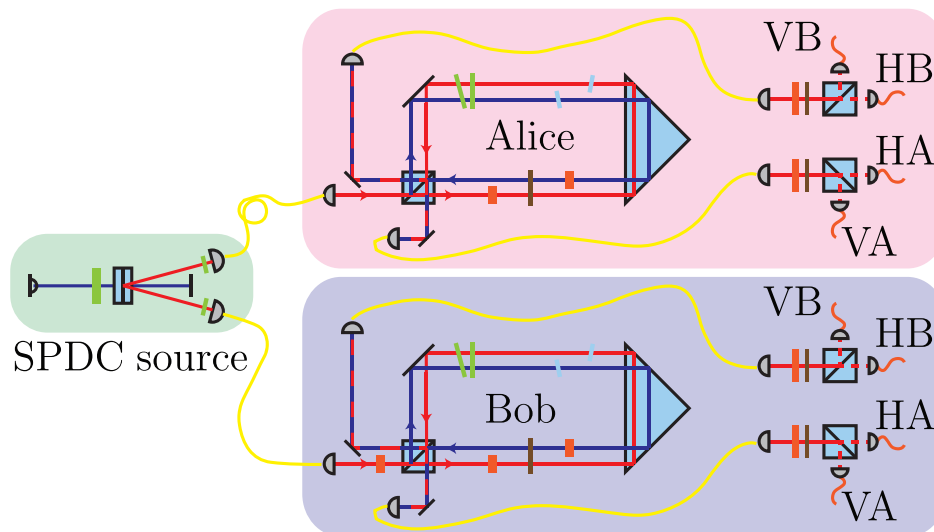


**Figure 3.6.: Complete experimental setup.** The complete setup consists of the photon source, two interferometers Alice and Bob, and four polarisation analyses, in total. The detectors in each Alice and Bob are labeled “HA”, “VA”, “HB” and “VB”, respectively, after the output modes “A” and “B” of the interferometer and the “H” and “V” output of the analysis PBS.

for each Alice and Bob. Further details on how these numbers are obtained can be found in Appendix A.2.

Altogether, the setup consists of the SPDC source with the additional waveplate, two Sagnac interferometers, 4 polarisation analyses and 8 detectors detecting twofold coincidences. The complete setup is shown in Figure 3.6.

### Measurement bases and settings

We choose to measure in the eigenbases of all combinations of local Pauli bases because this yields the required correlations for the two-measurement witnesses as described in the theory part (Section 3.1.1). For simplicity, let us first look at a single interferometer with its succeeding polarisation analyses. To measure, for example, in the  $xx$  basis in this system means we have to measure projections onto the eigenstates of  $\sigma_{11}$ , namely  $|P(a+b)\rangle$ ,  $|P(a-b)\rangle$ ,  $|M(a+b)\rangle$  and  $|M(a-b)\rangle$ , where a shorthand notation

$$\begin{aligned} |P(a+b)\rangle &\equiv \frac{1}{\sqrt{2}} (|H\rangle + |V\rangle) \otimes \frac{1}{\sqrt{2}} (|a\rangle + |b\rangle) \\ &= \frac{1}{2} (|Ha\rangle + |Va\rangle + |Hb\rangle + |Vb\rangle) \end{aligned} \quad (3.51)$$

is used. If we want to measure  $|P(a+b)\rangle$  with a click in the detector “HA”, the waveplates in the interferometer have to be set such that one has constructive interference at output “A” and destructive interference at output B. This means that in path  $a$  of the interferometer, the  $|P\rangle$  has to be rotated to  $e^{i\varphi_1} |H\rangle$  and in path  $b$  it has to be rotated to  $e^{i\varphi_2} |V\rangle$  (with arbitrary phases  $\varphi$ ). With both HWPs at  $\pi/8$  and the QWP at 0 (please note that angles are measured as seen from beam  $a$ ; therefore the angles for calculating beam  $b$  have to be

inverted), it is

$$\text{mode } a : \quad U_{\text{QWP}}(0) U_{\text{HWP}}\left(\frac{\pi}{8}\right) |P\rangle = |H\rangle \quad (3.52)$$

$$\text{mode } b : \quad U_{\text{QWP}}(0) U_{\text{HWP}}\left(-\frac{\pi}{8}\right) |P\rangle = i|V\rangle \quad (3.53)$$

so that the state  $|H\rangle + i|V\rangle = |R\rangle$  is in output  $A$  and nothing in  $B$ . Then, the QWP in the analysis  $\text{PA}_A$  has to be set to  $\pi/4$ ,

$$U_{\text{QWP}}\left(\frac{\pi}{4}\right) U_{\text{HWP}}(0) |R\rangle = e^{i\varphi} |H\rangle \quad (3.54)$$

such that the right polarised photon will be detected in the  $HA$ -detector (with a phase  $\varphi$  of no importance). Conveniently, the other eigenstates  $|P(a-b)\rangle$ ,  $|M(a+b)\rangle$  and  $|M(a-b)\rangle$  can be measured simultaneously in the detectors  $VA$ ,  $HB$  and  $VB$ , respectively, with the QWP in analysis  $\text{PA}_B$  set to  $-\pi/4$ . For example, the state  $|M(a-b)\rangle$  transforms

$$\text{mode } a : \quad U_{\text{QWP}}(0) U_{\text{HWP}}\left(\frac{\pi}{8}\right) |M\rangle = -i|V\rangle \quad (3.55)$$

$$\text{mode } b : \quad U_{\text{QWP}}(0) U_{\text{HWP}}\left(-\frac{\pi}{8}\right) |M\rangle = |H\rangle \quad (3.56)$$

to  $-|H\rangle - i|V\rangle = -|R\rangle$  (take into account the sign of path  $b!$ ) in output  $B$  of the beam splitter. This state will result in a click in detector  $VB$  if the corresponding QWP is set to  $-\pi/4$ .

Angles for the other bases can be derived analogously and are listed in Table 3.3.

For measuring the whole state, all combinations of the 9 measurement settings for both interferometers have to be considered, resulting in 81 different angle settings. Only twofold coincidences (each between one detector on Alice's side and one on Bob's side) are considered now, resulting in 16 projectors measured simultaneously in each setting. Therefore, in total  $81 \times 16 = 1296$  different projection measurements are performed.

### 3.2.3. Experimental results

For the actual experimental demonstration of the applicability of non-linear witnesses (after making sure all phases are compensated (Appendix A.1) and measuring the efficiencies (Appendix A.2)), 13 states of the family Eq. (3.47) were prepared by rotating the half-wave plate from  $\theta = 0$  to  $\pi/4$  in 13 equal steps. With a coincidence rate of approximately  $100 \text{ s}^{-1}$  and a measurement time of 40 s per basis setting (resulting in 3700 – 4400 counts per setting), it took about 12 h to perform QST for the whole family. The same data are used to obtain the values of all derived witnesses. In addition, with data from experiments described in Ref. [53, 54], the criteria for the Dicke  $|D_4^{(2)}\rangle$  and singlet state  $|\Psi_4\rangle$  are tested.

**Table 3.3.: Angle settings for different bases.** The angles of the waveplates of the interferometer (HWP<sub>IF,1</sub>, QWP<sub>IF</sub>, HWP<sub>IF,2</sub>) and of the two polarisation analyses (HWP<sub>A</sub>, QWP<sub>A</sub>; HWP<sub>B</sub>, QWP<sub>B</sub>) to perform the given projections. “HA”, “VA”, “HB”, “VB” denote the detectors for the transmitted (“H”) and reflected light (“V”) of the PBS of the polarisation analyses in the output modes A and B, respectively. For example, an event of the detector “HA” while measuring in the basis  $\sigma_{11}(xx)$  corresponds to a successful projection onto the state  $|P(a+b)\rangle$ . Please note that all angles are referenced with respect to mode  $a$  which means that for calculating the transformations induced for light in mode  $b$  a minus sign has to be added. Taken from [51].

Basis	Interferometer			Polarisation analyses				Projectors			
	HWP <sub>IF,1</sub>	QWP <sub>IF</sub>	HWP <sub>IF,2</sub>	HWP <sub>A</sub>	QWP <sub>A</sub>	HWP <sub>B</sub>	QWP <sub>B</sub>	HA	VA	HB	VB
$\sigma_{11}(xx)$	$\frac{\pi}{8}$	0	$\frac{\pi}{8}$	0	$\frac{\pi}{4}$	0	$-\frac{\pi}{4}$	P(a+b)	P(a-b)	M(a+b)	M(a-b)
$\sigma_{12}(xy)$	$\frac{\pi}{8}$	0	$\frac{\pi}{8}$	$-\frac{\pi}{8}$	0	$-\frac{\pi}{8}$	0	P(a+ib)	P(a-ib)	M(a+ib)	M(a-ib)
$\sigma_{13}(xz)$	$\frac{\pi}{8}$	0	$\frac{\pi}{8}$	0	0	$\frac{\pi}{4}$	0	Pa	Pb	Ma	Mb
$\sigma_{21}(yx)$	0	$\frac{\pi}{4}$	0	0	$-\frac{\pi}{4}$	0	$\frac{\pi}{4}$	R(a+b)	R(a-b)	L(a+b)	L(a-b)
$\sigma_{22}(yy)$	0	$\frac{\pi}{4}$	0	$\frac{\pi}{8}$	0	$\frac{\pi}{8}$	0	R(a+ib)	R(a-ib)	L(a+ib)	L(a-ib)
$\sigma_{23}(yz)$	0	$\frac{\pi}{4}$	0	0	0	$\frac{\pi}{4}$	0	Ra	Rb	La	Lb
$\sigma_{31}(zx)$	0	0	$\frac{\pi}{4}$	0	$\frac{\pi}{4}$	0	$-\frac{\pi}{4}$	H(a+b)	H(a-b)	V(a+b)	V(a-b)
$\sigma_{32}(zy)$	0	0	$\frac{\pi}{4}$	$-\frac{\pi}{8}$	0	$-\frac{\pi}{8}$	0	H(a+ib)	H(a-ib)	V(a+ib)	V(a-ib)
$\sigma_{33}(zz)$	0	0	$\frac{\pi}{4}$	0	0	$\frac{\pi}{4}$	0	Ha	Hb	Va	Vb

### Complete state tomography

The fidelity  $\mathcal{F}$  (see Section 2.7.4) is used as a measure for the quality of the prepared state. With  $\mathcal{F} = 0.958 \pm 0.004$  for the GHZ state and  $\mathcal{F} = 0.962 \pm 0.003$  for the cluster state, high agreement with the theoretically expected states is seen. Fidelities for the other states can be found in Table 3.4. The real parts of density matrices of GHZ, cluster and GHZ’ are depicted in Figure 3.7, while the imaginary parts are vanishingly small.

### Evaluation of nonlinear entanglement witnesses

Let us start with the evaluation of the measured correlations of the GHZ state. From measurements in the bases  $zzzz$  and  $xyyx$ , the correlations  $T_{3333} = 0.982 \pm 0.003$ ,  $T_{3300} = 0.993 \pm 0.002$ ,

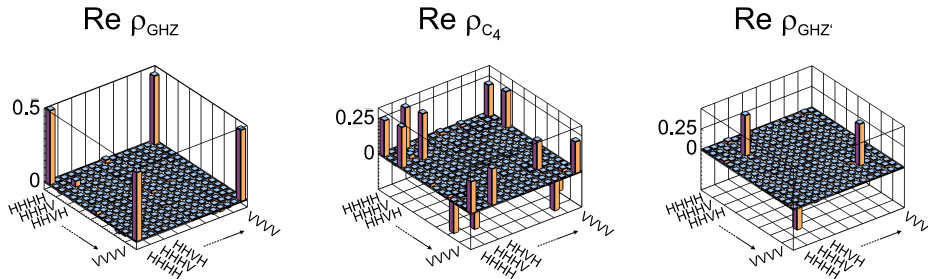


**Figure 3.7.: Experimental density matrices.** Real parts of the experimental density matrices of (a) the GHZ state ( $\theta = 0$ ,  $\phi = \pi$ ), (b) the cluster state ( $\theta = \frac{\pi}{8}$ ,  $\phi = \pi$ ), and (c) the GHZ’ state ( $\theta = \frac{\pi}{4}$ ,  $\phi = \pi$ ). From [51].

$T_{0033} = 0.988 \pm 0.002$ ,  $T_{3003} = 0.963 \pm 0.004$ ,  $T_{0330} = 0.969 \pm 0.004$ ,  $T_{3030} = 0.972 \pm 0.004$ ,  $T_{0303} = 0.960 \pm 0.005$  and  $T_{1221} = -0.925 \pm 0.006$  could be obtained. That leads to

$$\mathcal{W}_{AB|CD}^{\text{GHZ}} = 0.894 \pm 0.007 \leq \underset{AB|CD}{\text{SEP}} \frac{1}{2} \quad (3.57)$$

$$\mathcal{W}_{AC|BD}^{\text{GHZ}} = 0.906 \pm 0.006 \leq \underset{AC|BD}{\text{SEP}} \frac{1}{2} \quad (3.58)$$

$$\mathcal{W}_{AD|BC}^{\text{GHZ}} = 0.906 \pm 0.006 \leq \underset{AD|BC}{\text{SEP}} \frac{1}{2} \quad (3.59)$$

$$\mathcal{W}_{A|BCD}^{\text{GHZ}} = 0.906 \pm 0.006 \leq \underset{A|BCD}{\text{SEP}} \frac{1}{2} \quad (3.60)$$

$$\mathcal{W}_{B|ACD}^{\text{GHZ}} = 0.904 \pm 0.006 \leq \underset{B|ACD}{\text{SEP}} \frac{1}{2} \quad (3.61)$$

$$\mathcal{W}_{C|ABD}^{\text{GHZ}} = 0.906 \pm 0.006 \leq \underset{C|ABD}{\text{SEP}} \frac{1}{2} \quad (3.62)$$

$$\mathcal{W}_{D|ABC}^{\text{GHZ}} = 0.901 \pm 0.006 \leq \underset{D|ABC}{\text{SEP}} \frac{1}{2}, \quad (3.63)$$

certifying genuine multipartite entanglement with more than 56 standard deviations. In this case, also the single combined non-linear entanglement witness

$$\mathcal{W}^{\text{GHZ}} = 0.916 \pm 0.005 \leq \underset{\text{BISEP}}{\text{BISEP}} \frac{7}{11} \quad (3.64)$$

disproves separability with a significance of over 55 standard deviations.

For the cluster state, measurements in the bases  $zzxx$  and  $xxzz$  deliver the correlations  $T_{3300} = 0.987 \pm 0.002$ ,  $T_{3011} = 0.986 \pm 0.003$ ,  $T_{0311} = 0.974 \pm 0.003$ ,  $T_{1130} = -0.945 \pm 0.006$ ,  $T_{1103} = -0.934 \pm 0.006$  and  $T_{0033} = 0.989 \pm 0.002$ , allowing to infer values for the respective criteria

$$\mathcal{W}_{AB|CD}^{\mathcal{C}_4} = 0.922 \pm 0.006 \leq \underset{AB|CD}{\text{SEP}} \frac{1}{2} \quad (3.65)$$

$$\mathcal{W}_{AC|BD}^{\mathcal{C}_4} = 0.940 \pm 0.004 \leq \underset{AC|BD}{\text{SEP}} \frac{1}{2} \quad (3.66)$$

$$\mathcal{W}_{AD|BC}^{\mathcal{C}_4} = 0.940 \pm 0.004 \leq \underset{AD|BC}{\text{SEP}} \frac{1}{2} \quad (3.67)$$

$$\mathcal{W}_{A|BCD}^{\mathcal{C}_4} = 0.928 \pm 0.006 \leq \underset{A|BCD}{\text{SEP}} \frac{1}{2} \quad (3.68)$$

$$\mathcal{W}_{B|ACD}^{\mathcal{C}_4} = 0.922 \pm 0.006 \leq \underset{B|ACD}{\text{SEP}} \frac{1}{2} \quad (3.69)$$

$$\mathcal{W}_{C|ABD}^{\mathcal{C}_4} = 0.948 \pm 0.004 \leq \underset{C|ABD}{\text{SEP}} \frac{1}{2} \quad (3.70)$$

$$\mathcal{W}_{D|ABC}^{\mathcal{C}_4} = 0.943 \pm 0.004 \leq \underset{D|ABC}{\text{SEP}} \frac{1}{2}. \quad (3.71)$$

Here, genuine multipartite entanglement is proven with over 70 standard deviations. For the cluster state, the combined criterion looks exactly like the ones for cuts  $AC|BD$  and  $AD|BC$ , but with a threshold of  $2/3$  to account for all possible cuts. Therefore, with

$$\mathcal{W}^{\mathcal{C}_4} = 0.940 \pm 0.004 \leq \underset{\text{BISEP}}{\text{BISEP}} \frac{2}{3}, \quad (3.72)$$

### 3. Multipartite entanglement detection with minimal effort

biseparability is excluded with over 68 standard deviations.

All other states of the family are analysed only with respect to the two combined criteria, since the difference in sensitivity is not very large. The results are summarised in Table 3.4. All prepared states of the family can be shown to be genuinely fourpartite entangled by at least one of the criteria. While  $\mathcal{W}^{\text{GHZ}}$  proves entanglement for almost all states of the family,  $\mathcal{W}^{\mathcal{C}_4}$  is more suited for states near the cluster state. As shown in Figure 3.8, the regions where the criteria are above their respective thresholds overlap. Thus, some states can be detected to be genuinely fourpartite entangled by both witnesses.

**Table 3.4.: Characterisation of 13 members states of the family.** The states are given by Eq. (3.47) with  $\phi = \pi$ . The fidelities with the respective target states were determined from the experimental density matrices as obtained via quantum state tomography. The values for the combined entanglement criteria  $\mathcal{W}^{\text{GHZ}}$  and  $\mathcal{W}^{\mathcal{C}_4}$ , however, were inferred from two measurement settings only. For all prepared states, genuine fourpartite entanglement can be proven by at least one of the two criteria. Successful entanglement detection of the respective criterion is indicated by bold letters. Taken from [51].

Name	$\theta$	Fidelity $\mathcal{F}$	$\mathcal{W}^{\text{GHZ}} \leq_{\text{BISEP}} \frac{7}{11}$	$\mathcal{W}^{\mathcal{C}_4} \leq_{\text{BISEP}} \frac{2}{3}$	
GHZ	0	0.958 ± 0.004	<b>0.916 ± 0.005</b>	0.333 ± 0.002	
	$\frac{\pi}{48}$	0.959 ± 0.004	<b>0.894 ± 0.006</b>	0.387 ± 0.005	
	$\frac{\pi}{24}$	0.958 ± 0.004	<b>0.828 ± 0.007</b>	0.509 ± 0.007	
	$\frac{\pi}{16}$	0.965 ± 0.003	<b>0.740 ± 0.007</b>	<b>0.685 ± 0.007</b>	
	$\frac{\pi}{12}$	0.963 ± 0.003	<b>0.644 ± 0.006</b>	<b>0.835 ± 0.006</b>	
	$\frac{5\pi}{48}$	0.963 ± 0.003	0.603 ± 0.004	<b>0.918 ± 0.005</b>	
	Cluster	$\frac{\pi}{8}$	0.962 ± 0.003	0.590 ± 0.004	<b>0.940 ± 0.004</b>
		$\frac{7\pi}{48}$	0.959 ± 0.004	0.608 ± 0.006	<b>0.886 ± 0.007</b>
		$\frac{\pi}{6}$	0.959 ± 0.004	<b>0.679 ± 0.008</b>	<b>0.761 ± 0.008</b>
		$\frac{3\pi}{16}$	0.958 ± 0.003	<b>0.746 ± 0.007</b>	0.640 ± 0.008
$\frac{5\pi}{24}$		0.960 ± 0.004	<b>0.820 ± 0.007</b>	0.497 ± 0.007	
$\frac{11\pi}{48}$		0.963 ± 0.004	<b>0.890 ± 0.006</b>	0.375 ± 0.004	
GHZ'	$\frac{\pi}{4}$	0.967 ± 0.004	<b>0.927 ± 0.005</b>	0.330 ± 0.002	

With the experimental data from [53], all the witnesses for the Dicke state

$$\mathcal{W}_{\{1:3\}}^D = 0.819 \pm 0.013 \leq_{\text{SEP}_{\{1:3\}}} \frac{1}{2} \quad (3.73)$$

$$\mathcal{W}_{AB|CD}^D = 0.627 \pm 0.013 \leq_{\text{SEP}_{AB|CD}} \frac{1}{2} \quad (3.74)$$

$$\mathcal{W}_{AC|BD}^D = 0.620 \pm 0.013 \leq_{\text{SEP}_{AC|BD}} \frac{1}{2} \quad (3.75)$$

$$\mathcal{W}_{AD|BC}^D = 0.625 \pm 0.013 \leq_{\text{SEP}_{AD|BC}} \frac{1}{2}, \quad (3.76)$$

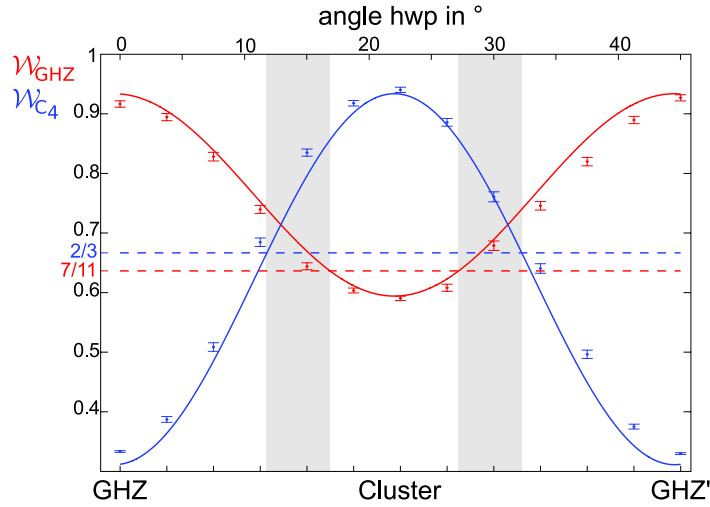


**Figure 3.8.: Performance of combined entanglement witnesses.** The entanglement criterion for the GHZ state enables to detect most states of the family to be genuinely fourpartite entangled (red) whereas the criterion for the cluster state detects states around  $\theta = 22.5^\circ$  to be genuinely fourpartite entangled (blue). States of the grey shaded areas can be detected to be genuinely fourpartite entangled by means of both criteria. The solid lines are obtained by a single fit with a phase  $\theta$  and fidelity  $\mathcal{F}$  as parameters. Taken from [51].

are violated with over 9 standard deviations. Because of the low absolute value of the non-full correlations, the combined criterion

$$\mathcal{W}^D = 0.600 \pm 0.012 \leq_{\text{BISEP}} \frac{7}{11} \quad (3.77)$$

fails to prove entanglement for the obtained data.

Experimental data of the singlet state  $|\Psi_4\rangle$  [54] lead to

$$\mathcal{W}_{\{1:3\}}^\Psi = 0.804 \pm 0.019 \leq_{\text{SEP}_{\{1:3\}}} \frac{1}{2} \quad (3.78)$$

$$\mathcal{W}_{AB|CD}^\Psi = 0.608 \pm 0.017 \leq_{\text{SEP}_{AB|CD}} \frac{1}{2} \quad (3.79)$$

$$\mathcal{W}_{AC|BD}^\Psi = 0.594 \pm 0.021 \leq_{\text{SEP}_{AC|BD}} \frac{1}{2} \quad (3.80)$$

$$\mathcal{W}_{AD|BC}^\Psi = 0.622 \pm 0.021 \leq_{\text{SEP}_{AD|BC}} \frac{1}{2} \quad (3.81)$$

and prove fourpartite entanglement by more than 4 standard deviations.

### 3.3. Conclusion

The introduced novel scheme to systematically construct non-linear entanglement witnesses based on data obtained in only two measurement settings proved to be successful for prominent states, theoretically as well as experimentally. Such a minimal multipartite entanglement detection may become a handy diagnostic tool, because it is fast and simple. It is also applicable for larger systems, as it is based on the simple principle of entanglement complementarity.

### *3. Multipartite entanglement detection with minimal effort*

---

For isolated cases like the GHZ or the cluster state there are other minimal methods to certify entanglement [55], but up to date there was no general constructive scheme applicable to such a wide range of states.

An interesting open question is how the problem of low noise robustness for low absolute correlation values of some states can be tackled. Further research could e.g. reveal the implications of relaxing the minimality condition, namely allowing three or more measurement settings to contribute.

## 4. Numerical investigation of Heisenberg scaling in quantum state tomography

In order to fully define the properties of a given quantum system, it is inevitable to perform a full quantum state tomography (QST). This is a demanding task, since  $4^n - 1$  real parameters have to be determined by measuring identically prepared quantum states, where  $n$  denotes the number of qubits. Since state preparation and measurement can take a long time in some systems, it is crucial to find methods that provide good scaling in terms of state fidelity with the number of performed measurements  $N_m$ . For random states, the infidelity scales with  $1/\sqrt{N_m}$  (normal scaling) while the limit of  $1/N_m$  (*Heisenberg scaling*) can be obtained for special cases. It was seen before that, in case of maximum likelihood estimation (MLE, Section 2.7.3), the scaling of fidelity with the number of counts per basis is significantly better and can reach the Heisenberg limit if one of the measurement axes is aligned with the target state [39]. This was also used for adaptive tomography of single qubit systems [56].

In this chapter, Monte-Carlo simulations are used to numerically investigate the scaling of tomographic state reconstruction fidelity with respect to the number of detections. Both linear inversion (LIN, Section 2.7.2) and MLE are examined, since the process of LIN is very easy to understand and sometimes preferred over non-linear methods such as MLE. On the other hand, MLE is a popular method to obtain physical density matrices from the sometimes unphysical linear results. The focus lies on single qubit states since even for this simple quantum mechanical system the convergence behaviour is not completely understood and most basic concepts established there can be generalised to more complex systems. An intuitive understanding of the processes, effects, and outcomes of quantum state tomography is developed and extended to multi-qubit systems.

### 4.1. Simulation algorithm

Every simulation starts by selecting a target state  $\rho_t$ . This is the state that is used to obtain the simulated measurement data, the state that could be prepared in an actual experiment. Then, for different numbers of counts per setting  $N$ , the measurement outcomes are determined statistically. From these data, the linearly reconstructed state  $\rho_{\text{LIN}}$  and the maximum likelihood estimate  $\rho_{\text{MLE}}$  are obtained. These states, as well as the fidelity to the target state are saved for later analysis. The whole process then has to be repeated sufficiently often to obtain a suitable sample size. Here, mostly  $M = 300$  samples are simulated.

#### 4.1.1. Target states

Because we want to study the scaling of reconstruction fidelity for differently oriented states in relation to the measurement basis, qubits rotated from  $|H\rangle$  in direction of  $|P\rangle$  are used,

i.e.

$$|\psi_t\rangle = U |H\rangle = \begin{pmatrix} \cos \theta/2 & e^{-i\varphi} \sin \theta/2 \\ e^{i\varphi} \sin \theta/2 & -\cos \theta/2 \end{pmatrix} \begin{pmatrix} 1 \\ 0 \end{pmatrix} \quad (4.1)$$

with  $\varphi = 0$  and  $\theta \in [0, \frac{\pi}{4}]$ . In case of two qubit target states, the tensor product of unity with the rotation matrix is applied to either a product or a maximally entangled two qubit state,

$$|\psi_t^{(\text{sep})}\rangle = \mathbb{1}^{(2)} \otimes U |HH\rangle . \quad (4.2)$$

$$|\psi_t^{(\text{ent})}\rangle = \mathbb{1}^{(2)} \otimes U |\phi_-\rangle \quad (4.3)$$

Additionally, white noise can be admixed

$$\rho_t = p |\psi_t\rangle \langle \psi_t| + (1 - p) \rho_{\text{WN}} \quad (4.4)$$

to get a mixed state. The state amplitude  $p$  is related to the fidelity between  $\rho_t$  and the corresponding pure state  $|\psi_t\rangle$

$$\mathcal{F}(\rho_t, |\psi_t\rangle) = p + \frac{1}{2^n} (1 - p) , \quad (4.5)$$

where the second term comes from the overlap of the white noise with the target state, and to the purity

$$P(\rho_t) = p^2 + \frac{1}{2^n} (1 - p^2) \quad (4.6)$$

where  $n$  is the number of qubits.

Because we use states with  $\varphi = 0$ , all the single qubit states in this chapter can be represented by a point on a two-dimensional unit circle, the projection of the Bloch sphere onto the  $T_x$ - $T_z$  plane, see Figure 4.1.  $\theta$  corresponds to the angular coordinate, while the radial distance is equal to the mixing factor  $p$ .

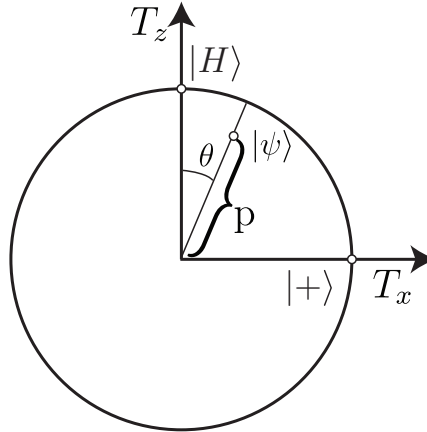


**Figure 4.1.: Target states on a projection of the Bloch sphere.** All target states used in this chapter lie in the  $T_x$ - $T_z$  plane, because  $\varphi$  is set to 0. Their position is given by the angle  $\theta$  and the radial distance  $p$ .

### 4.1.2. Simulated tomography

Starting with the target state, an overcomplete tomography scheme with  $3^n$  measurement settings  $\mathbf{s} = (s_1, \dots, s_n)$  with  $s_i \in \{x, y, z\} \equiv \{1, 2, 3\}$  as explained in Section 2.7 is simulated. Alternatively, one could consider a minimal measurement scheme as proposed by Ref. [57], with only  $2^n$  settings to consider. First, for each basis setting  $\mathbf{s}$ , the probabilities

$$p_{\mathbf{i}}^{\mathbf{s}} = \text{Re}(\text{Tr}(\rho_t \mathcal{P}_{\mathbf{i}}^{\mathbf{s}})) , \quad (4.7)$$

for all  $2^n$  measurement outcomes  $\mathbf{i} = (i_1, \dots, i_n)$  with  $i_i \in \{0, 1\}$  (with  $\mathcal{P}_{\mathbf{i}}^{\mathbf{s}}$  the projector onto the corresponding basis state) are calculated. Since the scaling behaviour is investigated in dependence to the (fixed) total number of counts  $N$  per measurement basis, a multinomial distribution

$$\mathcal{D}^{\mathbf{s}}(c_{\mathbf{i}}^{\mathbf{s}}; N, p_{\mathbf{i}}^{\mathbf{s}}) = \frac{N!}{\prod_{\mathbf{i}} c_{\mathbf{i}}^{\mathbf{s}}!} \prod_{\mathbf{i}} (p_{\mathbf{i}}^{\mathbf{s}})^{c_{\mathbf{i}}^{\mathbf{s}}} \quad (4.8)$$

(with the condition  $\sum_{\mathbf{i}} c_{\mathbf{i}}^{\mathbf{s}} = N$  on the sum of counts per basis) is used to randomise the number  $c_{\mathbf{i}}^{\mathbf{s}}$  of successful projections onto  $\mathcal{P}_{\mathbf{i}}^{\mathbf{s}}$  for the simulated tomography. After repeating this separately for every basis setting, all the frequencies  $f_{\mathbf{i}}^{\mathbf{s}} = c_{\mathbf{i}}^{\mathbf{s}}/N$  can be determined and subsequently, a reconstructed density matrix  $\rho_{rec}$  is derived via linear inversion (LIN, Section 2.7.2) and maximum likelihood (MLE, Section 2.7.3) estimation. These states can now be analysed regarding their fidelity to the theoretical target state and their purity. Please note that in case of LIN, the obtained density matrix does, in some cases, not represent a physical state, which can lead to fidelities and purities bigger than one. Nevertheless, the absolute infidelity  $|1 - \mathcal{F}|$  is still useful for a comparison of the results.

In case of a single qubit  $n = 1$ , there are only three measurement bases  $s \in \{x, y, z\}$  with two possible outcomes  $i \in \{0, 1\}$  each. The multinomial distribution simplifies to a binomial distribution

$$\mathcal{D}^s(c_0^s, c_1^s; N, p_0^s, p_1^s) = \frac{N!}{c_0^s! c_1^s!} (p_0^s)^{c_0^s} (p_1^s)^{c_1^s} = \binom{N}{c_0^s} (p_0^s)^{c_0^s} (1 - p_0^s)^{N - c_0^s} \quad (4.9)$$

because of the conditions on the sums of counts  $c_0^s + c_1^s = N$  and, equivalently, probabilities  $p_0^s + p_1^s = 1$ . This binomial distribution has a standard deviation of

$$\sigma = \sqrt{N p_0^s (1 - p_0^s)} \quad (4.10)$$

and is therefore strongly peaked for a target state with a probability of an outcome near to one, corresponding to states near one of the measurement axes. Since state reconstruction linearly uses elements of the correlation tensor  $T_s = (c_0^s - c_1^s)/N$  (see Section 2.7.2), the standard deviation of the outcomes is expected to scale with  $\sqrt{N}/N = 1/\sqrt{N}$ .

## 4.2. Results for one qubit

For a beginning, the results for one qubit found in Ref. [39, 56] are regained with the simulation procedure explained above in our frame of reference. For that purpose, the target states

$$|\psi_t\rangle = U(\theta, \varphi) |H\rangle \quad (4.11)$$

with  $\theta \in \{0, 1.5^\circ, 45^\circ\}$  and  $\varphi = 0$  are used to simulate tomographies with  $N = 100$  to  $N = 10^6$  counts per basis. To get reasonable high statistics,  $M = 300$  simulations are performed for each combination of state and counts. To analyse the performance, the mean and the standard deviation of the absolute infidelity  $|1 - \mathcal{F}|$  obtained from both LIN and MLE are calculated and displayed in a double logarithmic plot, see Figure 4.2

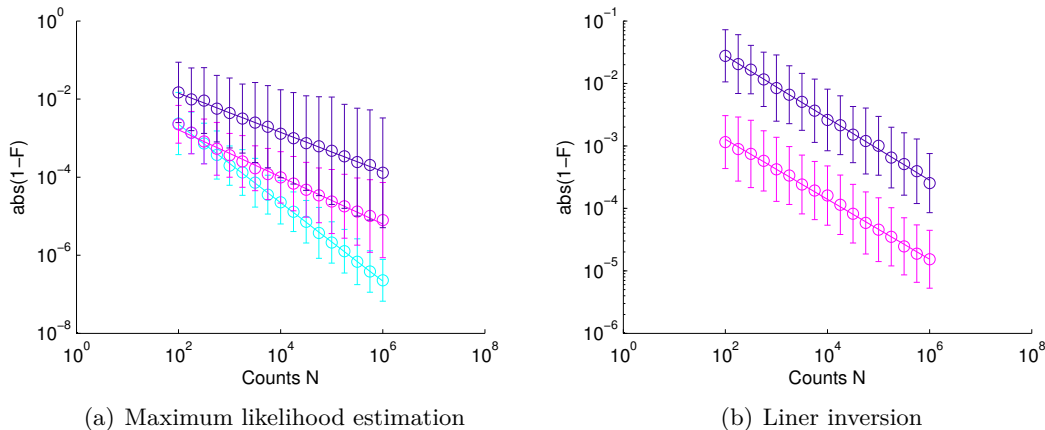


**Figure 4.2.: Scaling behaviour of infidelity.** The mean of the absolute infidelity  $|1 - \mathcal{F}|$  is depicted with respect to the number of counts per basis, for differently rotated target states - in cyan, the non-rotated state ( $\theta = 0^\circ$ ), in magenta, a slightly rotated state ( $\theta = 1.5^\circ$ ), and in indigo, a state far away from the measurement axes ( $\theta = 45^\circ$ ). For MLE (a), the slopes of linear fits (lines) in the plot are  $-1.00 \pm 0.01$ ,  $-0.60 \pm 0.03$ , and  $-0.50 \pm 0.01$ , respectively. For LIN, they are  $-0.48 \pm 0.01$  and  $-0.50 \pm 0.01$  for  $\theta = 1.5^\circ$  and  $45^\circ$ . Data for the non-rotated state are missing, since the fidelity for the (unphysical) linearly reconstructed density matrix is always exactly equal to one in this case<sup>1</sup>.

It is clearly visible that it is advantageous to align one measurement basis to the state (as is the case for the non-rotated state), leading to Heisenberg scaling  $N^\alpha = 1/N$  (with the *scaling exponent*  $\alpha$ ) if the result is obtained by MLE. Small deviations from this optimal orientation already lead to high losses in the scaling behaviour, such that for a state far away from the measurement axis the scaling decreases to  $N^\alpha = 1/\sqrt{N}$ . When using LIN, the scaling is independent of the measurement axis.

#### 4.2.1. Diverging distributions and a postselection criterion

For a closer investigation of this phenomenon, a histogram of the fidelities of all state reconstructions at  $N = 10^5$  (Figure 4.3) is helpful. While we observe a single-peaked distribution for the non-rotated target state, the distribution for  $\theta = 45^\circ$  is split into two parts. This can be explained by looking at the states giving rise to this fidelity distribution in a projection of the Bloch sphere onto the  $T_x$ - $T_z$  plane, see Figure 4.4. Without fitting, using just the linear inversion method, roughly half of the reconstructed states will lie outside the physical state space (they will be called *initially unphysical* from here on) for a pure target state far away from the measurement axes. In contrast, states lying inside the state space even with LIN are called *initially physical*. Running the maximum likelihood algorithm does not change these already physical states, but maps the unphysical ones onto the border of the Bloch sphere, improving their fidelity. Please note that these fitted density matrices represent physical states now, but will still be called *initially unphysical* in the context of distinguishing them

from the states that were already physical before fitting. Distinguishing these two classes of states leads to the separation seen in the histogram of Figure 4.3 (b). Without MLE fitting (c), there is no difference between physical and unphysical states.

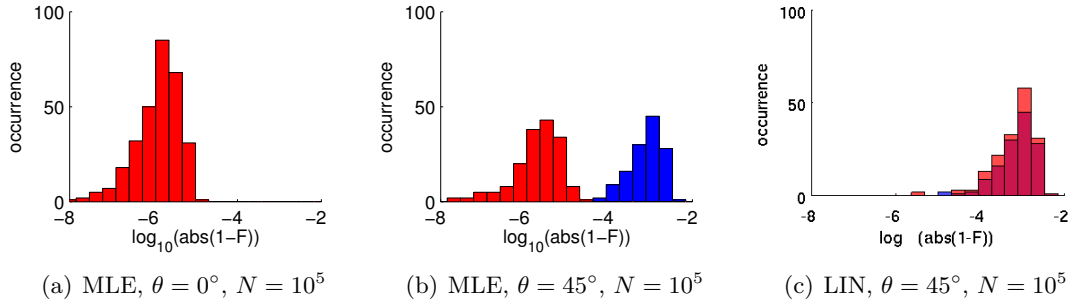


**Figure 4.3.: Histogram of infidelities.** While the histogram of 300 infidelities obtained from simulated tomographies with  $10^5$  counts per basis using MLE shows a single-peaked distribution for a non-rotated target state (a), it is split into two parts for a state rotated by  $\theta = 45^\circ$  (b). As it turns out, the two parts emerge from density matrices that correspond to **initially physical** (blue) and **initially unphysical** (red) states, respectively, when reconstructed linearly without fitting. After fitting, all states are of course physically valid, but evidently the fitting algorithm improves the result. Without fitting (LIN, (c)), the distributions of initially physical and initially unphysical states do not split.

Because of that splitting, it is not sufficient to average over all simulations and use the standard deviation as an error. Instead, a postselection is performed and the two classes of states are analysed separately. Figure 4.5 shows the infidelities for different numbers of measurements, determined using MLE but postselected on account of the physicality of the linear estimate. The averages within the groups as well as their standard deviations are shown, together with the average over all simulations for comparison. Please note that these averages are not calculated in logarithmic scale, leading to a seemingly increased importance of states with higher infidelity in the logarithmic plot.

The postselection reveals that only part of the result scales worse when the target state is far away from a measurement axis. Initially physical states, that are not affected by MLE, scale with  $1/\sqrt{N}$ , while the fitting algorithm uses knowledge about the border of the state space to provide scaling of  $1/N$  for initially unphysical states. In the case of a state perfectly aligned with a measurement axis, almost all reconstructed states are initially unphysical and benefit from fitting, therefore leading to a Heisenberg  $1/N$  scaling for all states.

This postselection analysis can be used to learn even more about state tomography and scaling behaviour. First, the focus will lie on pure states, then mixed target states will be investigated.

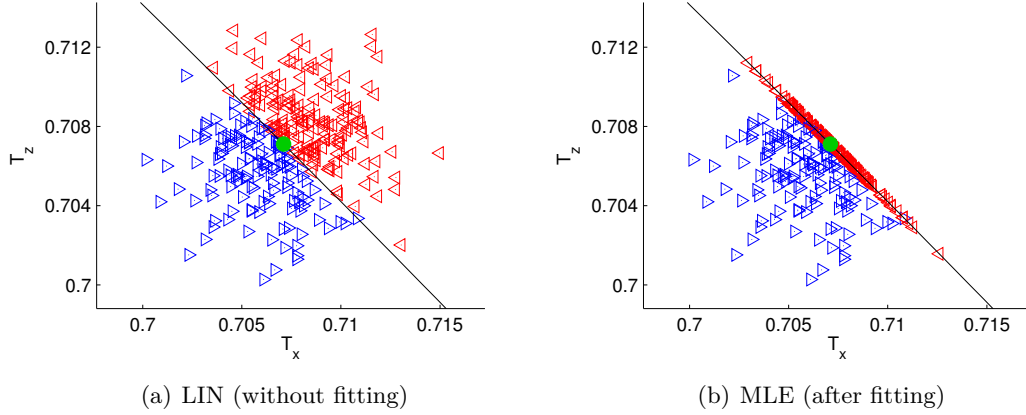


**Figure 4.4.: Section of the Bloch sphere with reconstructed states.** This section of the projection of the Bloch sphere onto the  $T_x$ - $T_z$ -plane (as in Figure 4.1) shows the position of the linearly reconstructed states (a) and their fitted counterparts (b) in relation to the target state (green dot  $\bullet$ ). The initially physical states (blue triangles  $\triangleleft$ ) are not changed by the MLE algorithm, while the initially unphysical (red triangle  $\triangleright$ ) states are mapped onto the border (black line). Note that the reconstructed states can, of course, have a non-zero  $T_y$  component because of statistics, and that this component is not visible in the projection. Here,  $N = 100000$  counts per basis were simulated for a pure target state with  $\theta = 45^\circ$ .

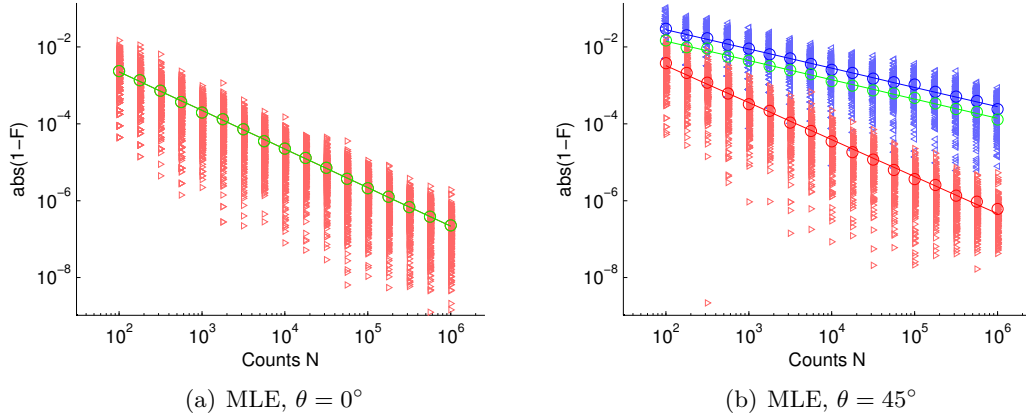


**Figure 4.5.: Scaling of infidelity with postselection.** The infidelities of all simulation results with MLE for (a) a target state aligned with the measurement axis and (b) a target state far away from them are shown. Initially unphysical states are marked by red triangles  $\triangleright$ , initially physical states by blue triangles  $\triangleleft$ . Averages and fits to them are illustrated by circles  $\circ$  and lines, while green denotes the average over all data. In (a), there are only initially unphysical states, scaling with  $\alpha = 1.00 \pm 0.01$ . For (b), approximately half of the states are initially unphysical, still scaling with  $\alpha = 0.96 \pm 0.03$ , while the other half scales with  $\alpha = 0.50 \pm 0.01$ , resulting in a scaling of  $\alpha = 0.50 \pm 0.01$  for the average over all states (not calculated in the logarithmic scale displayed in the plot, leading to a seemingly heightened importance of the states with higher infidelity).

### 4.2.2. Pure states

An interesting case is, for example, tomography of an only slightly rotated state (e.g. due to small misalignment of the measurement apparatus relative to the target state). The scaling of state tomography for such a target state is illustrated in Figure 4.6 both for LIN as well as after fitting with MLE.

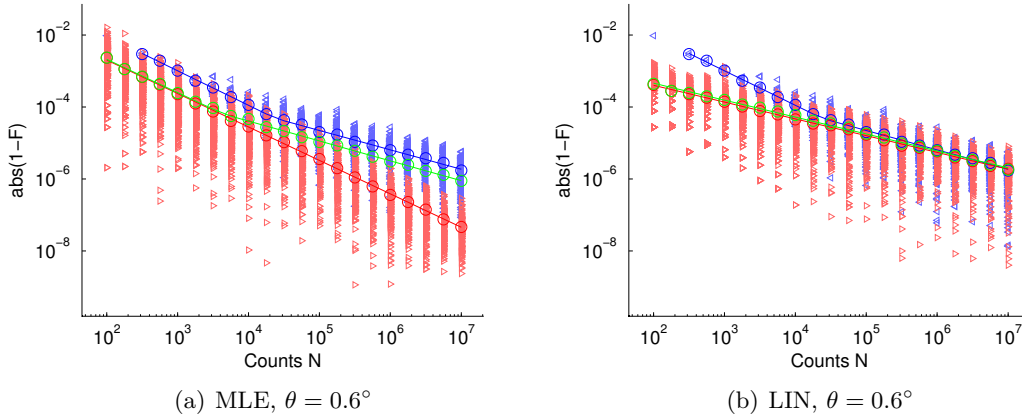


**Figure 4.6.: Slightly rotated target state.** As in previous figures, **initially unphysical** states are marked by **red triangles**  $\triangleright$ , **initially physical** states by **blue triangles**  $\triangleleft$ , averages and linear fits to them by circles  $\circ$  and lines, respectively, while **green** denotes the average over **all data**. The initially physical states remain the same for both MLE (a) and LIN (b), and they scale with  $\alpha = 0.96 \pm 0.04$  for small  $N \lesssim 30000$  and with  $\alpha = 0.54 \pm 0.03$  for large  $N \gtrsim 30000$ . The initially unphysical states scale with  $\alpha = 0.93 \pm 0.01$  for MLE and with  $\alpha = 0.47 \pm 0.01$  for LIN, as before. This leads to a bend in the mean fidelities of all states in case of MLE: First, they scale with  $\alpha = 0.93 \pm 0.05$ , then with  $\alpha = 0.55 \pm 0.02$ . Without fitting (LIN), they scale with  $\alpha = 0.47 \pm 0.01$  for all  $N$ .

Again, the initially unphysical states scale with only  $1/\sqrt{N}$  for LIN and with  $1/N$  for MLE. But, additionally, there are also initially physical states; their number increases with the number of counts until approximately half the reconstructed states are physical. Note that these states are the same for LIN and MLE, as they are not changed by the fitting algorithm. Their infidelity to the target state, however, scales differently for small ( $1 - \mathcal{F} \propto 1/N$ ) and large ( $1 - \mathcal{F} \propto 1/\sqrt{N}$ ) numbers of counts per basis.

#### Influence of discreteness

This effect can be explained by the *discrete* results of state tomography. For small  $N$ , there are only a few possible outcomes, the spacing between those is relatively large. Figure 4.7 shows the projection of the Bloch sphere, with the  $11 \times 11$  grid of possible reconstructed states in the  $T_x$ - $T_z$ -plane for  $N = 10$  counts per basis. The distance between two possible outcomes is proportional to  $1/N$ , but, as already seen in Section 4.1.2, the distribution of  $T_z$  has a standard deviation scaling with  $1/\sqrt{N}$ . Thus, for small  $N$  and especially for small initial values of the standard deviations, the distance between outcomes is much bigger than the spreading of results, therefore reducing the number of observed outcomes to only one or two values of  $T_z$ .

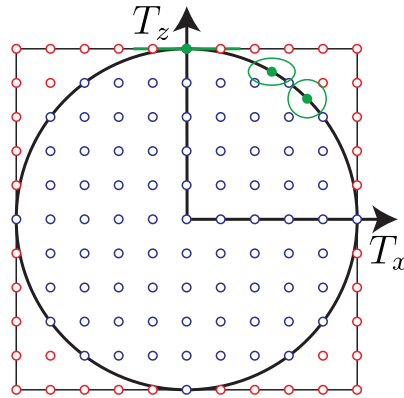


**Figure 4.7.:** Possible outcomes for state tomography with 10 counts per basis. The  $11 \times 11$  grid of statistically possible linearly reconstructed states in the  $T_x$ - $T_z$ -plane for 10 counts per basis. Each point is given by  $T_s = (c_0^s - c_1^s)/N$ , with  $c_0^s + c_1^s = N$  for  $s \in \{x, z\}$ . Physical states lying inside the sphere are marked by blue circles  $\circ$ , while the unphysical states are red. For the target states with  $\theta \in \{0^\circ, 30^\circ, 45^\circ\}$ , marked by green dots  $\bullet$ , the standard deviation of the binomial distribution (Eq. (4.10)) is shown by green ellipses.

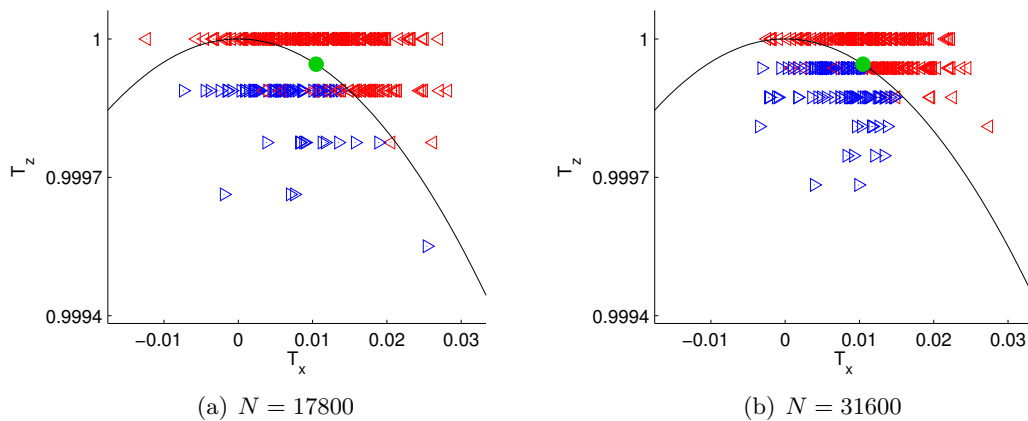


**Figure 4.8.:** Bloch representation of reconstructed states with slightly rotated target state. A small section of the Bloch sphere is shown. Please note the different scaling of the axes due to the high asymmetry of the distribution. In the  $T_z$  direction, discretisation plays an important role, since the distance between possible outcomes is large in comparison to the spreading of the theoretical binomial distribution. The target state is depicted by a green dot  $\bullet$ , initially physical states by blue triangles  $\triangleleft$  and initially unphysical states by red triangles  $\triangleright$ .

Since the bend in Figure 4.6 (a) is situated around  $N = 30000$  for  $\theta = 0.6^\circ$ , we examine the distribution of reconstructed states on the Bloch sphere for close-by  $N$ . The two cases  $N = 17800$  and  $N = 31600$  are shown in Figure 4.8. It becomes clear that for  $N$  smaller than 17800, the most significant effect on the scaling of reconstruction fidelity of initially physical states is not the width of the binomial distribution, but the distance between the target state and the second row of possible results, since that is the first row containing physical results. Not before this second row is nearer to the target state than the first one, the fidelity of initially physical states will scale with the distance between the rows and therefore with  $1/N$ . To support this conjecture, Figure 4.9 shows the position of the bend with respect to the angle  $\theta$  characterising the target state compared to a theoretical line marking the above mentioned point where the target state lies halfway between the two first rows of possible outcomes,

$$1 - \frac{N - 2}{N} = 2 - 2 \cos \theta . \quad (4.12)$$

The positions of the bends fit quite well to the theoretical line, but deviations from the line seem to grow systematically with the rotation angle  $\theta$ . This is presumably caused by the binomial distribution becoming less narrow and spanning more rows of possible outcomes.

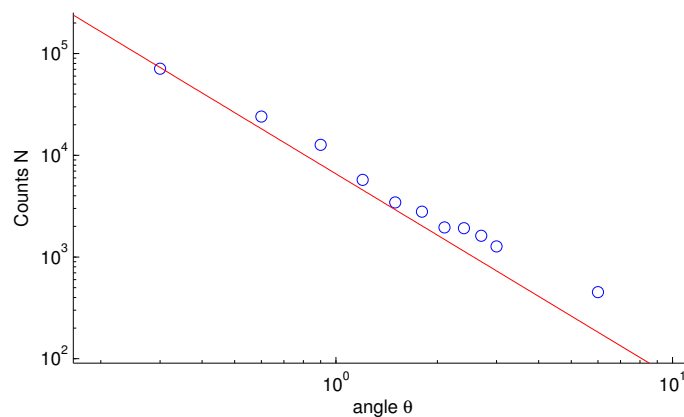


**Figure 4.9.: Position of bend in scaling of initially physical states.** For differently rotated target states, the position of the bend in the scaling of the initially physical states is shown, as obtained by simulation (blue circles  $\circ$ ). Additionally, the red line is calculated by setting the distance between possible reconstructed states equal to double the distance of the target state to the  $T_z = 1$  line, see Eq. (4.12). Deviations from the line seem to grow systematically towards larger angles  $\theta$ , which is probably due to influences of the binomial distribution becoming more important.

### Flattening of scaling in fitted reconstructed states

An additional phenomenon becomes visible at very high numbers of counts per basis. The fitted initially unphysical states do not scale as good as for lower numbers of counts, as if there would be a maximum fidelity of approximately  $1 - 10^{-8}$ , see Figure 4.10.

At first glance, numerical reasons in the simulation procedure seem likely, e.g. insufficient precision of variables. But a recalculation with increased precision yields the same results, and for other target states, see e.g. Figure 4.10 (b), lower infidelities up to  $10^{-10}$  are reached. The reason for this flattening is therefore still unknown.

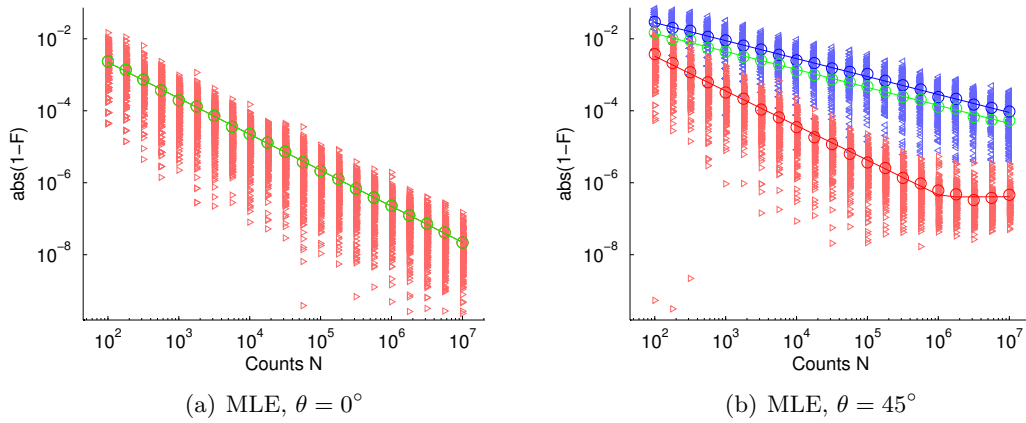


**Figure 4.10.: Flattening of scaling of initially unphysical states.** For target states far away from one of the measurement axes (b), there seems to be a maximally reachable fidelity of about  $1 - 10^{-8}$ , the **initially unphysical states (red)** exhibit a scaling behaviour of  $\alpha = -0.96 \pm 0.03$  for low numbers of counts, but  $\alpha = 0.0 \pm 0.2$  at high count rates. Numerical reasons seem likely at first, but a recalculation with increased precision yields the same result and, for target states aligned with a measurement axis (a), lower infidelities are possible. Here, the reconstructed states' fidelities scale with  $\alpha = -1.00 \pm 0.01$  for the whole range of count rates, reaching infidelities of  $10^{-10}$ . Thus, a convincing explanation has not yet been found.

### 4.2.3. Mixed states

Even if one often aims for a pure state, in an actual experiment noise and imperfections will lead to a mixed state in the experiment. Thus, one also has to consider such states as target states. To analyse the effect of a little added noise, target states with a fidelity of  $\mathcal{F}_t = 99.9\%$  to the corresponding pure state are investigated. With the help of discerning between states that lie outside the Bloch sphere before fitting and those that lie inside, the effects of the border of the state space can be studied.

#### Effects of the state space border

It was already shown in Ref. [56, 58, 59] that, measured by infidelity, quantum state tomography scales with  $1/N$  for target states deep inside the Bloch sphere. This can be seen with a Taylor expansion of the infidelity (in terms of the target state  $\rho_t$ 's eigenbasis  $\{|i\rangle\}$ ) [56]

$$1 - \mathcal{F}(\rho, \rho + \epsilon\Delta) = \frac{1}{4} \sum_{i,j} \frac{\langle i | \Delta | j \rangle^2}{\langle i | \rho | i \rangle + \langle j | \rho | j \rangle} + \mathcal{O}(\Delta^3), \quad (4.13)$$

with the error matrix  $\Delta = \rho_{rec} - \rho_t$ . Typically, errors scale as  $|\Delta| \propto 1/\sqrt{N}$ . Thus, the infidelity scales with  $|\Delta|^2 \propto 1/N$ , except when an eigenvalue  $\langle i | \rho | i \rangle$  is nearly 0. In that case, namely when the state is almost pure (in comparison to the width of the distribution of reconstructed states), the infidelity becomes linear in  $\Delta$  and therefore proportional to  $1/\sqrt{N}$  [56]. This is also seen in our simulations, see Figure 4.11, and happens for all mixed target states.

Additionally, there are no initially unphysical states when the number of counts is high enough for the distribution of reconstructed states to lie completely in the interior of the

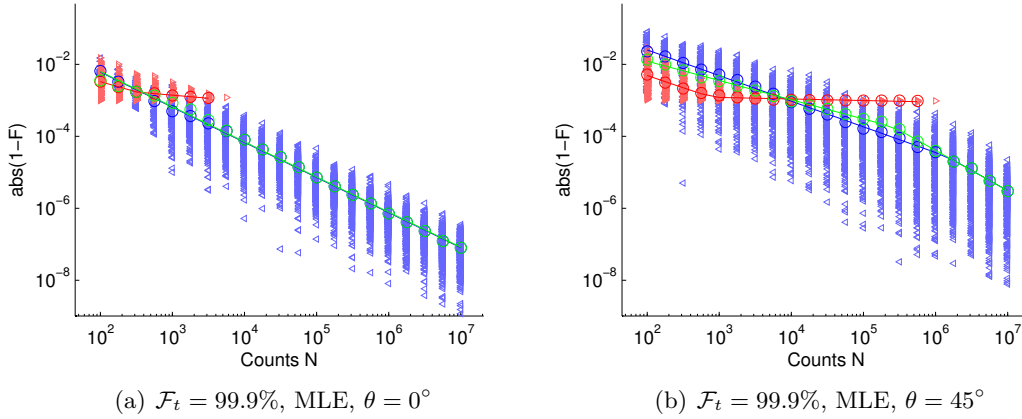


**Figure 4.11.: Scaling for mixed states with MLE.** For mixed target states aligned with a measurement axis (a), the transition from initially unphysical reconstruction results to almost only initially physical states happens at quite small count numbers, because the variance of the distribution in  $T_z$  direction is very small. The **initially physical states** scale with  $\alpha = -0.98 \pm 0.02$  for all count rates, while the **initially unphysical states** scale with  $\alpha = -0.57 \pm 0.09$  for low counts and level out with  $\alpha = -0.17 \pm 0.06$  before disappearing completely. If **all QST results** are considered, this leads to a scaling of  $\alpha = -0.57 \pm 0.09$  and  $\alpha = -1.02 \pm 0.01$ , respectively. For target states with  $\theta = 45^\circ$  (b) the bend happens at far larger count numbers, but is also there. Here, the exponents  $\alpha$  for small and large  $N$  are  $-0.71 \pm 0.02$  and  $-1.1 \pm 0.1$ ,  $-0.7 \pm 0.1$  and  $-0.04 \pm 0.02$ ,  $-0.54 \pm 0.02$  and  $-1.12 \pm 0.06$ , respectively.

Bloch sphere. At lower count rates, the fidelity of these states levels out at  $\mathcal{F} = 1 - 10^{-3}$ , simply because all MLE results lie on the border of the Bloch sphere and therefore cannot be nearer to the target state than that.

### Uhlmann fidelity

The situation when reconstructing the state just linearly (LIN) without fitting is plotted in Figure 4.12. A very peculiar effect is seen for target states strongly differing from eigenstates of the measurement basis: The limit of  $1 - 10^{-3}$  for fidelities of unphysical states is not valid anymore, and the mean fidelities of these states actually get worse after a certain number of counts.

But, at closer investigation, it becomes clear that this is due to the used measure, the Uhlmann infidelity, which is not defined for unphysical states lying outside the Bloch sphere. Figure 4.13 (a) shows the infidelity of states over the Bloch sphere to a pure target state. Here, only the length of the projection onto the direction of the target state matters, states outside the Bloch sphere can achieve infidelities below 0. This is not a problem, since we used the absolute value of the infidelity, such that a minimum was achieved only in a line containing the target state. However, when measuring the fidelity in comparison to a mixed target state (Figure 4.13 (b)), the situation changes. For an only slightly mixed target state, in a small region outside the Bloch sphere (Figure 4.13 (c)), infidelity is higher at the border and decreases to 0 with increased distance, such that there are multiple regions with minimal infidelity. One contains the target state, but the other lies outside the Bloch sphere.

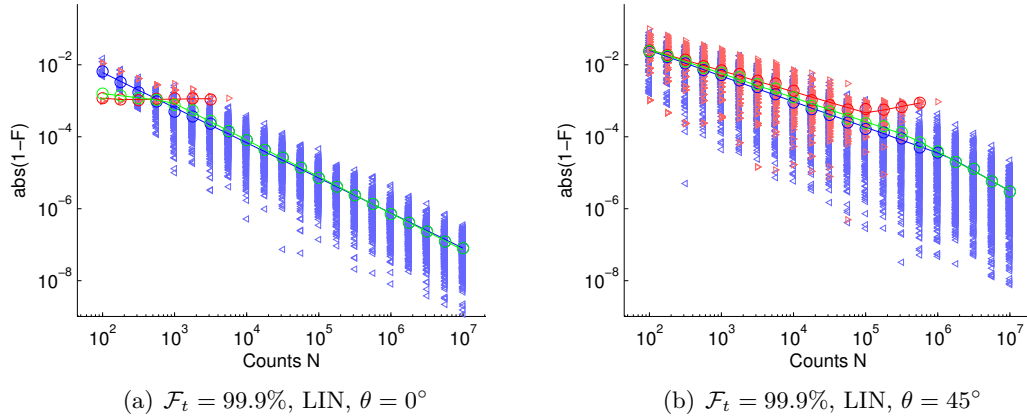


**Figure 4.12.: Scaling for mixed states with LIN.** The initially physical states are of course the same as in Figure 4.11, and scale with (a)  $\alpha = -0.98 \pm 0.02$  and (b)  $-0.71 \pm 0.02$  and  $-1.1 \pm 0.1$ . But the initially unphysical states exhibit a quite different behaviour: While not scaling at all ( $\alpha = 0.00 \pm 0.04$ ) for  $\theta = 0^\circ$ , their infidelity actually “turns around” and gets worse with  $\alpha = 0.4 \pm 0.4$  (for mediocre count rates) after starting out with  $\alpha = -0.59 \pm 0.04$  (for low count rates) for  $\theta = 45^\circ$ . This causes the average infidelity of all reconstructed states to (a) scale poorly with  $\alpha = -0.24 \pm 0.10$  for low counts and very good ( $\alpha = -1.02 \pm 0.01$ ) for high counts and (b) to scale with  $\alpha = -0.67 \pm 0.03$  and  $\alpha = -1.09 \pm 0.10$ , respectively, for a misaligned target state.

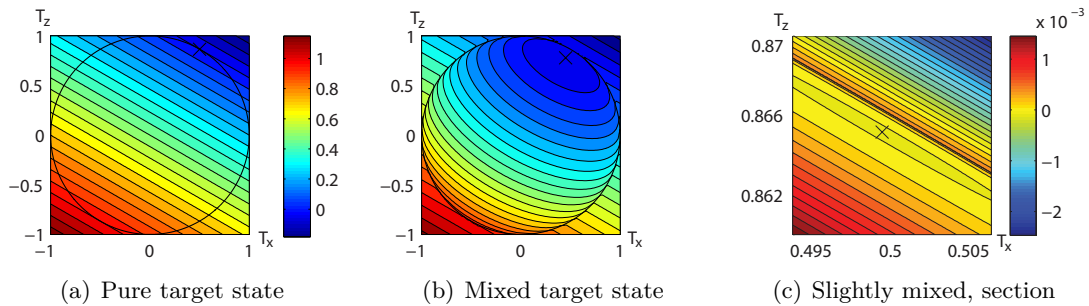


**Figure 4.13.: Illustration of Uhlmann infidelity.** The Uhlmann infidelity with respect to a pure (a) or mixed (b,c) target state (marked by a black cross  $\times$ ). (a) and (b) show the whole Bloch sphere and use the same color code. (c), however, shows only a small section of the sphere, the color code is therefore different.

Therefore, if the distribution of reconstructed states becomes so small, that the outermost initially unphysical states can not fall in this second region with minimal infidelity anymore, the infidelity of these states increases with the number of counts, as seen in the simulations.

### 4.3. Extension to more qubits

When trying to extend the postselection criterion to multi-qubit states, it is important to know that it gets increasingly unlikely to obtain an initially physical state by linear inversion, due to the increasing dimensionality of the Hilbert space. In the case of the pure two-qubit target states used here,

$$|\psi_t^{(\text{sep})}\rangle = \mathbb{1}^{(2)} \otimes U |HH\rangle \quad \text{and} \quad (4.14)$$

$$|\psi_t^{(\text{ent})}\rangle = \mathbb{1}^{(2)} \otimes U |\phi_-\rangle, \quad (4.15)$$

(with the rotation operator  $U$  defined above) it is almost impossible because one of the qubits is aligned with a measurement axis. Therefore, it is not meaningful to discern between “initially physical” and “initially unphysical” states anymore, as before. Nevertheless, simulations still show diverging distributions. This section shows how it is possible to discern states of these distributions for product and entangled states, and analyses which of the single qubit effects are still there.

#### 4.3.1. Product states

With the target state being a product state, there is still a meaningful choice for a discriminating criterion, namely *partial physicality*: If a state is unphysical, but partially tracing out one of the qubits results in a physical single qubit state, we call the whole state *partially physical*. For example, if the target state is a pure product state with  $\theta = 45^\circ$  (i.e. the first qubit is still aligned with the  $\sigma_z$ -axis while the second qubit is rotated by  $45^\circ$  in direction of  $\sigma_x$ ), tracing out the second qubit of a simulated and reconstructed state will almost always result in an initially unphysical state, as the remaining qubit is aligned with a measurement axis. In contrast, tracing out the first qubit yields initially physical results approximately half the time.

And indeed, as seen in Figure 4.14 and Figure 4.15, this criterion works to discern the states belonging to the two different distributions. We now distinguish three classes of states: Those that are initially physical, those that are only partially physical and those that are not partially physical (initially entirely unphysical) states after linear reconstruction. Here, only two classes are present, as there are no states that are completely physical. With that, there is actually an astonishing similarity to the single qubit case: Initially unphysical states exhibit infidelities of the same order of magnitude whether the state is rotated or not and scale with  $\alpha = -1$ , while the (partially) physical states show results with increased infidelity for a rotated target state. Only the widths of the distribution differ from the single qubit case, the distribution of initially unphysical states is narrower, while the distribution of partially physical states is a bit broader.

An interesting fundamental difference between the single qubit and the product state is that the fitting algorithm used for MLE does intrinsically not change an already physical state in

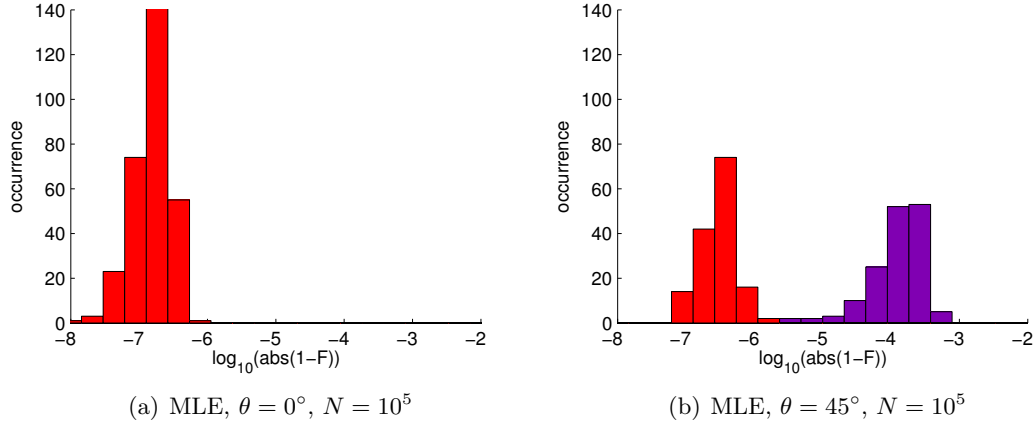


**Figure 4.14.: Histogram of infidelities for a two-qubit product state.** As above, simulated tomographies with  $10^5$  counts per basis using MLE result in a single-peaked distribution for a non-rotated target state (a), but a split distribution for a state rotated by  $\theta = 45^\circ$  (b). As in the previous chapter, **initially unphysical states** are colored red, while the **partially physical states** are lilac.

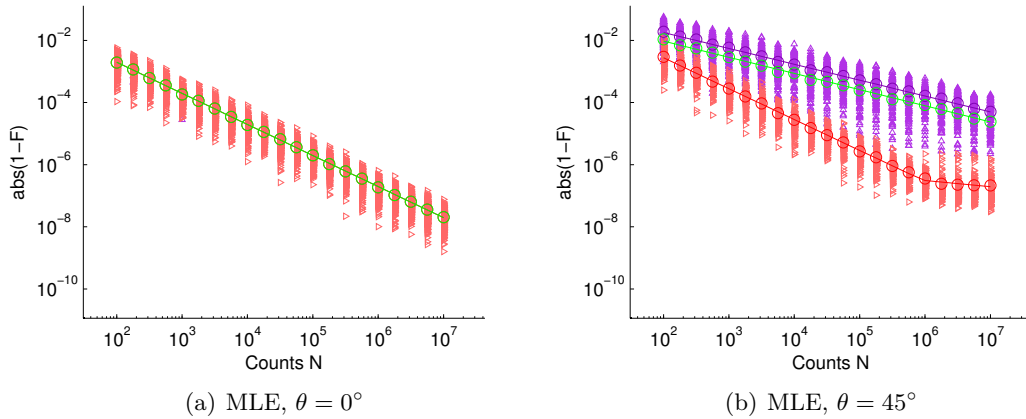


**Figure 4.15.: Scaling for pure product states with MLE.** Like for a single qubit, the infidelities of reconstructed states scale with  $\alpha = -1.00 \pm 0.01$  for a non-rotated state (a) because all of them are initially unphysical. Also just like in the single qubit case, there are two diverging distributions for rotated target states (b). **Initially unphysical states** are depicted by red triangles  $\triangleright$ , while **partially physical states** are represented by lilac triangles  $\triangle$ . They scale with  $\alpha = -0.99 \pm 0.02$  (and  $\alpha = -0.20 \pm 0.09$  for higher numbers of counts) and  $\alpha = -0.51 \pm 0.01$ , respectively, resulting in a scaling of  $\alpha = -0.52 \pm 0.01$  for the mean over all states, depicted in green circles  $\circ$ .

the single qubit case, while here, all states are fitted to the Bloch border since none of them is already completely physical. The fact that there is still an observable difference between the distributions points to different classes of fitting behaviour for multi-qubit initially unphysical states.

Figure 4.15 also shows the flattening of the initially unphysical states as in the single qubit case, which remains without explanation yet. The discreteness effect can also be seen for slightly rotated target states ( $\theta = 0.6^\circ$ ), see Figure 4.16. The effect is even more clear when the partially physical states have been fitted by MLE.

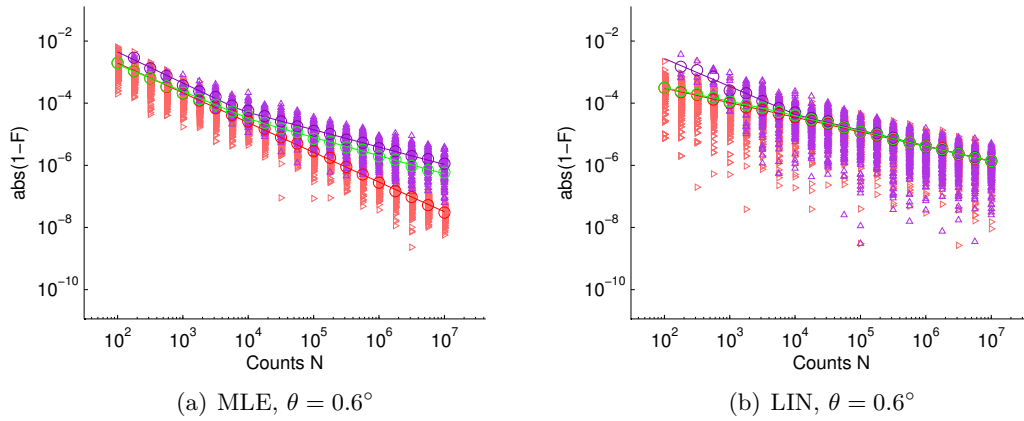


**Figure 4.16.: Discreteness in product states.** The effect of discreteness explained in the previous section is also seen for slightly rotated pure product states. For MLE (a), **initially unphysical states** scale with  $\alpha = -0.96 \pm 0.01$ , while **partially physical states** scale with  $\alpha = -1.00 \pm 0.06$  for low count rates and with  $\alpha = -0.56 \pm 0.03$  for high count rates. When reconstructed linearly (b), **initially unphysical states** scale only with  $\alpha = -0.47 \pm 0.01$ . In contrast to the single qubit case, fitting changes the infidelities of the **partially physical states**, such that these scale differently for LIN:  $\alpha = -0.90 \pm 0.07$  for low numbers of counts and  $\alpha = -0.50 \pm 0.04$  for higher numbers.

### Mixed product states

The situation changes for mixed product states because initially physical states are possible now and will occur for large enough numbers of counts. Simulation results for target states with a fidelity of  $\mathcal{F} = 99.9\%$  to the corresponding pure state with  $\theta = 0^\circ$  and  $\theta = 45^\circ$ , reconstructed with MLE, are shown in Figure 4.17.

Compliant with Ref. [60], the transition from only partially physical to physical reconstruction results happens in a quite small range of numbers of counts. A flattening of the infidelity curve can be seen, as in the single qubit case, only that it occurs for partially physical states and leads to a flat scaling of the infidelity of all states. When performing an experiment, that means that almost no improvement is seen when using  $N = 10^6$  counts instead of only  $N = 10^4$ , even though measuring  $N = 10^6$  counts per basis is potentially a hundredfold the effort!

It is also very interesting that, for mediocre numbers of counts per basis, the fidelity is worse for states fitted to the state space border by MLE compared to the linearly reconstructed states, see Figure 4.18. Additionally, the effect due to the (not well defined for unphysical

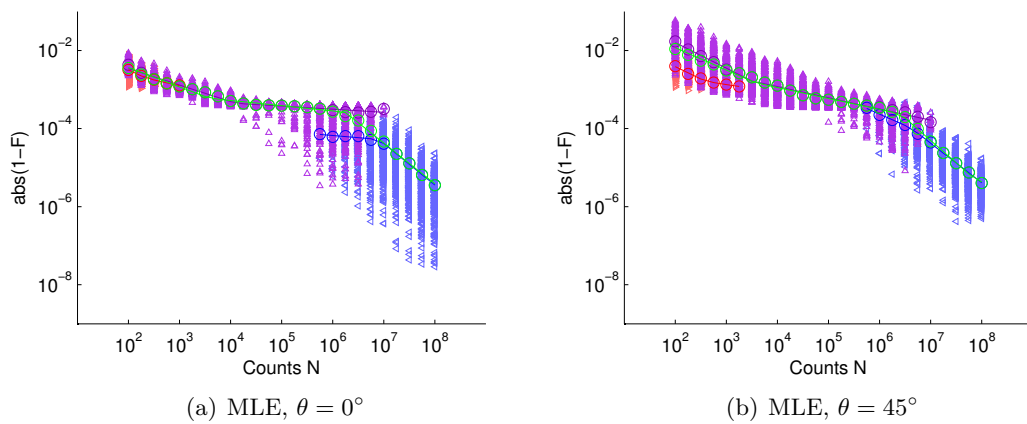


**Figure 4.17.: Mixed product states reconstructed using MLE.** For a non-rotated target state (a), there are still **initially unphysical results** for low counts, scaling poorly with  $\alpha = -0.4 \pm 0.1$ . For mediocre count numbers, there are only **partially physical states**, first scaling with  $\alpha = -0.42 \pm 0.05$ , then flattening to  $\alpha = -0.08 \pm 0.03$ . At high count rates, **initially physical states** take over, scaling with  $\alpha = -0.11 \pm 0.09$  first and, when the distribution enters the state space completely, with  $\alpha = -1.07 \pm 0.09$ . All this combined leads to a tripartite scaling behaviour of **all simulation results**: First scaling with  $\alpha = -0.50 \pm 0.02$ , the infidelities level out to  $\alpha = -0.13 \pm 0.05$ , and join the initially physical states with  $\alpha = -1.04 \pm 0.09$  at very high count rates. Similarly, for the rotated target state (b), the **initially unphysical states** scale with  $\alpha = -0.4 \pm 0.2$ , the **partially physical states** with  $\alpha = -0.66 \pm 0.10$  at first, then with  $\alpha = -0.29 \pm 0.03$ . Again, **initially physical states** take over at high count rates, scaling with  $\alpha = -0.58 \pm 0.07$  first and with  $\alpha = -1.01 \pm 0.04$  later. Here, that leads to a **combined** scaling of  $\alpha = -0.57 \pm 0.02$ ,  $\alpha = -0.28 \pm 0.03$ , and  $\alpha = -1.15 \pm 0.09$ , respectively.

states) Uhlmann fidelity as seen in Section 4.2.3 reappears here. Interestingly, that bend happens before the initially physical states can take over completely and can lead to a short worsening of the average infidelity with increasing numbers of counts. But, of course, the states still get better, it is important to keep in mind that this measure is faulty here.

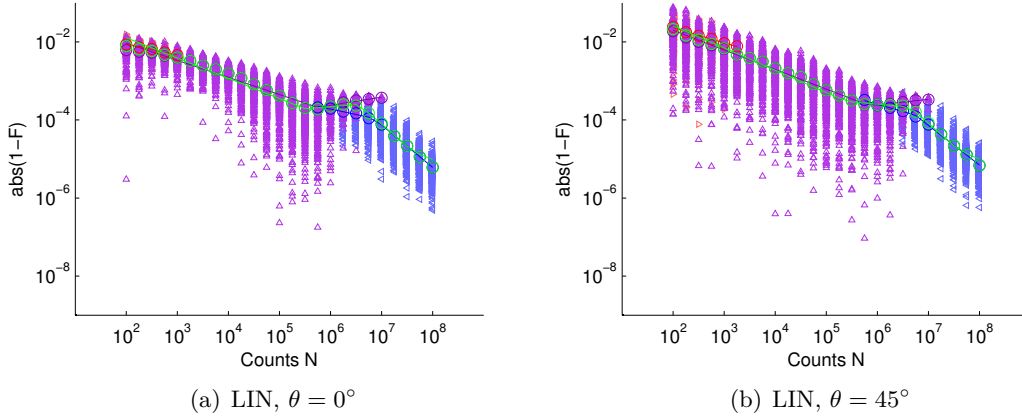


**Figure 4.18.: Mixed product states reconstructed using LIN.** For the non-rotated target state (a), infidelities of **partially physical states** start to scale with  $\alpha = -0.44 \pm 0.04$ , but then rise again with  $\alpha = 0.2 \pm 0.2$ . Similarly, for a state far away from the measurement axes (b), infidelities scale with  $\alpha = -0.50 \pm 0.02$  and  $\alpha = 0.15 \pm 0.10$ , respectively. Here, this can also give rise to a worsening in the **combined infidelity** curve. For  $\theta = 0^\circ$  (a), it scales with  $\alpha = -0.52 \pm 0.03$ ,  $\alpha = 0.1 \pm 0.3$ , and  $\alpha = -1.1 \pm 0.4$ , for low, medium and high numbers of counts, respectively, and for  $\theta = 45^\circ$  (b) with  $\alpha = -0.57 \pm 0.02$ ,  $\alpha = -0.1 \pm 0.2$  and  $\alpha = -1.2 \pm 0.3$ .

### 4.3.2. Maximally entangled states

The postselection criterion introduced for two-qubit product states does not work for entangled states, because a partial trace always leads to a state near the maximally mixed state, which will almost always be initially physical. Nevertheless, two diverging infidelity distributions are still clearly visible in tomographies of simulated measurement data for a target state with  $\theta = 45^\circ$  and reconstructing the state using MLE, see Figure 4.19.

It is possible to distinguish states belonging to these two distributions by checking the eigenvalues of the linearly reconstructed states. A state is physical if all eigenvalues are positive. Unphysical density matrices have negative eigenvalues, which may also lead to an eigenvalue bigger than 1, since the sum of eigenvalues still has to be equal to 1. Here, we call a state *semi physical*, when it is unphysical, but the highest eigenvalue is still smaller than 1 (before a potential fit with MLE). With that criterion, the diverging distributions can be described very well, see also Figure 4.20. Please note that this criterion could, theoretically, be employed to discern product states as well. Unfortunately though, it does not work in practice, as there are partially physical states that are not semi physical and vice versa.

As in the previous cases of single qubit and two-qubit product state, initially unphysical states scale with  $1/N$ . The flattening of the infidelity curve can be seen for initially unphysical states fitted by MLE when employing rotated target states. The discreteness effect described above can be observed as well in simulations using a slightly rotated ( $\theta = 0.6^\circ$ ) target state, see

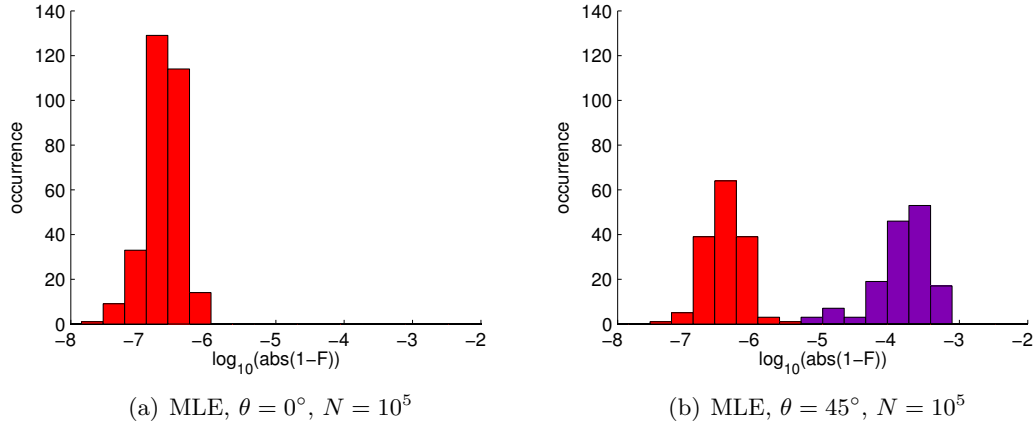


**Figure 4.19.: Histogram of infidelities for a two-qubit maximally entangled state.** As seen before, simulated tomographies with  $N = 10^5$  counts per basis using MLE result in a single-peaked distribution for a non-rotated target state (a), but a split distribution for a state rotated by  $\theta = 45^\circ$  (b). As before, **unphysical states** are colored **red**, while the states we call *semi physical* are **lilac**.

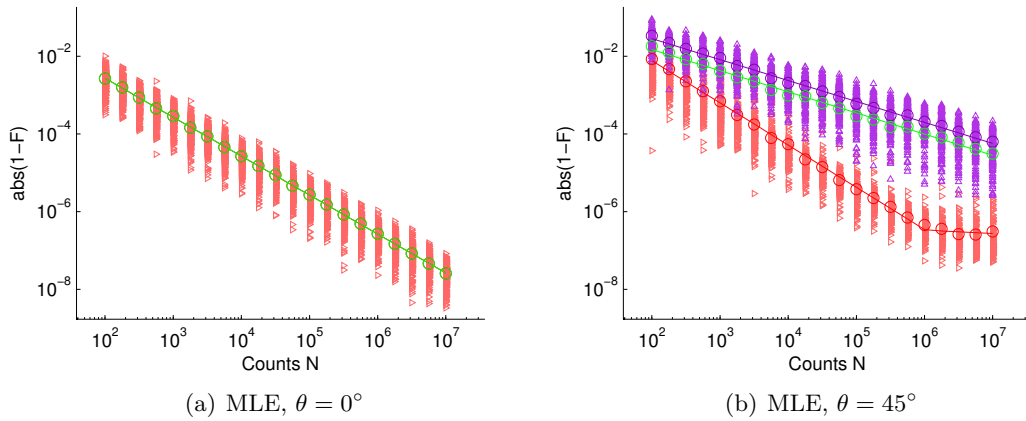


**Figure 4.20.: Scaling for pure maximally entangled states with MLE.** As before, there is only a single distribution when using a non-rotated target state (a) (scaling with  $\alpha = -1.00 \pm 0.01$ ), but two diverging distributions for  $\theta = 45^\circ$  (b). The **semi physical states**, denoted by **lilac triangles**  $\triangle$ , scale with  $\alpha = -0.54 \pm 0.01$  in this case, while the **initially unphysical states** also show the flattening seen before for single qubits as well as product states: Scaling with  $\alpha = -1.09 \pm 0.03$  for low numbers of counts, the infidelities don't decrease anymore ( $\alpha = -0.1 \pm 0.2$ ) for high numbers of counts.

Figure 4.21. As before, discrete possible state reconstruction outcomes lead to an improved scaling of semi physical states at low count rates.

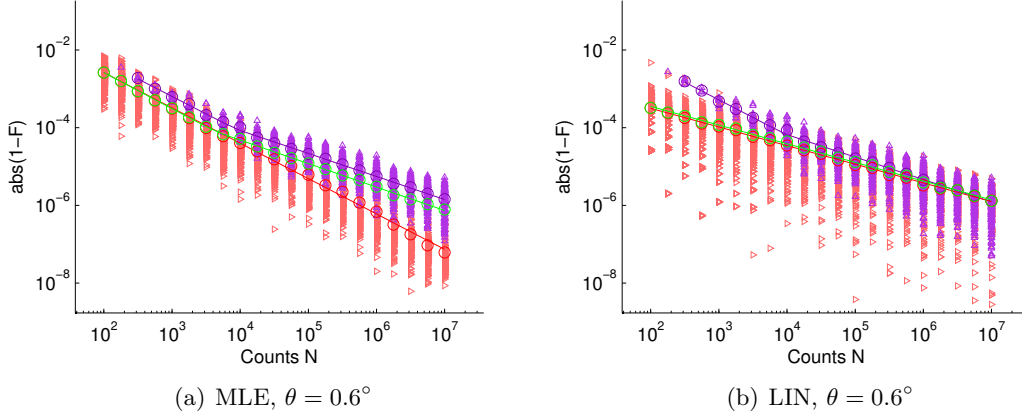


**Figure 4.21.: Discreteness in maximally entangled states.** When using MLE (a), the infidelities of the **initially unphysical states** scale with  $\alpha = -0.91 \pm 0.02$ , while the **semi physical states** scale with  $\alpha = -0.9 \pm 0.07$  and  $\alpha = -0.59 \pm 0.02$  for low and high count rates, respectively. This results in a bend in the behaviour of the mean infidelity over **all states**, scaling with  $\alpha = -0.93 \pm 0.04$  and  $\alpha = -0.61 \pm 0.01$ . When reconstructing the states linearly (b), the scaling exponents are  $\alpha = -0.48 \pm 0.01$ ,  $\alpha = -0.91 \pm 0.08$  and  $\alpha = -0.58 \pm 0.03$ , and  $\alpha = -0.48 \pm 0.01$ , respectively.

Additionally, there is an extra effect that is not appearing in single qubit or product states. For states rotated by about  $\theta \in [1^\circ, 6^\circ]$ , initially unphysical states scale worse for low counts when reconstructed using MLE, see Figure 4.22. It seems as if the infidelity curves of semi physical and initially unphysical states would not cross each other. An explanation has not yet been found. A better understanding of the criterion to distinguish between semi physical and unphysical density matrices would, presumably, help to solve the problem.

### Mixed entangled states

The infidelities of state tomography with an entangled target state essentially behave as for product target states. In Figure 4.23, the flatness of the infidelity averaged over all states can be seen again for the range between  $N = 10^4$  and  $N = 10^6$  counts (for a non-rotated target state). It is also interesting that, when comparing to the linear results (Figure 4.24), maximum likelihood estimation has a greater benefit on initially unphysical states than it has on semi physical states, especially for target states not aligned with the measurement basis.

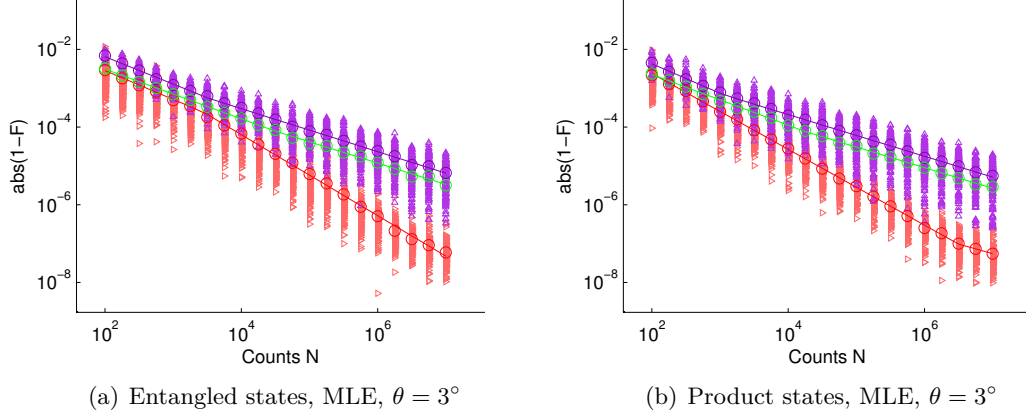


**Figure 4.22.: Additional effect in entangled states.** There is an additional bend in the infidelities of **initially unphysical states** when using a maximally entangled target state rotated by only a small angle  $\theta$  (a), that is not there for a product target state (b). Infidelities scale with  $\alpha = -0.74 \pm 0.11$  before steepening again to  $\alpha = -1.04 \pm 0.03$  for entangled target states, while scaling with  $\alpha = -0.98 \pm 0.01$  already at low numbers of counts for product states.

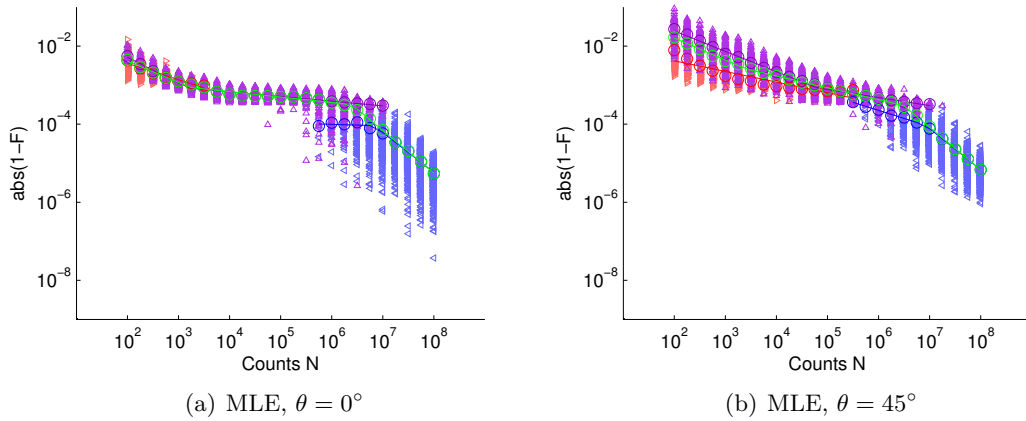


**Figure 4.23.: Mixed entangled states, reconstructed using MLE.** Also for entangled states aligned with a measurement axis (a), the infidelity of **semi physical states** levels out for high count numbers, scaling with  $\alpha = -0.66 \pm 0.11$  at first and with  $\alpha = -0.12 \pm 0.02$  later. Again, **initially physical states** take over quickly while scaling with  $\alpha = 0.0 \pm 0.2$ , then with  $\alpha = -1.0 \pm 0.2$ . For low numbers of counts, there are also **initially unphysical states** scaling with  $\alpha = -0.42 \pm 0.11$ . All this leads to exponents  $\alpha$  of  $-0.55 \pm 0.11$ ,  $-0.14 \pm 0.03$  and  $-1.09 \pm 0.07$  for the **average over all results** for respective regimes of counts  $N$ . For a rotated state (b) exponents  $\alpha$  are given by  $-0.59 \pm 0.09$  and  $-0.12 \pm 0.05$ ,  $-0.52 \pm 0.02$  and  $-0.20 \pm 0.04$ ,  $-0.41 \pm 0.04$  and  $-1.05 \pm 0.05$ , and  $-0.56 \pm 0.01$ ,  $-0.30 \pm 0.01$ , and  $-1.09 \pm 0.05$ , for **initially unphysical**, **semi physical**, **initially physical**, and **average over all states**, respectively.

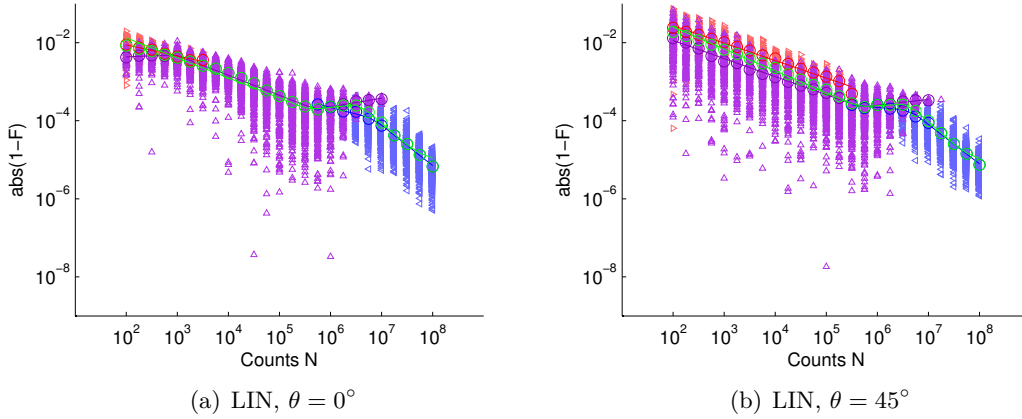


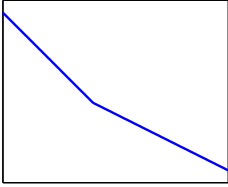
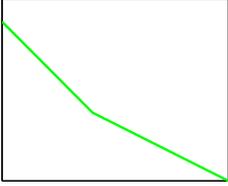
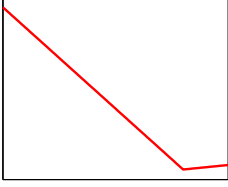
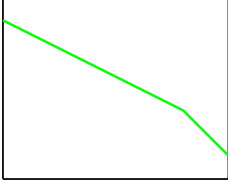
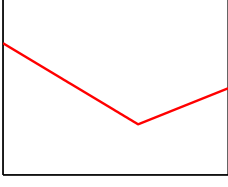
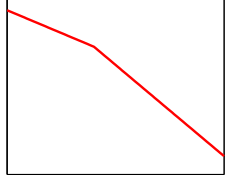
**Figure 4.24.: Mixed entangled states, reconstructed using LIN.** When linearly reconstructing states with  $\theta = 0^\circ$  (a), *semi physical states* exhibit worsening infidelities for low numbers of counts ( $\alpha = 0.05 \pm 0.15$ ), scale better for mediocre count rates ( $\alpha = -0.51 \pm 0.03$ ) and disappear with  $\alpha = 0.22 \pm 0.08$  for high numbers of counts. *Initially physical states* set in, scaling with  $\alpha = -1.04 \pm 0.11$ . This leads to a scaling exponent  $\alpha$  of  $-0.51 \pm 0.03$ ,  $0.1 \pm 0.4$ , and  $-1.1 \pm 0.4$  for the average infidelity of *all states*. For a rotated state (b) exponents  $\alpha$  are given by  $-0.45 \pm 0.03$ ,  $-0.46 \pm 0.02$  and  $-0.15 \pm 0.08$ ,  $-0.12 \pm 0.13$  and  $-1.01 \pm 0.10$ , and  $-0.56 \pm 0.02$ ,  $0.0 \pm 0.3$ , and  $-1.1 \pm 0.3$ , for *initially unphysical*, *semi physical*, *initially physical*, and *average over all states*, respectively. Note that, contrary to MLE-fitted states (Figure 4.23), *initially unphysical states* have higher infidelity than *semi physical states*.

## 4.4. Conclusion

In this chapter, an intuitive understanding of quantum state tomography schemes was developed. Linear inversion, as well as maximum likelihood estimation, were employed to evaluate simulated measurements for target states that were differently aligned with respect to the measurement axes to investigate scaling effects that were observed (and even used) in other works before. Table 4.1 provides an overview. We discovered that there is often not a single-peaked distribution describing the fidelities of reconstructed states, but two diverging peaks, and provided a criterion by which these can be distinguished for single qubit tomography. We extended this criterion to two-qubit product and maximally entangled states. With the help of these criteria, multiple astonishing behaviour patterns of infidelity scaling, present in both single qubit and two-qubit (product as well as entangled) state tomography, can be observed and described. The best scaling was achieved only for mixed target states deep within the Bloch sphere and sometimes for *initially unphysical* state reconstructions that were fitted by maximum likelihood estimation.

Further work is needed to develop an understanding of the different kinds of unphysicality discovered here. A satisfactory explanation is still missing for some of the effects we observed, and the used method could be tested on systems with an even higher dimension, e.g. three-qubit systems. Maybe there will be even more “classes of unphysicality”, as there are different kinds of entangled states as well. With that understood, it might be possible to calculate error regions for tomographical state reconstructions, depending on parameters like the number of counts, the used method and the reconstructed state’s initial physicality.

**Table 4.1.: Overview of all observed scaling effects.** The illustrations show an example plot of infidelity vs. number of counts. The colors are used as before: green denotes the average over all states, blue the initially physical states, and red the initially unphysical states.

	<p>Observable for: i. physical states, LIN+MLE, <math>\mathcal{F}_t = 1</math>, <math>\theta \lesssim 9^\circ</math></p> <p>Seen before: no</p> <p>Explanation: discrete range of possible measurement outcomes <math>T_i</math></p> <p>Extension: partially physical product states; semi physical entangled states</p>
	<p>Observable for: average of all states, MLE, <math>\mathcal{F}_t = 1</math>, <math>\theta \lesssim 9^\circ</math></p> <p>Seen before: no</p> <p>Explanation: bipartite diverging distribution on a log-scale</p> <p>Extension: product states; entangled states</p>
	<p>Observable for: i. unphysical states, MLE, <math>\mathcal{F}_t = 1</math>, <math>\theta \in [3^\circ, 45^\circ]</math></p> <p>Seen before: no</p> <p>Explanation: none yet</p> <p>Extension: i. unphysical product states; unphysical entangled states</p>
	<p>Observable for: average of all states, LIN+MLE, <math>\mathcal{F}_t &lt; 1</math>, <math>\theta \in [0^\circ, 45^\circ]</math></p> <p>Seen before: yes, [39]</p> <p>Explanation: distribution of reconstructed states enters state space entirely</p> <p>Extension: product states; entangled states</p>
	<p>Observable for: i. unphysical states, MLE, <math>\mathcal{F}_t &lt; 1</math>, <math>\theta \in [0^\circ, 45^\circ]</math></p> <p>Seen before: no</p> <p>Explanation: i. unphysical state are as far away as state space border</p> <p>Extension: partially physical product states; semi physical entangled states</p>
	<p>Observable for: i. unphysical states, LIN, <math>\mathcal{F}_t &lt; 1</math>, <math>\theta \gtrsim 2^\circ</math></p> <p>Seen before: no</p> <p>Explanation: the Uhlmann fidelity is not well defined</p> <p>Extension: partially physical product states; semi physical entangled states</p>
	<p>Observable for: i. unphysical max. entangled states, MLE, <math>\mathcal{F}_t = 1</math>, <math>\theta \lesssim 3^\circ</math></p> <p>Seen before: no</p> <p>Explanation: none yet</p>

---

## 5. Conclusion

This thesis consists of two main parts, illuminating different aspects of information extraction in quantum systems. In the first part, a constructive method to design minimal non-linear witnesses for genuine multipartite entanglement was derived. Before, there were minimal witnesses for genuine multipartite entanglement only in rare special cases, without any constructive method to design them specifically for a certain state. Besides, constructive, fidelity based witnesses were known, but they still imposed a lot of experimental effort. Here, it was shown that it is possible to prove genuine multipartite entanglement with minimal effort, namely by measuring in only two settings (independent of the number of qubits), for prominent quantum states.

In a proof of principle experiment, we prepared four-qubit GHZ and cluster states in an optical setup using two entangled photons from a down-conversion source and encoded the qubits on polarisation and spatial degree of freedom using interferometers. This made the preparation of GHZ and cluster states as well as superpositions of them possible in a single setup, with high count rates leading to high state fidelity. We demonstrated full experimental control by performing full tomographies on all prepared states. Experimental data obtained in only two measurement settings could indeed be used to prove genuine multipartite entanglement for all states. Additionally, with data from former experiments, the applicability of our entanglement criteria could be verified for the four-qubit Dicke and singlet state as well.

Furthermore, this thesis examined the convergence of full quantum state tomography, in particular focusing on  $1/N$ -scaling and solutions to the problem that measurement results often lead to density matrices that do not represent a physical state. Simulations done on single qubit systems were used to analyse how the fidelity of reconstructed states scales with respect to the number of performed measurements. Both the direct approach to reconstruct the quantum state, linear inversion, and the more sophisticated maximum likelihood estimation were investigated, as these are two of the most commonly used methods to calculate an estimate of the density matrix from measurement data.

We found that a postselection criterion can be used to distinguish between different classes of reconstructed states, helping to interpret the tomography results. That criterion was also used to describe the effects of tomography on differently oriented states. Seemingly strange effects that were observed in earlier works could be explained intuitively with the help of the postselection criterion, which is trivial for the single qubit case. We extended these tools to both product and entangled two qubit systems, where the criteria are not unambiguous and trivial anymore, and showed their usefulness for the interpretation of tomography results.

Both the method to construct non-linear witnesses for detecting genuine multipartite entanglement and the postselection criteria for quantum tomography could prove to be useful tools for the extraction of information about quantum systems and play a role in the development of new protocols for quantum cryptography, quantum computation or quantum metrology.



## A. Interferometer setup

The process to set up an interferometer as used in Chapter 3 will be described here in more detail. Keep in mind that the interferometer is more stable the smaller it is built.

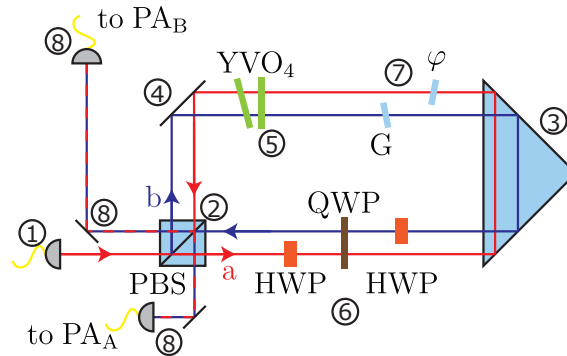


**Figure A.1.: Sagnac interferometer setup.** The numbers shown besides the components correspond to the order of placement.

To set up an interferometer in a Sagnac configuration as in Figure A.1, follow these steps:

- First, adjust the coupler of the incoming fiber (1) such that emitted light runs parallel to the optical table, e.g. with a pinhole.
- Then, place the polarising beam splitter (2). It has to be oriented very accurately, so assure that the reflected beam is still parallel to the optical table (using the pinhole), then use horizontally polarised light and minimise the intensity of the reflected part of the beam to adjust the angle. Pay heed to ghosting effects, i.e. beams reflected off non-functional surfaces of the PBS.
- The prism (3) is next to be set. Use the pinhole again to assure that the height of the beam stays the same, and position the prism such that there is enough space to reflect all beams. A small angle with respect to the beam is suggested, such that back-reflections are kept out of the main beam paths.
- Adjust the mirror in the interferometer (4) such that a rough mode overlap is achieved. It will be fine tuned later, when the other components have been inserted.
- The  $\text{YVO}_4$  crystals (5) are used to compensate polarisation dependent phases. First, use the vertically polarised light from the PBS, an additional polariser and a power meter to adjust the first crystal. For the second crystal, we need diagonally polarised light, so another polariser has to be inserted behind the PBS. Check that the polarisation stays the same when going through the  $\text{YVO}_4$ 's and the prism. See Figure A.2 (a) for the positioning of additional components.

- Insert the motorised waveplates (6). Take care that the half-wave plates will not touch the wrong beam, even if they are rotated by  $\pm 45^\circ$ . By using horizontally polarised light or just blocking mode  $b$  of the interferometer, the HWP in mode  $a$  and the QWP can be calibrated. Rotating them and measuring the intensity of light in output  $A$  with a photo diode can be used to find the zero position. Similarly, use vertically polarised light to calibrate the second HWP. Set all waveplates to their respective zero positions to continue. See Figure A.2 (b) for illustration.
- Again using diagonally polarised light entering the interferometer, set up the two glass plates (7) (one of them manually adjustable ( $G$ ), one motorised ( $\varphi$ )). Now, the contrast has to be optimised. For that purpose, first fine tune the mode overlap using the mirror (4), then try to find the point of destructive interference of zeroth order by setting the angle of glass plate  $G$ .
- Couple both interferometer outputs into single mode fibers (8) for spatial filtering. Use the mirrors to optimise coupling efficiency.

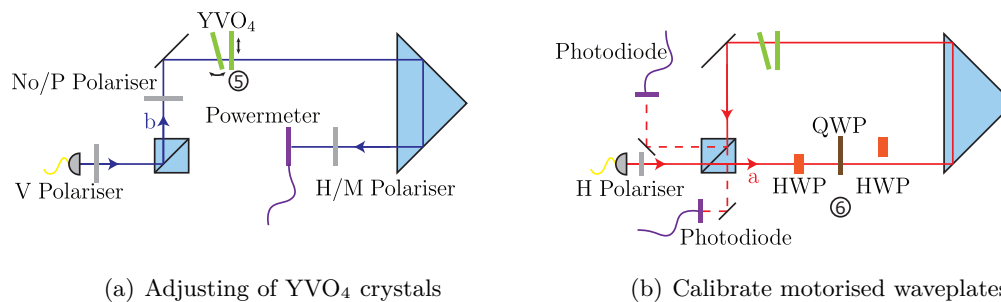


**Figure A.2.: Details on the interferometer setup process.** For the calibration of the  $\text{YVO}_4$  crystals (a), insert a vertical (V) polariser in front of the PBS, only the reflected mode  $b$  will be used. With the first crystal, make sure that the vertically polarised light is still vertically polarised after the prism, by inserting a horizontal (H) polariser and a power meter. For the second crystal, insert another polariser behind the PBS to produce diagonally polarised light and check again that the polarisation stays the same. For calibration of the first motorised HWP and the QWP (b), use only mode  $a$ . First insert the HWP, rotate it while taking a measurement curve with the photo diodes. The zero position is found by fitting. Then, do the same for the QWP. Use mode  $b$  to calibrate the second HWP.

## A.1. Compensation of phases

Polarisation dependent phases are already compensated by the  $\text{YVO}_4$  crystals, but there will be fluctuations in the path lengths, leading to a phase shift between the two interferometer modes  $a$  and  $b$ . These fluctuations can be time dependent, e.g. by thermal variations. Furthermore, there can be a dependence on the settings of the other elements in the interferometer. The waveplates may not be of exactly equal thickness everywhere, so there can be a change of phase when the waveplates are rotated. Therefore, before gathering data in a measurement series, the exact position of the phase compensating glass plate ( $\varphi$ ) is determined. For that purpose, single photons from a white LED and a diagonal (P) polariser are used instead of the down-conversion photons, in favour of higher count rates. The glass plate

is then rotated in 100 steps by a total of  $14^\circ$  and the interferometer response is measured. A typical measurement curve can be seen in Figure A.3.

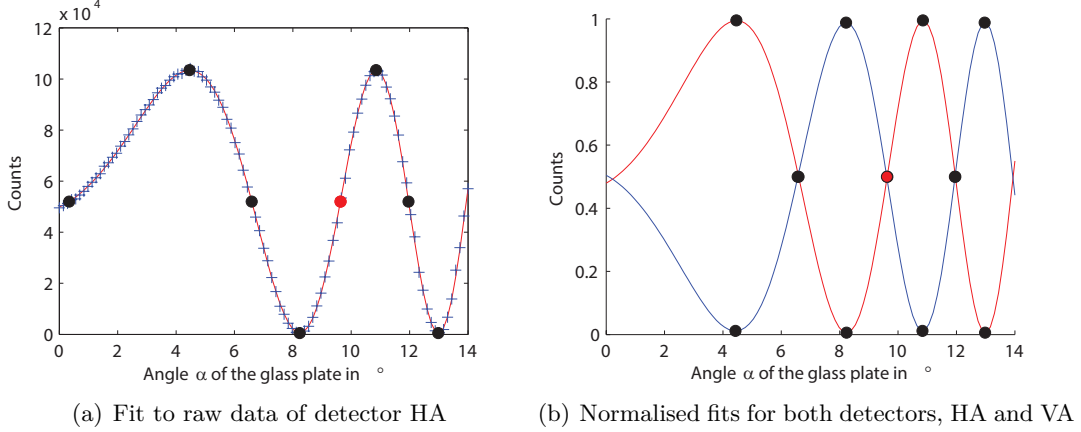


**Figure A.3.: Measurement of zero position of glass plate.** Here, the waveplates in the interferometer were set to measure in the  $x$  basis (see Table A.1). In that setting, right circular polarised light emerges from the interferometer in both outputs if the glass plate is at zero position. When the plate is rotated, the phase difference transforms the polarisation towards plus diagonally (P) polarised light, then to left circular (L), minus diagonal (M) and back to right circular (R). Since the waveplates in the analyses are set to separate  $|P\rangle$  and  $|M\rangle$  polarised photons, the point of half intensity in the increasing flank of the curve in the HA detector is the zero position of the glass plate. Data points are indicated by blue crosses +, the fits to outputs of detector HA and VA by red and blue lines, respectively. Black dots • mark the maximal, minimal, and half intensity points on the fits. The red dot • marks the zero position of the glass plate in this case.

A fit to the model

$$x_1 \left( \cos \left( 2\pi n x_2 \frac{1}{\sqrt{1 - \sin(\alpha + x_3)^2/n^2 - 1}} + x_4 \right) \right) + x_5$$

with the refractive index of the glass plate  $n = 1.52$ , the angle of the plate  $\alpha$  and the parameters of the fit  $x_i$ , is used to determine the respective zero position of the glass plate. Details on the model can be found in Ref. [61, 62]. Curves like these have to be recorded for all 3 settings of the waveplates in the interferometer that are to be used for measurement later. In the analyses, the HWP is set to  $22.5^\circ$ , while the QWP remains at  $0^\circ$ . The only problem occurs when trying to measure in the setting for the  $z$  basis since there would be no effect when turning the glass plate<sup>1</sup>. Therefore, two curves are measured, each with a slightly different angle setting, and the results are interpolated. The zero position of the glass plate corresponds to either a maximum, a minimum, or the point of half intensity in the flank of a curve, depending on the settings of the waveplates and the detector, see Table A.1.

## A.2. Efficiencies

Per interferometer, 4 detectors are used, having different detection efficiencies. Additionally, the coupling efficiencies of the single mode fibers behind the interferometer vary for every of

<sup>1</sup>because there is no interference; photons in mode  $a$  remain H-polarised and are transmitted to output  $A$ , photons in mode  $b$  are rotated from V- to H-polarisation and are transmitted into output  $B$

**Table A.1.: How to identify the zero position of the glass plate.** The zero position of the glass plate corresponds to the point of half intensity in the increasing flank (HI inc.), the decreasing flank (HI dec.), the position of the maximum (Max.) or the minimum (Min.), depending on the respective setting and the used detector.

Settings			Basis	zero position marked by			
HWP <sub>1</sub>	QWP	HWP <sub>2</sub>		HA	VA	HB	VB
22.5°	0°	22.5°	$x$	HI inc.	HI dec.	HI inc.	HI dec.
0°	45°	0°	$y$	Min.	Max.	Min.	Max.
0°	0°	40°	$z_1$	HI inc.	-	HI inc.	-
0°	0°	50°	$z_2$	HI dec.	-	HI dec.	-

the 3 different settings of the waveplates in the interferometer, leading to  $4 \cdot 3 = 12$  different efficiencies. This can be compensated after a measurement, if the *relative efficiencies* are known. They can be determined for each interferometer separately, as only coincidence events are recorded.

For that purpose, all components in the interferometer, including the glass plate, are set to the respective setting (see also Table A.1). The white LED with a diagonal polariser is used as a light source again. Then, for all settings, an equal amount of photons will be present in the two outputs of the interferometer. The waveplates in the analyses can now be rotated to guide the photons to either one of the respective detectors. For the  $y$  and  $z$  bases, the HWP has to be rotated since linear polarised light is emitted from the interferometer. The circular polarisation emitted in the  $x$  basis has to be rotated by the QWP. Fits to values near the maximum and the minimum determine the amplitudes of the measurement curves for all detectors in all settings. The relative efficiencies are given by the relative amplitudes.

# Bibliography

- [1] Planck, M. K. E. L., Zur Theorie des Gesetzes der Energieverteilung im Normalspektrum, *Verhandl. Dtsc. Phys. Ges.*, **2**, 237 (1900).
- [2] Heisenberg, W., Über den anschaulichen Inhalt der quantentheoretischen Kinematik und Mechanik, *Zeitschrift für Physik*, **43**, 3-4, 172 (1927).
- [3] Horodecki, R., Horodecki, P., Horodecki, M., and Horodecki, K., Quantum entanglement, *Rev. Mod. Phys.*, **81**, 865 (2009).
- [4] Einstein, A., Podolsky, B., and Rosen, N., Can Quantum-Mechanical Description of Physical Reality Be Considered Complete?, *Phys. Rev.*, **47**, 777 (1935).
- [5] Ekert, A. K., Quantum cryptography based on Bell's theorem, *Phys. Rev. Lett.*, **67**, 661 (1991).
- [6] Gisin, N., Ribordy, G., Tittel, W., and Zbinden, H., Quantum cryptography, *Reviews of modern physics*, **74**, 1, 145 (2002).
- [7] Nauerth, S., Moll, F., Rau, M., Fuchs, C., Horwath, J., Frick, S., and Weinfurter, H., Air-to-ground quantum communication, *Nature Photonics*, **7**, 5, 382 (2013).
- [8] Bennett, C. H., Brassard, G., Crépeau, C., Jozsa, R., Peres, A., and Wootters, W. K., Teleporting an unknown quantum state via dual classical and Einstein-Podolsky-Rosen channels, *Physical review letters*, **70**, 13, 1895 (1993).
- [9] Giovannetti, V., Lloyd, S., and Maccone, L., Advances in quantum metrology, *Nature Photonics*, **5**, 4, 222 (2011).
- [10] Shor, P. W., Polynomial-time algorithms for prime factorization and discrete logarithms on a quantum computer, *SIAM journal on computing*, **26**, 5, 1484 (1997).
- [11] Grover, L. K., Quantum mechanics helps in searching for a needle in a haystack, *Physical review letters*, **79**, 2, 325 (1997).
- [12] Ekert, A. and Jozsa, R., Quantum computation and Shor's factoring algorithm, *Reviews of Modern Physics*, **68**, 3, 733 (1996).
- [13] Dür, W., Vidal, G., and Cirac, J. I., Three qubits can be entangled in two inequivalent ways, *Phys. Rev. A*, **62**, 062314 (2000).
- [14] Klein, N., Fehleranalyse in der Rekonstruktion quantenmechanischer Zustände, Bachelor thesis, Ulm University (2012).
- [15] Knips, L., Reconstruction and analysis of multi-photon entangled quantum states, Master thesis, LMU Munich (2013).
- [16] Kiesel, N., Experiments on Multiphoton Entanglement, Doctoral thesis, LMU Munich (2007).

- [17] Schumacher, B., Quantum coding, *Phys. Rev. A*, **51**, 2738 (1995).
- [18] Yin, J., Cao, Y., Yong, H.-L., Ren, J.-G., Liang, H., Liao, S.-K., Zhou, F., Liu, C., Wu, Y.-P., Pan, G.-S., Li, L., Liu, N.-L., Zhang, Q., Peng, C.-Z., and Pan, J.-W., Lower Bound on the Speed of Nonlocal Correlations without Locality and Measurement Choice Loopholes, *Phys. Rev. Lett.*, **110**, 260407 (2013).
- [19] Bell, J., On the Einstein Podolsky Rosen Paradox, *Physics I*, **3**, 195 (1964).
- [20] Clauser, J. F., Horne, M. A., Shimony, A., and Holt, R. A., Proposed Experiment to Test Local Hidden-Variable Theories, *Phys. Rev. Lett.*, **23**, 880 (1969).
- [21] Aspect, A., Dalibard, J., and Roger, G., Experimental test of Bell's inequalities using time-varying analyzers, *Physical review letters*, **49**, 25, 1804 (1982).
- [22] Rowe, M. A., Kielpinski, D., Meyer, V., Sackett, C. A., Itano, W. M., Monroe, C., and Wineland, D. J., Experimental violation of a Bell's inequality with efficient detection, *Nature*, **409**, 6822, 791 (2001).
- [23] Bennett, C. H., Popescu, S., Rohrlich, D., Smolin, J. A., and Thapliyal, A. V., Exact and asymptotic measures of multipartite pure-state entanglement, *Phys. Rev. A*, **63**, 012307 (2000).
- [24] Eisert, J. and Plenio, M. B., A comparison of entanglement measures, *Journal of Modern Optics*, **46**, 1, 145 (1999).
- [25] Coffman, V., Kundu, J., and Wootters, W. K., Distributed entanglement, *Phys. Rev. A*, **61**, 052306 (2000).
- [26] Peres, A., Separability Criterion for Density Matrices, *Phys. Rev. Lett.*, **77**, 1413 (1996).
- [27] Gühne, O., Reimpell, M., and Werner, R. F., Estimating Entanglement Measures in Experiments, *Phys. Rev. Lett.*, **98**, 110502 (2007).
- [28] Eisert, J., Brandão, F. G. S. L., and Audenaert, K. M. R., Quantitative entanglement witnesses, *New Journal of Physics*, **9**, 3, 46 (2007).
- [29] Greenberger, D. M., Horne, M. A., and Zeilinger, A., Going beyond Bell's theorem, in Bell's theorem, quantum theory and conceptions of the universe, 69–72, (Springer1989).
- [30] Ardehali, M., Bell inequalities with a magnitude of violation that grows exponentially with the number of particles, *Phys. Rev. A*, **46**, 5375 (1992).
- [31] Hein, M., Eisert, J., and Briegel, H. J., Multiparty entanglement in graph states, *Phys. Rev. A*, **69**, 062311 (2004).
- [32] Walther, P., Resch, K. J., Rudolph, T., Schenck, E., Weinfurter, H., Vedral, V., Aspelmeyer, M., and Zeilinger, A., Experimental one-way quantum computing, *Nature*, **434**, 7030, 169 (2005).
- [33] Briegel, H. J. and Raussendorf, R., Persistent Entanglement in Arrays of Interacting Particles, *Phys. Rev. Lett.*, **86**, 910 (2001).
- [34] Dicke, R. H., Coherence in Spontaneous Radiation Processes, *Phys. Rev.*, **93**, 99 (1954).
- [35] Gühne, O., Bodoky, F., and Blaauboer, M., Multiparticle entanglement under the influence of decoherence, *Phys. Rev. A*, **78**, 060301 (2008).

- 
- [36] Trojek, P., Efficient Generation of Photonic Entanglement and Multiparty Quantum Communication , Doctoral thesis, LMU Munich (2007).
- [37] Kwiat, P. G., Waks, E., White, A. G., Appelbaum, I., and Eberhard, P. H., Ultrabright source of polarization-entangled photons, *Phys. Rev. A*, **60**, R773 (1999).
- [38] James, D. F. V., Kwiat, P. G., Munro, W. J., and White, A. G., Measurement of qubits, *Phys. Rev. A*, **64**, 052312 (2001).
- [39] de Burgh, M. D., Langford, N. K., Doherty, A. C., and Gilchrist, A., Choice of measurement sets in qubit tomography, *Phys. Rev. A*, **78**, 052122 (2008).
- [40] Uhlmann, A., The “transition probability” in the state space of a  $\star$ -algebra, *Reports on Mathematical Physics*, **9**, 2, 273 (1976).
- [41] Jozsa, R., Fidelity for Mixed Quantum States, *Journal of Modern Optics*, **41**, 2315 (1994).
- [42] Cramer, M., Plenio, M. B., Flammia, S. T., Somma, R., Gross, D., Bartlett, S. D., Landon-Cardinal, O., Poulin, D., and Liu, Y.-K., Efficient quantum state tomography, *Nature communications*, **1**, 149 (2010).
- [43] Donoho, D. L., Compressed sensing, *Information Theory, IEEE Transactions on*, **52**, 4, 1289 (2006).
- [44] Tóth, G., Wieczorek, W., Gross, D., Krischek, R., Schwemmer, C., and Weinfurter, H., Permutationally Invariant Quantum Tomography, *Phys. Rev. Lett.*, **105**, 250403 (2010).
- [45] Moroder, T., Hyllus, P., Toth, G., Schwemmer, C., Niggebaum, A., Gaile, S., Gühne, O., and Weinfurter, H., Permutationally invariant state reconstruction, *New Journal of Physics*, **14**, 10, 105001 (2012).
- [46] Schwemmer, C., Tóth, G., Niggebaum, A., Moroder, T., Gross, D., Gühne, O., and Weinfurter, H., Experimental comparison of efficient tomography schemes for a six-qubit state, *Physical review letters*, **113**, 4, 040503 (2014).
- [47] Gisin, N. and Bechmann-Pasquinucci, H., Bell inequality, Bell states and maximally entangled states for n qubits, *Physics Letters A*, **246**, 1–2, 1 (1998).
- [48] Badziąg, P., Brukner, i. c. v., Laskowski, W., Paterek, T., and Żukowski, M., Experimentally Friendly Geometrical Criteria for Entanglement, *Phys. Rev. Lett.*, **100**, 140403 (2008).
- [49] Bourennane, M., Eibl, M., Kurtsiefer, C., Gaertner, S., Weinfurter, H., Gühne, O., Hyllus, P., Bruß, D., Lewenstein, M., and Sanpera, A., Experimental Detection of Multipartite Entanglement using Witness Operators, *Phys. Rev. Lett.*, **92**, 087902 (2004).
- [50] Tóth, G. and Gühne, O., Detecting Genuine Multipartite Entanglement with Two Local Measurements, *Phys. Rev. Lett.*, **94**, 060501 (2005).
- [51] Knips, L., Schwemmer, C., Klein, N., Wieśniak, M., and Weinfurter, H., Multipartite entanglement detection with minimal effort, *arXiv*, 1412.5881 (2014).
- [52] Wieśniak, M. and Maruyama, K., Package of facts and theorems for efficiently generating entanglement criteria for many qubits, *Phys. Rev. A*, **85**, 062315 (2012).

- [53] Schwemmer, C., Knips, L., Tran, M. C., de Rosier, A., Laskowski, W., Paterek, T., and Weinfurter, H., Experimental multipartite entanglement without multipartite correlations, *arXiv*, 1412.5881 (2014).
- [54] Wieczorek, W., Schmid, C., Kiesel, N., Pohlner, R., Gühne, O., and Weinfurter, H., Experimental Observation of an Entire Family of Four-Photon Entangled States, *Phys. Rev. Lett.*, **101**, 010503 (2008).
- [55] Tóth, G. and Gühne, O., Detecting Genuine Multipartite Entanglement with Two Local Measurements, *Phys. Rev. Lett.*, **94**, 060501 (2005).
- [56] Mahler, D. H., Rozema, L. A., Darabi, A., Ferrie, C., Blume-Kohout, R., and Steinberg, A. M., Adaptive Quantum State Tomography Improves Accuracy Quadratically, *Phys. Rev. Lett.*, **111**, 183601 (2013).
- [57] Řeháček, J., Englert, B.-G., and Kaszlikowski, D., Minimal qubit tomography, *Phys. Rev. A*, **70**, 052321 (2004).
- [58] Gill, R. D. and Massar, S., State estimation for large ensembles, *Phys. Rev. A*, **61**, 042312 (2000).
- [59] Sugiyama, T., Turner, P. S., and Murao, M., Effect of non-negativity on estimation errors in one-qubit state tomography with finite data, *New Journal of Physics*, **14**, 8, 085005 (2012).
- [60] Knips, L., Schwemmer, C., Klein, N., Reuter, J., Tóth, G., and Weinfurter, H., Distribution of eigenvalues in quantum state tomography, *to be published* (2015).
- [61] Krebs, Isabel, Erzeugung und Analyse von Hyperentanglement mit einem Michelson-Interferometer, Bachelor thesis, LMU München (2010).
- [62] Reimann, Thomas, Erzeugung von Zwei-Qubit-Hyperentanglement mit einem Sagnac-Interferometer, Bachelor thesis, LMU München (2011).